Optical Transient Grating Measurements of Micro/Nanoscale Thermal Transport and Mechanical Properties

ARCHIVES
MASSACHUSETTS INSTITUTE OF TECHNOLOLGY
JUN 23 2015
LIBRARIES

by

Jeffrey Kristian Eliason

B.A. Chemistry, Concordia College (2010)

Submitted to the Department of Chemistry

in partial fulfillment of the requirements for the degree of

Doctor of Philosophy

at the

MASSACHUSETTS INSTITUTE OF TECHNOLOGY

June 2015

©Massachusetts Institute of Technology 2015. All rights reserved

Author........... Signature redacted ....
Department of Chemistry
April 30, 2015

Certified by ...... Signature redacted ....
Keith A. Nelson
Thesis Supervisor, Professor of Chemistry

Accepted by.......... Signature redacted ....
Robert W. Field
Chairman, Department Committee on Graduate Students

This doctoral thesis has been examined by a committee of the Department of Chemistry as follows:

Signature redacted

Professor Jianshu Cao ....

Chairperson

Signature redacted

Professor Keith A. Nelson ....

Thesis Supervisor

Signature redacted

Professor Gang Chen ....

Committee Member

Optical Transient Grating Measurements of Micro/Nanoscale Thermal Transport and Mechanical Properties

by

Jeffrey K. Eliason

Submitted to the Department of Chemistry on May 12th, 2015, in partial fulfillment of the requirements for the degree of Doctor of Philosophy

Abstract

The laser-based transient grating technique was used to study phonon mediated thermal transport in bulk and nanostructured semiconductors and surface wave propagation in a monolayer of micron sized spheres. In the transient grating technique two picosecond pulses are crossed to generate a spatially periodic intensity profile. The spatially periodic profile generates a material excitation with a well-defined wavevector. The time dependence of the spatially periodic material response is measured by monitoring the diffracted signal of an incident probe beam.

Non-diffusive thermal transport was observed in thin Si membranes as well as bulk GaAs at relatively short (micron) transient grating periods. First-principles calculations of the phonon mean free paths in Si and GaAs were compared with experimental results and showed good agreement. Preliminary measurements on promising thermoelectric materials such as PbTe and Bi_2Te_3 are presented showing evidence of non-diffusive transport at short length scales.

The transient grating technique was used to measure the thermal conductivity of Si membranes with thickness ranging from 15 nm to 1518 nm. Using the Fuchs-Sondheimer suppression function along with first-principles results, the thermal conductivity as a function of membrane thickness was calculated. The calculations showed excellent agreement with experimental measurements. A convex optimization algorithm was employed to reconstruct the phonon mean free path distribution from experimental measurements. This marks the first experimental determination of the mean free path distribution for a bulk material. Thermal conductivity measurements at low temperatures in a 200 nm Si membrane indicate the breakdown of the diffuse boundary scattering approximation.

The transient grating technique was used to generate surface acoustic waves and measure their dispersion in a monolayer of 0.5 – 1 μm diameter silica spheres. The measured dispersion curves show "avoided crossing" behavior due to the interaction between an axial contact resonance of the microspheres and the surface acoustic wave at a frequency of ~200MHz for the 1 μm spheres and ~700 MHz for the 0.5 μm spheres. The experimental measurements were fit with an analytical model in which the contact stiffness was the only fitting parameter. Preliminary results of surface acoustic wave propagation in microsphere waveguides, transmission through a microsphere strip, and evidence of a nonlinear response in a 2D array of microspheres are presented.

Thesis Supervisor: Keith A. Nelson
Title: Professor of Chemistry

Acknowledgements

As a graduate student at MIT I have had the great fortune of working with a host of wonderful people who have guided my development as a scientist and have been a joy to work with and get to know. First, I must thank my thesis advisor Keith Nelson. Without his support and guidance none of this work would have been possible. I am constantly impressed with his understanding of science and his ability to suggest new experiments that advance our current projects. His enthusiasm for science is infectious and the time I spend with him in meetings always leaves me refreshed and inspired to work harder. I have also appreciated his availability and willingness to meet with his graduate students despite his busy schedule. It has been a pleasure working with him!

There are many members of the Nelson group with whom I have worked very closely with over the years. Alex Maznev has been a part of the group for the duration of my tenure as a graduate student and has been so helpful in all aspects of my research. I have learned a great deal from him both on the experimental side of our work and understanding the theory. He has always been willing to discuss any questions I have, discuss and plan experiments, and come to the lab and solve problems. I am so grateful to him for being a great resource and mentor over the years. Jeremy Johnson was my predecessor on the transient grating project. Even though we only overlapped in the group for a short time, he taught me how to successfully operate the equipment in the lab and keep it running for the last 5 years. I am thankful for his patience in teaching and his willingness to continue to help me even though he was no longer on campus.

I want to thank the members of the acoustic subgroup, Kara Manke, David Veysset, Hyun Doug Shin for all the helpful discussions on photoacoustics. In particular, I want to thank Ryan Duncan and Alejandro Vega-Flick who are new members to the project and will continue the work I have been doing. They have been a great help in ongoing experiments and helping with data analysis while I was writing. I want to thank all the members of the Nelson group with whom I overlapped: Johanna Wolfson, Kit Werley, Harold Hwang, Brad Perkins, Xibin Zhou, Sharly Fleischer, Longfang Ye, Vasily Temnov, Felix Hofmann, Patrick Wen, Dylan Arias, Nate Brandt, Steph Teo, Brandt Pein, Ben Ofori-Okai, Colby Steiner, Samuel Teitelbaum, Yongbao Sun, Jian Lu, Ilana Porter, Joseph Yoon, Leora

Cooper, Prasahnt Sivarajah, Yaqing Zhang, Xian Li, and Yu-Hsiang Cheng. The members of the Nelson group have created a great atmosphere to learn about science and have fun at the same time. I am so grateful for all the discussions I had with the Nelson group members.

I would like to thank Jill Sewell for working with me in the outreach Lambda Lab. Jill helped by organizing and teaching high school students about our experimental technique. I am thankful for the opportunity I had to work in the outreach lab and I had a great time working with Jill and the students.

My graduate work would not have been possible without help from a number of collaborators outside of the Nelson group. The majority of the funding for this thesis was provided by the Solid State Solar Thermal Energy Conversion (S^3TEC) center under the award number DE-SC0001299 / DE-FG02-09ER46577. S^3TEC was part of the larger DOE Energy Frontier Research Center (EFRC) program. Gang Chen was the leader of S^3TEC and I have been able to work closely with him and his group members, John Cuffe, Kim Collins, Maria Luckyanova, Lingping Zeng, Vazrik Chiloyan and Sam Huberman.

The work on silicon membranes was done in collaboration with the Institute Catala de Nanociencia i Nanotecnologia (ICN) and the Technical Research Center of Finland (VTT). From ICN we got silicon membrane samples and I worked with Clivia Sotomayor Torres, Timothy Kehoe, Emigdio Chávez-Ángel, and Sebas Reparaz. From VTT we got ultra-thin silicon samples from Andrey Shchepetov, Mika Prunnila and Jouni Ahopelto.

The work on microspheres was performed in collaboration with Prof. Nick Fang and his students Anshuman Kumar and Tian Gan from MIT. They helped in fabricating samples and theoretical analysis of the data. I also worked closely with Prof. Nick Boechler and his students Amey Khanolkar and Morgan Hiraiwa at the University of Washington. Nick Boechler was a post-doc at MIT in Nick Fang's group and helped with the first microsphere experiments, data analysis, and sample fabrication. Now at the University of Washington, Nick B. and his group have continued to help with sample fabrication, experiments, and theoretical analysis.

I would like to thank the many people outside of science who have made my time at MIT enjoyable. I want to thank all the members of my intramural sports teams and the chemistry basketball teams, the guys from noonball where I was able to play many hours of basketball to relax, and Kari Thande who convinced me to play in community basketball leagues for a number of seasons. In particular I would like to thank Russ Jensen for all that time on the court and on the field.

I also need to thank my parents Roger and Bonita Eliason for their constant support over the years and my brother Karl Eliason for all the hours chatting and playing games. I would also like to thank my future in-laws Alan and Lori Petersen and Ross Petersen who have been very supportive. Finally I would like to thank my fiancé Beci Petersen for all the hours we spent talking every night. Her constant support and encouragement have helped me stay focused and have inspired me to work hard in graduate school. I am thankful for all she has done and I look forward to finally getting to be with her.

Optical Transient Grating Measurements of Micro/Nanoscale Thermal Transport and Mechanical Properties:

Table of Contents

Abstract 5

Acknowledgements 7

1. Overview 13

2. Transient Grating Technique 17

- 2.1. Crossing Beams 17
- 2.2. Material Excitation 18
- 2.3. Heterodyne detection and phasemask 21
- 2.4. Phase and amplitude grating 23
  - 2.4.1. Transmission geometry 23
  - 2.4.2. Reflection geometry 26
- 2.5. Experimental setup 27
- 2.6. Continuously variable grating period 28
- 2.7. Summary 30

3. Thermal Transport in Non-Metallic Crystals 33

- 3.1. Introduction 33
- 3.2. Thermal conductivity 33
  - 3.2.1. Introduction to thermal conductivity 33
  - 3.2.2. Phonon dispersion 35
  - 3.2.3. Heat capacity 37
  - 3.2.4. Phonon mean free path 37
- 3.3. Experimental observations of non-diffusive thermal transport 40
  - 3.3.1. Measurement of thermal transport with TG technique 41
  - 3.3.2. Non-diffusive transport in a 400 nm Si membrane 42
  - 3.3.3. Modeling non-diffusive transport in the TG geometry 45
- 3.4. Thermal conductivity measurements in bulk materials 47
  - 3.4.1. TG measurements in reflection 48
  - 3.4.2. Phase and amplitude grating in reflection 49
  - 3.4.3. Non-diffusive thermal transport in bulk GaAs 51
  - 3.4.4. Results for promising TE materials (PbTe and Bi_2Te_3) 53
- 3.5. Summary 56

4. **Recovering Phonon MFP contributions to Thermal transport** **59**
  4.1. Introduction 59
  4.2. In-plane thermal conductivity of Si membranes 61
  4.3. Phonon boundary scattering 64
  4.4. Comparing experiment to theory 66
  4.5. Reconstruction the MFP distribution 67
  4.6. Low temperature measurements in a 200 nm Si membrane 69
  4.7. Summary 71
5. **Surface Acoustic Waves in Granular media** **75**
  5.1. Introduction 75
  5.2. Contact mechanics and adhesion 75
  5.3. SAW generation and detection 78
  5.4. Wave behavior in a monolayer of microspheres 79
    5.4.1. Experiment 79
    5.4.2. Theory 82
  5.5. Summary 86
6. **Mechanical Properties of Microsphere Structures** **89**
  6.1. Introduction 89
  6.2. Variability of adhesion conditions 89
    6.2.1. Sample-to-sample variations 89
    6.2.2. Changing humidity 92
  6.3. 500 nm spheres 94
  6.4. Microsphere waveguides 96
  6.5. SAW filtering 100
  6.6. Nonlinear dynamics 105
  6.7. Summary 107
  References **109**

Chapter 1

Overview

The study of light-matter interactions, or spectroscopy, dates back to the first experiments performed by Newton. Over the years, spectroscopy has been used as a powerful tool for experimentalists to explore the natural world. Its discoveries have shaped theories that form the basis for modern physical science. Modern spectroscopists have access to coherent laser sources with short pulses enabling the study of a host of interesting phenomena on short time scales. Typical optical experiments use single laser spots with a pump pulse that generates the material excitation and a probe pulse that measures the response. This technique, called pump-probe spectroscopy is ubiquitous in modern spectroscopy. A natural extension is to generate spatially dependent material responses by using constructive and destructive interference to shape the spatial profile of the light's electric field. This is the basis for the fields of holography and four-wave-mixing [Collier, Eichler].

This thesis presents measurements conducted using a four-wave-mixing technique commonly known as transient grating, or impulsive stimulated scattering (ISS). In the transient grating technique, two short optical pulses overlap spatially and temporally to generate a sinusoidal interference pattern. The spatially periodic profile generates a periodic excitation in a material. Diffraction of an incident probe beam monitors the time dependence of the material response. Depending on the material an electronic, thermal, and/or strain profile is generated with a well-defined wavevector. The sinusoidal profile of the material response allows for relatively straightforward analysis of the generated signal.

In this thesis I present a selection of the work I have done at MIT using the transient grating technique to study thermal and mechanical properties of materials. In recognition of all the collaborators who have aided in this work I will use 'we' for the remainder of the thesis.

Chapter 2 introduces the transient grating technique. The description of the technique includes the generation and detection of a periodic thermal profile and surface acoustic waves. Then, the experimental setup is described and a novel modification to the technique is presented. The remainder of the thesis covers two major projects. Chapters 3 and 4 cover studies of the fundamental nature of thermal transport in semiconductors. Chapters 5 and 6 describe interesting mechanical behavior in granular materials.

Chapter 3 begins with an introduction to thermal transport in non-metallic crystals, including the important parameters in determining the thermal conductivity of materials. We describe the analysis of 1D and 2D thermal profiles from crossed beams in a semi-transparent material or at the surface of an opaque material. Then, we present observations of deviations from diffusive thermal transport in bulk and nanostructured semiconductors showing the broad distribution of the mean free paths of heat carriers. In an attempt to observe non-diffusive effects in promising thermoelectric materials we present thermal conductivity measurements in PbTe and Bi_2Te_3. In chapter 4 we present the experimental determination of the mean free path distribution in Si using experimental measurements of thermal conductivity. We describe phonon boundary scattering in thin films and present the Fuchs-Sondheimer suppression function, which describes the reduction of thermal conductivity in a thin film. Low temperature measurements in a Si membrane are presented to study the temperature dependences of thermal conductivity and phonon boundary scattering. We compare all our results to first-principles calculations and in most cases, demonstrate good agreement between experiment and theory.

In chapters 5 and 6 we discuss surface acoustic wave behavior in a granular media. In particular, we study a monolayer of micron-sized spheres. Chapter 5 introduces contact mechanics and adhesion in the context of a sphere in contact with an elastic substrate. Then we discuss transient grating measurements of the surface acoustic wave dispersion, which demonstrates an interaction between the axial contact of the spheres and the surface wave. We compare our measured dispersion to an analytical result based on contact models. Chapter 6 details experiments aimed at learning more about the adhesive interaction between sphere and substrate. We present dispersion measurements as a function of humidity, substrate surface conditions, and sphere diameter. We conclude with a demonstration of surface acoustic wave filtering and evidence of nonlinearity in the microsphere contact.

Chapter 2

Transient Grating Technique

The transient grating technique, also called impulsive stimulated scattering (ISS), uses a four-wave mixing process to generate and detect coherent material excitations. ISS takes advantage of the periodic intensity profile generated from crossing two spatially and temporally coincident laser pulses to set the wavevector of the excitation. This technique, hereafter referred to as transient grating (TG), is well developed in the literature and has been use for studying a wide variety of systems [Eichler]. Here we will cover relevant information related to generation and detection of mechanical and thermal responses. A schematic illustration of a typical TG setup is shown in Fig 2.1. The description of the TG experiment will begin with the crossed laser beams for excitation, followed by the probing of the material response, and conclude with a novel advancement to the technique.

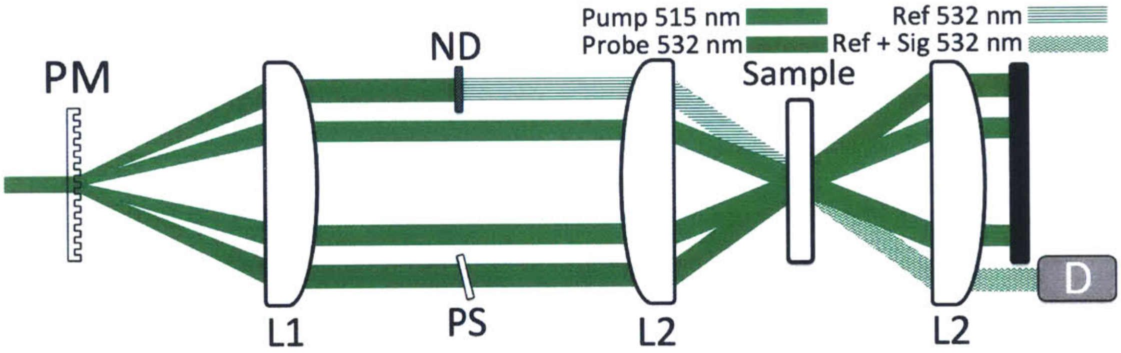

Fig 2.1. Schematic illustration of the TG setup used for many experiments described in this thesis. PM is a binary optical diffraction grating called a phase mask. ND is the neutral density filter used to attenuate one arm of the probe beam creating the reference beam. PS is a highly parallel glass plate used to control the relative phase between the probe and the reference fields. L1 and L2 are achromatic doublet lenses where L1 has twice the focal length of L2 for 2:1 imaging. D is a fast (>1GHz bandwidth) photodetector and is connected with an oscilloscope for real-time data collection.

2.1 Crossing Beams

When two plane waves with identical wavelength and polarization cross, the resulting constructive and destructive interference creates a sinusoidal intensity profile. Crossing two beams on a surface and observing the profile with a CCD camera provides an image of the periodic interference pattern as seen in Fig 2.2

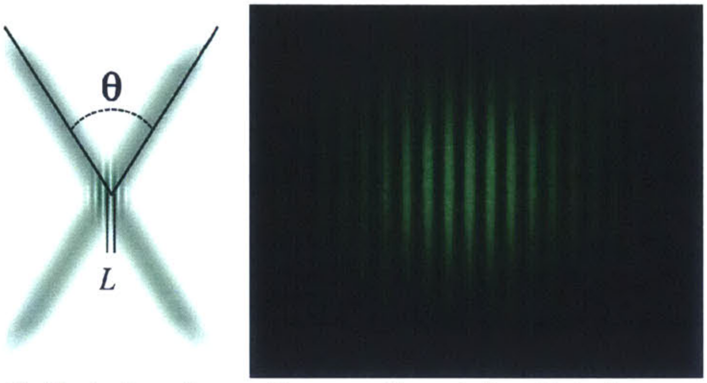

Fig 2.2 (Left) Schematic illustration of crossed beams with angle θ and interference pattern period *L*. (Right) CD Image of crossed beams on a 100 nm aluminum layer on a glass substrate. The resulting period is 13.5 μm.

The period *L* of the interference pattern is given by the following equation,

$$L = \frac{2\,\pi}{q} = \frac{\lambda}{2\,\sin\left(\frac{\theta}{2}\right)} \tag{2.1}$$

Here *q* is the magnitude of the grating wavevector, λ is the wavelength of the light, and θ is the angle at which the beams are crossed. If the medium is transparent and both beams enter through the same surface, the period of the interference pattern is unchanged compared to the period for beams crossed in air. The period remains unchanged because the change in angle due to refraction from entering medium with a higher refractive index counteracts the change in wavelength of the light. It is worth noting that if two beams are crossed with perpendicular polarizations, e.g. vertical and horizontal, the generated interference pattern has a periodic polarization profile rather than a periodic intensity profile.

2.2 Material Excitation

Typically we use short laser pulses to generate a material excitation, which we call the pump process. If the sample of interest absorbs the laser light, sudden heating and subsequent thermal expansion cause a fast, step-like stress response, which launches counter-propagating acoustic waves. The period of the resulting thermal profile and the wavelength of the acoustic wave match the period of the interference intensity profile given by *L*, shown in Eq (2.1). The temperature rise in the material, δT, is determined by the absorbed energy, which is proportional to the intensity of the light as,

$$\delta T(x) \propto I(x) = I_{abs}\cos^2\left(\frac{q}{2}x\right) = {}^1/_2\, I_{abs}(1+\cos(qx)). \qquad (2.2)$$

Here *I(x)* is the spatially periodic intensity profile, I_{abs} is the absorbed intensity and q is the grating wavevector. The stress from thermal expansion, σ, can be calculated as[Nye, Landau, JohnsonPhD]:

$$\sigma_{ij}(x) = c_{ijkl}\alpha_{kl}\delta T(x) \propto c_{ijkl}\alpha_{kl}\cos(qx) \qquad (2.3)$$

The subscripts refer to summations over the index according to Einstein notation. Here c_{ijkl} is the elastic stiffness tensor and α_{kl} is the thermal expansion tensor. In the case of an isotropic material c_{ijkl} is the bulk modulus and α_{kl} becomes the linear thermal expansion coefficient. If the material is thick and partially absorbing, heat is deposited throughout the depth of the material and thermal expansion generates a bulk longitudinal wave. A standing wave occurs in the region where the two counter-propagating waves overlap, but the waves will continue to propagate until material damping dissipates the energy. At the same time, the sinusoidal temperature profile decays due to thermal diffusion that moves energy from peaks to nulls of the pattern. The thermal and acoustic responses are probed by diffraction of an incident laser beam due to coupling between the refractive index and the material response. The probing process will be covered in more detail in the next section. The diffraction of the probe beam by thermal and acoustic responses caused by an impulsive temperature rise in an absorbing material is often termed impulsive stimulated thermal scattering (ISTS) [Rogers94, Yang].

In the case where the material is strongly absorbing the pump beams are absorbed close to the surface and thermal expansion generates surface acoustic waves (SAWs)[Rogers00]. The thermal profile is also created near the surface of the material and now heat flows into the depth of the material in addition to heat transport from peak to null [Käding]. Surface heating and SAWs will be discussed more thoroughly later in the thesis.

In the case where the sample does not absorb the pump light, non-resonant excitation can occur through a process called electrostriction. In electrostriction, the electric field of the light perturbs the electron density of the molecules in the sample. The fast change in electron density causes the nuclei to respond and results in an applied stress. Much like ISTS, if the intensity profile occurs in a bulk medium, the electrostrictive driving force generates counter-propagating bulk longitudinal waves, but in this case there is no heating. Since the stress only lasts as long as the short pump pulse (sub-nanosecond). The diffraction of the probe beam by acoustic responses generated via electrostriction is called impulsive stimulated Brillouin scattering (ISBS)[Yan, JohnsonPhD, TorchinskyPhD]. In general, semi-transparent samples yield acoustic responses due to a combination of ISTS and ISBS driving forces. It should be noted that in ISTS the driving force is step-like (following the temperature rise) while in ISBS it is delta-like (following the laser intensity profile), which results in a phase difference between the ISTS and ISBS signals [JohnsonPhD]. Representative signals from samples demonstrating ISTS and ISBS are shown in fig 2.3.

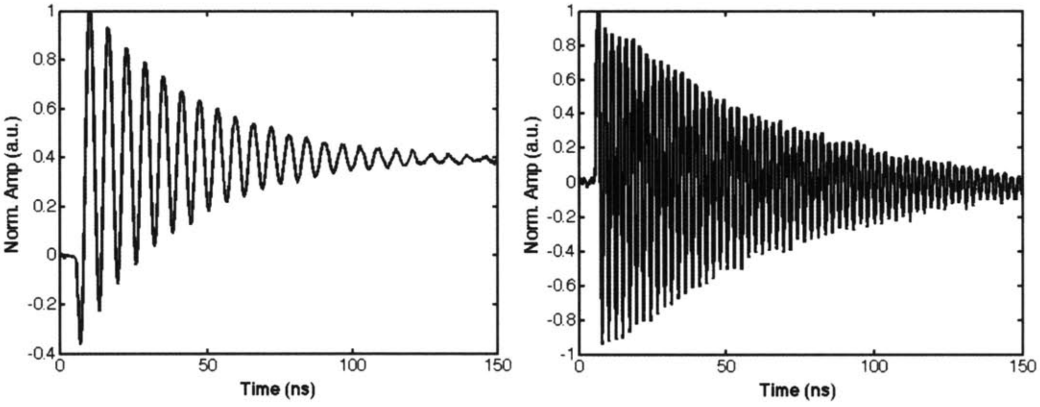

Fig 2.3 (Left) TG data from PDMS showing a combination of ISTS and ISBS responses. The oscillations from counter-propagating acoustic waves are offset from zero indicating a long-lived thermal grating. (Right) TG data from PMMA demonstrating a pure ISBS signal.

The ISBS driving force is also capable of generating bulk shear waves. Rather than using the same polarization for both pump beams, crossed polarizations generate a periodic polarization profile. Since this has no intensity profile there will be no periodic absorption and no ISTS signal allowing for isolation of shear waves

[JohnsonPhD]. Since the samples we have investigated in this thesis show no ISBS component, in the following "transient grating" will exclusively mean ISTS.

2.3 Heterodyne detection and phasemask

In order to measure the material response generated by the pump beams, we direct another laser beam, the probe, onto the crossing region. The probe diffracts off of the periodic refractive index modulation due to the coupling between the optical properties and material excitation, such as temperature and strain [Berne]. The diffracted signal is overlapped with another beam, the local oscillator or reference beam, in a process called heterodyning. The diffracted signal can be generated with a variably delayed pulse or with a continuous wave (cw) laser. For all of the experiments presented here a cw laser is used and the diffracted signal is sent to a fast photodetector connected to an oscilloscope. This real-time detection scheme is preferable for responses on the nanosecond to microsecond time scales, as it reduces data collection time. In real-time detection, the fastest measurable time dynamics are limited by the bandwidth of the detection electronics (photodiode and oscilloscope). If we wanted to resolve dynamics on the picosecond to femotosecond time scales, we would need femtosecond pulses and a scanning delay line.

The time dependence of the material response, in this case the temperature profile and acoustic waves, is carried in the intensity of the diffracted signal. The diffracted signal and reference beam are overlapped and interfere to give the following intensity [Maznev98],

$$I_{s+r} = I_s + I_r + 2\sqrt{I_s I_R} \cos \varphi \tag{2.4}$$

Here I_s is the intensity of the diffracted signal, I_r is the intensity of the reference and φ is the phase difference between the two beams. In the case where $I_r >> I_s$, the measured signal, I_{s+r} is linearly dependent on $\sqrt{I_r}$, because I_s is negligible and I_r has no time dependence. Since the pump-induced perturbations of the sample are proportional to the diffracted electric field, the heterodyne signal is linearly proportional to the material response. In addition, the linear dependence of the signal on $\sqrt{I_r}$ is beneficial for reducing noise from the detection electronics and scattered light [Maznev98]. Data can be collected at $\varphi = 0$ and $\varphi = \pi$, and by subtracting the two traces, any signals not dependent on the heterodyne phase, such as signals from low-frequency EM sources or scattered pump light, are eliminated. Finally, it allows for information dependent on the phase to be recovered, which will be covered in more depth in the following section. Representative traces taken at $\varphi = 0$ and $\varphi = \pi$ are shown in figure 2.4.

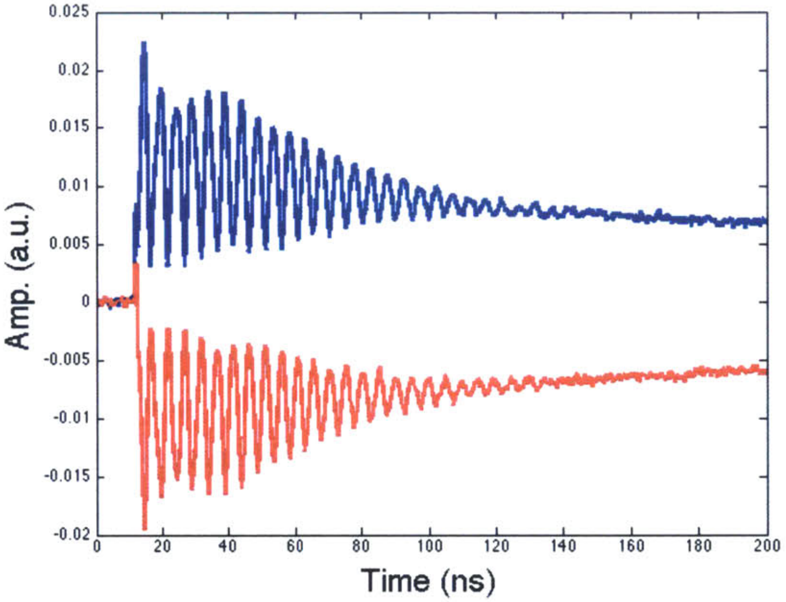

Figure 2.4: Time traces taken at $\varphi = 0$ (blue) and $\varphi = \pi$ (red) for surface excitation of a 200 nm aluminum film on a glass substrate.

With common reflective optics, achieving heterodyne detection is complicated because it is difficult to overlap two beams and maintain a stable phase between them [Nelson82]. In practice, using an optical phase mask solves this issue [Maznev98]. An optical phase mask is a binary diffraction grating, basically a piece of glass with a periodic square relief pattern. The square-wave pattern diffracts an incident beam into all the Fourier components of the square wave. The height of the square pattern is set to optimize the ±1 diffraction orders for a certain wavelength of light. The TG condition of two crossed beams is achieved by using a two-lens imaging system, where the first lens brings the beams parallel and the second lens crosses them at the sample. The setup including phase mask, and two lenses can be seen in figure 2.1. Use of the phase mask makes alignment of the TG experiment simple. If the pump and probe beams are incident on the same location on the phase mask, all four beams, i.e., the ±1 diffraction orders from pump and probe, will be recombined at the same location on the sample. This also ensures that the diffracted signal will be overlapped with the reference beam, created by attenuating one arm of the probe. We can also describe this setup as imaging of the phase mask but with a Fourier filter (blocking all higher order beams), which results in a sinusoidal intensity profile with half the period of the phase mask. Now that we have established the framework of the TG setup it is instructive to look at the origin of the diffracted signal from a periodic material excitation.

2.4 Phase and amplitude grating

2.4.1 Transmission geometry

In general, we can determine the transmission of a probe beam through a thin sample with no reflection at the interfaces by multiplying the input electric field by a complex transmission function given by [Collier, JohnsonPhD],

$$t_0 = \exp\left(i\left(t_0'(\tau) + it_0''(\tau)\right)\right) \tag{2.5}$$

where, t_0' is the real part of the transmission function, t_0'' is the imaginary part of the transmission function, and τ is time. Excitation of the material results in a spatial and temporal modulation of the complex transfer function with the following result,

$$t(x,\tau) = t_0 \exp\left(i\left(t'(\tau) + it''(\tau)\right)\cos(qx)\right) \tag{2.6}$$

where q is the TG wavevector, $t'(t)$ is the change in the real part of the transmission function, and $t''(t)$ is the change in the imaginary part of the transmission function. We assume that the excitation results in a small perturbation to the optical properties of the sample giving,

$$t(x,\tau) = t_0(1 + \cos(qx)[it'(\tau) - t''(\tau)]) \tag{2.7}$$

We can see from the transmission function that t' will result in a change in the phase of the incident electric field and t'' will change the amplitude and so we call these the phase and amplitude grating respectively. We approximate the electric field of the probe and reference as plane waves giving,

$$E_p = E_{0p}\exp\left(i\left(k_p^2 - \frac{q^2}{4}\right)^{1/2} z - i\frac{q}{2}x - i\omega_p\tau + i\varphi_p\right) \tag{2.8}$$

and,

$$E_r = a_r E_{0p}\exp\left(i\left(k_p^2 - \frac{q^2}{4}\right)^{1/2} z + i\frac{q}{2}x - i\omega_p\tau + i\varphi_r\right) \tag{2.9}$$

Here E_{0p} is the amplitude of the incident probe beam, k_p is optical wavevector magnitude of the probe, q is the wavevector of the transient grating, ω_p is the frequency of the optical light, φ_p and φ_r are the phases of probe and reference respectively, and a_r is the attenuation coefficient of the reference beam.

To obtain the diffracted fields we multiply the probe field, E_p, and the transmission function [Collier, JohnsonPhD]. First order diffraction of the probe beam gives the following result,

$$E_{p(+1)} = E_s = E_{0p}t_0[it'(\tau) - t''(\tau)]\exp\left(i\left(k_p^2 - \frac{q^2}{4}\right)^{1/2} z + i\frac{q}{2}x - i\omega_p\tau + i\varphi_p\right) \tag{2.10}$$

Heterodyne detection requires that the first order diffraction from the probe overlaps with one order of the reference beam. We see that this condition is met by the zero order diffraction, or the transmission, of the reference given by,

$$E_{r(0)} = a_r E_{0p} t_0 \exp\left(i\left(k_p^2 - \frac{q^2}{4}\right)^{1/2} z + i\frac{q}{2}x - i\omega_p\tau + i\varphi_r\right) \tag{2.11}$$

The probe and reference fields are collinear, and the resulting interfere intensity is,

$$I_{s+r(0)} = I_{0p}{t_0}^2(a_r^2 + t'^2(\tau) + t''^2(\tau) - 2a_r[t''(\tau)\cos\varphi - t'(\tau)\sin\varphi]) \tag{2.12}$$

where $\varphi = \varphi_p - \varphi_r$, is the heterodyne phase. If the reference beam were absent the diffracted signal would be,

$$I_{s(non-het)} = I_{0p}{t_0}^2\left(t'^2(\tau) + t''^2(\tau)\right) \tag{2.13}$$

Therefore, without heterodyning the signal is comprised of a mix of phase and amplitude grating contributions, making it difficult to analyze this signal. With heterodyning, if the reference intensity is much larger than that of the diffracted probe, the heterodyne signal dominates,

$$I_{s(het)} = 2I_{0p}{t_0}^2 a_r[t''(\tau)\cos\varphi - t'(\tau)\sin\varphi] \tag{2.14}$$

Here we can see that the heterodyne signal has a linear dependence on the probe intensity, I_{0p}, and on the attenuation factor of the reference, a_r. We can also see that the by selecting the appropriate heterodyne phase we can isolate the phase or amplitude grating contribution to the signal. By setting $\varphi = 0$ or π, the heterodyne signal will come from the phase grating and at $\varphi = \pi/2$ and $3\pi/2$ the heterodyne signal will come from the amplitude grating. The ability to select between the phase and amplitude grating components is essential for unambiguous determination of TG signals. In addition subtracting signals with π phase difference eliminates any non-heterodyne terms.

To build physical intuition for the pump-probe response it is instructive to look at how the material response couples to the complex refractive index, $n^* = n + ik$. For a weak, thin grating, the real and imaginary parts of the transmission function map directly to changes in the real and imaginary parts of the complex refractive index. In this specific scenario the heterodyne signal is as follows,

$$I_{s(het)} = 2I_{0p}{t_0}^2 a_r k_p z[\delta k(\tau)\cos\varphi - \delta n(\tau)\sin\varphi], \tag{2.15}$$

where δn is the change in the real part of the complex refractive index, δk is the change in the imaginary part of the complex refractive index and z is the thickness of the sample. Temperature and strain cause changes in the real and imaginary parts of the complex index of refraction [Eichler],

$$\begin{aligned} \delta n &= \frac{\partial n}{\partial \varepsilon} d\varepsilon + \frac{\partial n}{\partial T} dT \\ \delta k &= \frac{\partial k}{\partial \varepsilon} d\varepsilon + \frac{\partial k}{\partial T} dT \end{aligned} \tag{2.16}$$

Here ε is the strain response coming from the applied stress, and T is the temperature rise from heating after absorption in the medium. Heterodyne detection can separate the contributions from the phase and amplitude grating, changes in δn and δk respectively. In general the real and imaginary components of the transmission are related to the changes in the complex refractive index but it is not as simple as the above case. For example, when there are multiple reflections in the sample, i.e. Fabry-Pérot effects, it is not trivial to determine how transmission is affected by changes in refractive index [Brekhovskikh].

2.4.2 Reflection geometry

For strongly absorbing materials the laser light is absorbed near the surface, and in addition to changes in the complex reflectivity, there is a net surface displacement from thermal expansion. It is straightforward to account for this by incorporating an addition phase term in the transmission function above, to obtain the complex reflection function,

$$r(x,\tau) = r_0 \exp\left(i\left(r'(\tau) + ir''(\tau)\right)\cos(qx)\right) \exp\left(-i2k_p u(\tau)\cos(qx)\cos(\beta_p)\right) \qquad (2.17)$$

where r_0 is the baseline reflectivity of the sample, r' is the change in the amplitude of the reflectivity, r'' is the change in the phase of the reflectivity, $u(\tau)$ is the amplitude of surface displacement, and β_p is the angle of incidence of the probe beam. Following the same procedure as above the heterodyne signal is given by,

$$I_{s(het)} = 2I_{0p}{r_0}^2 a_r\left[r'(\tau)\cos\varphi - \left(r''(\tau) - 2k_p u(\tau)\cos(\beta_p)\right)\sin\varphi\right] \qquad (2.18)$$

By adjusting the heterodyne phase, we can again isolate the amplitude grating or the phase grating contribution to the signal. The amplitude grating is given by the real part of the reflectivity, $r'(\tau)$, but now the phase grating, $r''(\tau)-k_p u(\tau)\cos(\beta_p)$, has a combination of the change in reflectivity and diffraction from the surface displacement. The kinetics of the reflectivity change and surface displacement are not the same [Käding, Johnson12], which makes analysis of the phase grating complicated. For thermal measurements of highly absorbing samples the amplitude grating provides a straightforward way to measure the kinetics of the thermal grating decay[Johnson12].

2.5 Experimental setup

All the experiments in this thesis use a short excitation pulse from a HighQ femtoREGEN system. The HighQ femtoREGEN is a Yb:KGW laser system with self contained oscillator and regenerative amplifier. The system has a variable repetition rate, but we run it at 1kHz, which is down counted from the oscillator rep-rate of 78 MHz. Under normal operation, the laser outputs 300 fs pulses at 1035 nm. To avoid sample damage from high peak powers we bypass the compressor to obtain ~200 ps pulses. A detailed guide for operation and troubleshooting can be found in Appendix A of [TorchinskyPhD]. To accommodate the samples studied, we use a shorter wavelength obtained by frequency doubling the fundamental output to ~515 nm using a temperature controlled BBO (beta-barium borate) crystal. The BBO crystal was made for 1064 nm, but by heating the crystal to 240 °C we achieve a reasonable second harmonic generation efficiency at 1035 nm. The probe laser is a 532 nm Coherent Verdi V5 single-longitudinal mode laser. The Verdi was chosen for its highly stable output, long coherence length (~60 m), and because the wavelength is well matched to the 515 nm pump light. Matching the pump and probe wavelengths improves the imaging of the phase mask by reducing chromatic aberrations. We modulated the probe output with an electro-optic modulator (EOM - ConOptics 350-50 with 302 RM high voltage source) in conjunction with a delay generator to obtain a 64 μs probe window (~95-5 duty cycle). We used a short probe duration with the goal of reducing the heating of the sample, although in most cases we observed a much larger impact from the peak power of the probe than from the duty cycle of the probe [Note1]. As mentioned above, we used a custom phase mask optimized for 532 nm light (80% of the power in ±1 diffraction orders). We created a 2:1 imaging system using Thorlabs achromatic doublets, where the first lens had a focal length of f = 15 cm and the second lens had f = 7.5 cm. For most experiments the pump and probe beams were overlapped on the phase mask, with the pump beam at normal incidence and the probe beam at a slight angle below normal allowing for separation of pump and probe beams in the vertical plane.

After the sample, we directed the collinear reference and signal beams to a 1 GHz bandwidth Si avalanche photodiode from Hamamatsu (C5658). A laser line filter set to block the excitation wavelength of 515 nm was used to reduce scattered pump light. The APD module was connected with an SMA cable to a 4 GHz bandwidth Tektronix TDS 7404 oscilloscope. Thorlabs ND 3 filters were used to attenuate the reference beam. It was found that ND 3 was the appropriate level of attenuation to avoid saturating the Hamamatsu detector, although for a different detector a different ND filter would likely be optimal. For phase control of the probe and reference beams, we used a highly parallel CVI SQW1-1512-UV fused silica plate. The angle of the window was adjusted by a Thorlabs Z612 motorized actuator with TDC001 Servo controller. In general, to avoid issues from probe lasers with short correlation length, the thickness of the glass slide and ND filter should be well matched. For temperature dependent measurements we used a Janis ST-100H cryostat connected to a Lakeshore 331 temperature controller. Data acquisition was performed with Labview on a computer. A diagram of the laser table can be seen in [JohnsonPhD].

2.6 Continuously variable grating period

The custom phase mask is designed to have many small areas with different periodicities of the square pattern. The periods available on a given pattern determine the TG periods that can be used in the experiment without changing the magnification of the imaging system. In theory the smallest TG period occurs when the crossing angle is 180° giving a period of $L = \lambda/2$. In reality, this is difficult to achieve with a phase mask, as it would not be possible to image the grating and gain all the benefits discussed above. For imaging, the grating period is determined by the numerical aperture of the imaging system. The higher the numerical aperture, the smaller the grating spacing that can be achieved. The largest grating spacing is limited by the size of the spot since diffraction only occurs if there are a few periods within the size of the spot.

For our experiments we use a two-inch diameter lens with a focal length of 7.5 cm, which results in a 0.32 numerical aperture [JohnsonPhD]. With our 515 nm/532 nm pump/probe wavelengths and our phase mask pattern, the grating period range is L = 1-50 um. The phase mask is divided into 28 different discrete segments with different periods. Having discrete sections makes switching between grating periods relatively easy. The phase mask is mounted on a rail to facilitate passing the pump and probe beams through selected segments of different periods. In many cases, it would be useful to have finer control over the TG period. A few techniques for generating continuously variable grating periods have been covered in the literature [Dadusc, Goodno, Terazima].

We have developed a novel method for easily generating a continuous range of TG periods. The range is still limited by the numerical aperture (short period) of the imaging system and the spot size (long period), but our method offers the ability to tune the grating period between any two adjacent patterns on the phase mask. To achieve this, we rotate the phase mask so that it is no longer perpendicular to the beam propagation axis. The exact crossing angles can be calculated using the standard grating equation, but in the limit of long phase mask period and small rotation angle the new grating period for a finite angle ϑ is well approximated by,

$$L' = L\cos\vartheta \tag{2.19}$$

where L' is the new TG period and L is the TG period for that phase mask pattern. We can visualize this relationship by determining the projection of the phase mask onto the image plane. As the grating is rotated the projection of the peaks of the phase mask get closer together in the imaging plane. The only modification needed is placing the phase mask on a rotation stage, where the pump and probe spots are centered on the rotation axis. A demonstration of this technique is presented in figure 2.5. There are a few issues that arise when the grating rotation angle is large. In addition to reduced first-order diffraction due to a larger zero order, the first order beams will no longer be equal in intensity. If the two first order beams are not the same intensity the resulting intensity profile will have a non-zero null, or a decreased extinction ratio. Another issue that could arise at large rotation angles is that the edges of the phase mask would no longer be in the image plane of the two-lens system causing a slight shift in the period of the intensity profile at the edges of the spot. This would only be a significant issue for angles greater than 45° or if the imaging system had a short depth of focus. We will demonstrate a useful application of this technique in section 6.6.

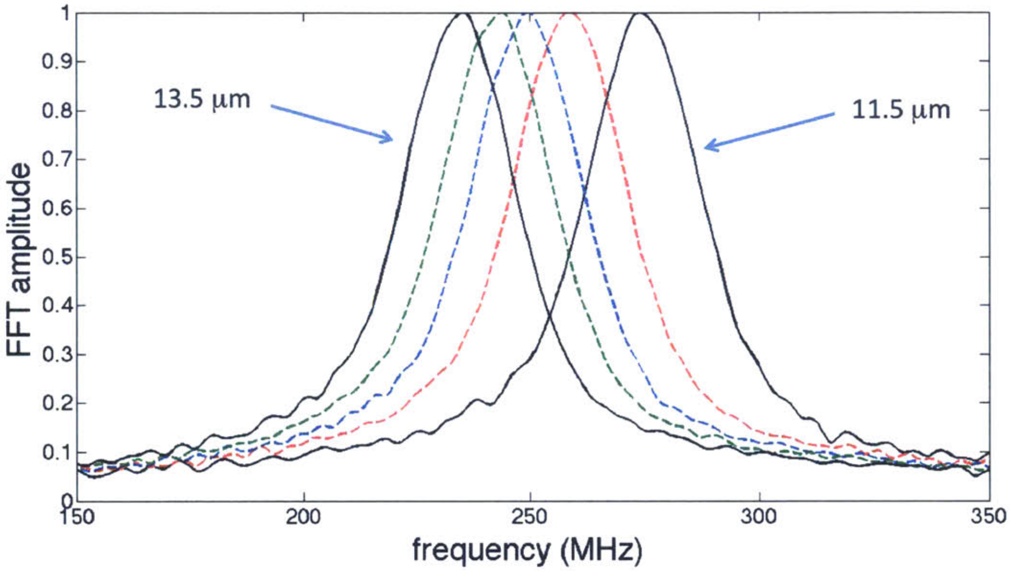

Fig 2.5. FFT amplitude for surface acoustic waves on a 100 nm Al film on a glass substrate. The dashed lines are taken with a base grating period of 13.5 μm but at $\vartheta = 15°$, 20° and 25° for green, blue and red traces respectively. By tuning from $\vartheta = 0°$ to ~35° we can continuously generate SAWs with wavelength ranging from 13.5 μm to 11.5 μm.

2.7 Summary

This chapter focused on introducing the TG experiment by discussing the generation and detection of a material response to crossed-beam excitation. We discussed the heterodyne detection scheme, the phase and amplitude grating components of the signal and a novel approach to generating a continuously variable TG period. The remainder of the thesis is focused on applying the TG technique to studying micro/nanoscale thermal transport in semiconductors and surface acoustic wave (SAW) propagation in granular materials.

Chapter 3

Thermal Transport in Non-Metallic Crystals

3.1 Introduction

In recent years a great deal of work has been focused on understanding thermal transport short distances [Cahill03, Cahill14, Koh, Highland, Siemens]. In non-metallic crystals, phonons are the predominant heat carriers, and the phonon mean free path (MFP) governs how far heat moves in the material [Ziman, Ashcroft, Chen05]. Understanding how phonons with a certain MFP contribute to thermal transport is essential for controlling thermal transport in a material. For example, designing materials with low thermal conductivity is a key component to increasing the efficiency of thermoelectric devices. The highest thermoelectric efficiency has been demonstrated for highly nanostructured materials [Poudel, Snyder, Dresselhaus, Chen03]. On the other hand, closely packed heat sources in microelectronic devices pose significant challenges for thermal management [Pop]. In this case, high thermal conductivity is desired to avoid overheating. The following chapter will introduce thermal conductivity and present experiments that shed light on the nature of thermal transport at short length scales and the MFP of phonons that contribute to thermal transport.

3.2 Thermal conductivity

3.2.1 Introduction to thermal conductivity

In the early 1800's Joseph Fourier performed pioneering work on thermal conduction [Fourier]. He concluded that over macroscopic distances, heat flux was proportional to the temperature gradient according to the following equation,

$$\vec{\boldsymbol{q}} = -k\nabla T \tag{3.1}$$

where $\boldsymbol{q}$ is the heat flux, ∇T is the temperature gradient and k is the thermal conductivity. In Fourier's theory he assumed that heat carriers move according to diffusion theory with the heat equation is given by,

$$\frac{\partial T}{\partial t} = \alpha \nabla^2 T \tag{3.2}$$

The diffusion equation relates the time dependence of the temperature profile to the second derivative in space of the temperature profile. The proportionality constant, α, is the thermal diffusivity related to the thermal conductivity as $\alpha = k/\rho c$, where ρ is the density of the medium and c is the specific heat at constant pressure. In diffusion the mean free path, or the average distance the heat carrier travels before it scatters, is much shorter than the length of the thermal profile.

In the mid 1800's kinetic theory was used to described heat transfer as molecular motion. Kinetic theory accurately determined the thermal conductivity of gasses as $k = ⅓C v \Lambda$, where C is the volumetric heat capacity (ρc), v is the average speed of the gas molecules, and Λ is the mean free path. This provides an intuitive picture for thermal conductivity, where C describes how much heat is carried, v describes how fast heat is carried, and Λ describes how far heat is carried. For gasses at high temperature and/or pressure, the transport is diffusive, where the mean free path is shorter than the temperature gradient. While this is useful for gasses, in solids heat is not carried by molecular translation since the atoms are locked in a lattice.

In the 1920's Peter Debye and Rudolf Peierls developed the theory of thermal transport in non-metallic crystals [Debye, Peierls]. In non-metallic solids, lattice vibrations, called phonons, carry the majority of heat. Phonons have a wide range of frequencies, and in a simple picture the thermal conductivity can be determined by summing up the contributions of all the phonons according to the following equation,

$$k = \frac{1}{3} \int_0^{\omega_{max}} C(\omega) v(\omega) \Lambda(\omega) d\omega \tag{3.3}$$

Here, $C(\omega)$ is the frequency-dependent heat capacity, $v(\omega)$ is the frequency dependent group velocity and $\Lambda(\omega)$ is the frequency dependent mean free path. The integration is performed over all phonon frequencies and a sum over polarizations is implied with the 1/3 factor accounting for three propagation directions. The modern day understanding of thermal conductivity is still largely based on the Debye-Peierls picture of thermal conductivity.

It is worth mentioning that the kinetic theory thermal conductivity expression can be derived from the semi-classical Boltzmann transport equation, shown in equation 3.4 for one dimension under the relaxation time approximation(RTA) [Majumdar93].

$$\frac{\partial f}{\partial t} + v_x \frac{\partial f}{\partial x} = \frac{f^0 - f}{\tau} \tag{3.4}$$

Here, f is the phonon distribution function, f_0 is the equilibrium phonon distribution, v_x is the phonon group velocity and τ is the single mode phonon relaxation time. The RTA has been the subject of much criticism, but more recently has been shown to work well for temperatures above 100K [Ward].

The heat capacity and group velocity can be calculated in a straightforward way as well as determined experimentally. The MFP, on the other hand, is not so simple to calculate as it depends on the interaction between a given phonon and all other phonons. It is also arguably the most important parameter when trying to understand the length dependent nature of thermal conductivity since it is directly related to how far a carrier of heat travels. The next section will briefly cover heat capacity and group velocity and then discuss attempts at calculating phonon MFPs.

3.2.2 Phonon dispersion

The collective lattice vibrations of a periodic crystal can be decomposed into normal modes called phonons. This is analogous to normal mode analysis of molecular vibrations. Phonon modes are described by their polarization (longitudinal or transverse), frequency, ω, and wavevector, $\boldsymbol{q}$. Phonons are quasi-particles that exhibit wave and particle like behavior, but are well described for our purposes by the classical wave equation. Using a primitive mass on a spring model the equations of motion provide a good approximation of the relationship between ω and $\boldsymbol{q}$ of each phonon mode, which is called the dispersion relation. The group velocity for each mode is the slope of the dispersion curve or $d\omega/d\boldsymbol{q}$, which for a linear dispersion is ω/q. More advanced calculations can also be done to obtain the dispersion relation with high accuracy. One such technique uses density-function perturbation theory (DFT) to determine the harmonic and anharmonic force constants and then determines ω and $\boldsymbol{q}$ from *ab initio* calculations [Deinzer03]. The dispersion for Si is presented in fig 3.1 adapted from [Ward].

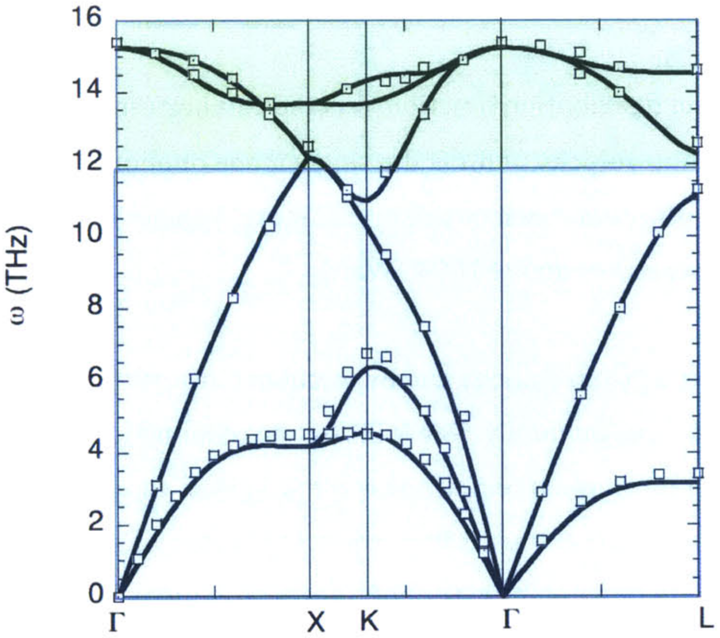

Fig 3.1 Dispersion relation for Si along the high symmetry directions adapted from [Ward]. The acoustic phonons are highlighted in blue and optical phonons highlighted in green. Open squares are data from [Nilsson]

Starting at the Γ point and moving toward X at low frequencies, we see two branches corresponding to the longitudinal acoustic (higher frequency) and two transverse acoustic phonon branches (lower frequency, but degenerate in this direction). The transverse acoustic branch splits at the X point revealing the two transverse modes. At much higher frequency there are addition modes corresponding to optical phonon modes (one longitudinal and two transverse). Phonon dispersion relations can be measured experimentally with neutron scattering [Nilsson].

3.2.3 Heat capacity

The heat capacity describes how much the temperature of a material will when a specified amount of energy is put into the material. Alternatively it is a measure of the relative energy contribution of phonons of a given frequency. Phonons are bosons, and their occupation number at a given temperature is described by the Bose-Einstein distribution. The heat capacity will also be dependent on the number of phonon modes available in the system or the density of states. For a 3D solid the density of states is given by $\boldsymbol{q}(\omega)^2/(2\pi^2 v(\omega))$, where $\boldsymbol{q}$ is the phonon wavevector and v is the phonon group velocity. The mode dependent heat capacity is then given by [Ashcroft],

$$C(\omega) = \hbar\omega g(\omega)\frac{\partial n(\omega, T)}{\partial T} \tag{3.5}$$

Where $g(\omega)$ is the density of states, and n is the phonon occupation number.

3.2.4 Phonon mean free path

Phonons interact with other phonons, electrons, and inhomogeneities in the crystal lattice such as isotopes, defects, grain boundaries or physical boundaries [Callaway, Holland63, Holland64]. When the phonon interacts with one of these objects it may be scattered and may create a new phonon with a new energy and/or wavevector. Phonon scattering by defects and grain boundaries in general behaves similarly to Rayleigh scattering and scales as ω^4. We consider a perfect crystal, and as a result defect scattering contributions will be neglected. The characterization of electron-phonon interactions is a large field in its own right [Ziman]. Typically for intrinsically doped semiconductors, electron-phonon scattering results in a small change in the intrinsic scattering rates [Ziman]. This leaves phonon-phonon interactions as the major factor that determines the mean free path.

For temperatures on the order of the Debye temperature the most common phonon-phonon interactions are three phonon interactions in which either two phonons of lower frequency combine to form one of a higher frequency or one of higher frequency decomposes into two lower frequency ones. Phonon scattering processes must follow momentum and energy conservation, $\boldsymbol{q} + \boldsymbol{q}' = \boldsymbol{q}''$ and $\omega + \omega' = \omega''$, but it is important to note that the phonon momentum is not a true momentum, rather it is a crystal momentum given by $\hbar\boldsymbol{q}$. The crystal momentum is periodic in the reciprocal lattice vector $\mathbf{G}$ and so a phonon with a crystal momentum $\hbar\boldsymbol{q}$ is indistinguishable from one with momentum $\hbar\boldsymbol{q} + \mathbf{G}$. In practice when examining phonon scattering events there are two possible situations, one where the sum of crystal momentum is less than the reciprocal lattice vector, $\boldsymbol{q}'' < \mathbf{G}$ and one where $\boldsymbol{q}'' > \mathbf{G}$, typically called normal(N) and umklapp(U) scattering processes respectively. It is commonly thought that umklapp processes provide the only source of thermal resistance for lattice thermal conduction [Callaway, Holland]. This is only true for specific conditions but in general both N and U processes contribute to thermal resistance [Maznev14]. The misconception arises due to the typical choice of the primitive unit cell. If the Brillouin zone is chosen to center around $q = 0$ then the combination of two large $\boldsymbol{q}$ acoustic phonons would exceed G and the resulting wavevector would point in the opposite direction resulting in a thermal resistance. In reality the choice of the Brillouin zone is arbitrary and while the interaction of such phonons would be a U process with that choice of the Brillouin zone it could be N in another. The fact that N and U processes both contribute to thermal resistance is seen in [Ward] where the phonon lifetime is given by the following expression $1/\tau = 1/\tau_N + 1/\tau_U$ indicating that N and U processes are indistinguishable.

Using the kinetic theory approach to thermal conductivity, $k = \frac{1}{3}Cv\Lambda$, the phonon MFP Λ can be calculated. The textbook value of the average MFP for many semiconductors is in the range of 10 nm to 100 nm [Blakemore, Burns]. This suggests that thermal transport will be diffusive for all but the very shortest thermal transport length scales. But the average value of mean free path doesn't give an accurate picture of the wide range of MFPs present in the phonon distribution, and how the phonons in the distribution contribute to thermal transport. Early experimental and theoretical work studying the phonon MFP at room temperature showed that phonons which contribute to thermal transport can be much larger than the average MFP [Ju,Chen96]. More recently molecular dynamics [Henry] as well as first-principles calculations have had a great deal of success in calculating phonon MFPs [Broido, Ward, Esfarjani10]. Calculations for Si are shown in fig 3.2 adapted from [Esfarjani10]

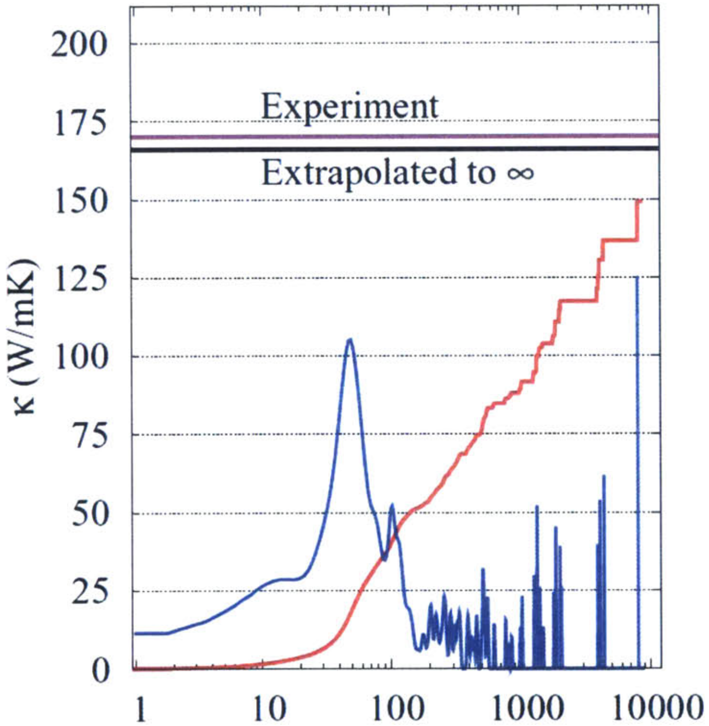

Fig 3.2 Taken from [Esfarjani10]. Differential (blue) and Cumulative (red) thermal conductivity for silicon at 277 K. The units on the y axis apply to the cumulative distribution and the differential is shown for comparison.

There are two instructive ways to visualize the contribution of phonons with a given MFP. The differential thermal conductivity, plotted in blue in fig 3.2, describes the contribution of phonons within any small range of MFPs, Λ to $\Lambda + d\Lambda$. By looking at the differential distribution it seems reasonable that the average MFP would be under 100 nm just like the textbook value. Integrating the differential thermal conductivity up to a cutoff MFP, Λ_c results in the cumulative thermal conductivity. The cumulative thermal conductivity, plotted in red in fig 3.2, describes how much phonons up to Λ_c contribute to the thermal conductivity. This provides a very different picture than the average mean free path in which around 50 percent of thermal conductivity can be attributed to phonons with mean free path greater than 1 μm at room temperature.

3.3 Experimental observations of non-diffusive thermal transport

Departure from diffusive thermal transport has been observed as ballistic heat propagation at cryogenic temperatures [Wolfe]. More recently a number of experiments have been aimed at observing non-diffusive thermal transport in non-metallic crystals near room temperature [Minnich11, Johnson13, Regner13]. In order to reach the non-diffusive thermal transport regime the thermal gradient imposed by the experiment should approach the MFP of the phonons contributing to thermal transport. In each of the three papers listed above this is achieved in three different ways. In [Minnich11] they used a time-domain thermoreflectance technique (TDTR). TDTR is pump-probe measurement technique that uses fs laser pulses for both pump and probe with a scanning delay line to measure the time dependent changes in reflectivity due to heating from the pump pulse. To change the thermal transport length scale they reduced the spot size of the laser and observed a reduction in the thermal conductivity they extracted, although only significant deviations were observed only at temperatures below 100K. In [Regner13] they used frequency-domain thermoreflectance (FDTR). FDTR is a very similar experiment to TDTR as they are both measuring changes in reflectivity as a function of temperature, but in FDTR a cw laser is modulated sinusoidally at high frequencies upwards of 200 MHz. In the diffusion model a temporally periodic heating of the surface results in a spatially decaying thermal profile into the depth of the material. They measured the phase and amplitude of the thermoreflectane response at the surface and related that to the thermal conductivity of the material. The length of the thermal profile, termed the thermal penetration depth, is inversely proportional to the modulation frequency. As the frequency increases the thermal penetration depth decreases leading to a short thermal transport length scale. Regner et. al. observed that as the modulation frequency increased, the thermal conductivity decreased indicating non-diffusive transport due to the thermal length scale being shorter than some of the phonon MFPs.

In both [Regner13] and [Minnich11], thin metal films are used as transducers to avoid unwanted electron responses. This is accounted for in their modeling but it has become clear that significant non-equilibrium effects are present in these systems and the results are not entirely unambiguous [Choi, Vermeersch]. In addition thermal boundary resistance occurs when heat flows from one material to another and is still a significant hurdle in nanoscale thermal transport measurements [Kapitza, Capinsky, Cahill03].

3.3.1 Measurement of thermal transport with the TG technique

When two short pump pulses are crossed in a bulk sample, as in the TG technique, the resulting sinusoidal thermal profile resembles planes of heat with period equal to the transient grating period q. If the crossing depth is much larger than the grating period then 1D thermal transport will occur from the grating peaks to nulls. When the grating period is longer than the MFP of the heat carriers the transport follows the diffusion equation [Carslaw]. To analyze the kinetics of the thermal transport we can solve the 1D heat diffusion equation with spatially periodic excitation given as,

$$\frac{\partial \Delta T_{x,t}}{\partial t} = \alpha \frac{\partial^2 \Delta T_{x,t}}{\partial x^2} + \frac{Q}{\rho c_p} \cos(qx)\delta(t) \tag{3.6}$$

where $\Delta T_{x,t}$ is the pump-induced deviation in the equilibrium temperature, and α is the thermal diffusivity. The first two terms are the 1D heat diffusion equation and the third term is the TG heat source. Q is the energy deposited by the laser, ρ is the density and c_p is the specific heat. To solve the equation we assume that $\Delta T_{x,t}$ is spatially periodic following the heat source and Fourier transform in both space and time to obtain the following result,

$$\Delta \tilde{T}_{q,\omega} = \frac{Q}{\rho c_p} \frac{1}{(i\omega + \alpha q^2)} \tag{3.7}$$

Then, we can inverse Fourier transform to obtain the time dependent solution

$$\Delta T_{q,t} = \frac{Q\sqrt{2\pi}}{\rho c_p} exp(-\alpha q^2 t) = \frac{Q\sqrt{2\pi}}{\rho c_p} exp(-\gamma t) \tag{3.8}$$

The decay rate γ of the periodic thermal profile is determined by the thermal diffusivity of the material and the grating wavevector squared. In a typical TG experiment we measure the time dependent diffraction for a set grating wavevector and by fitting the experimental time trace to a single exponential, we can determine the thermal diffusivity as $\alpha = \gamma/q^2$. This simple approach to determining the thermal diffusivity for a bulk material was demonstrated in [Schmidt08] for a nanofluid of alumina nanoparticles suspended in decane. The diffusion model works well for a liquid where the heat carriers have very short MFP. In a non-metallic crystal as we discussed above the MFP is much longer, and in this case the transport may no longer be diffusive on micron length scales. The rest of this chapter will focus on observations of non-diffusive thermal transport using the TG technique.

3.3.2 Non-diffusive transport in a 400 nm Si membrane

For common semiconductors such as silicon and gallium arsenide the penetration depth for optical light at 532 nm is 1.7 μm and 125 nm respectively. It is clear that with such short penetration depths, that realizing a 1D transport regime with green light is not possible in a thick sample. To reach the 1D transport regime it is necessary to get samples with thicknesses on the order of the penetration depth of the light. Such samples exist in the form of freestanding silicon membranes, which were fabricated for us by collaborators at the Catalan Institute of Nanotechnology. The details of the fabrication procedure are contained in [Johnson13]. A 400 nm silicon membrane is thin enough to allow the light to pass through and set up the 1D thermal transport regime. Transmission TG experiments were carried out on the membrane as described in Chapter 2 and the resulting time traces for grating periods of 3.2 μm – 18 μm are shown in Fig 3.3, adapted from [Johnson13].

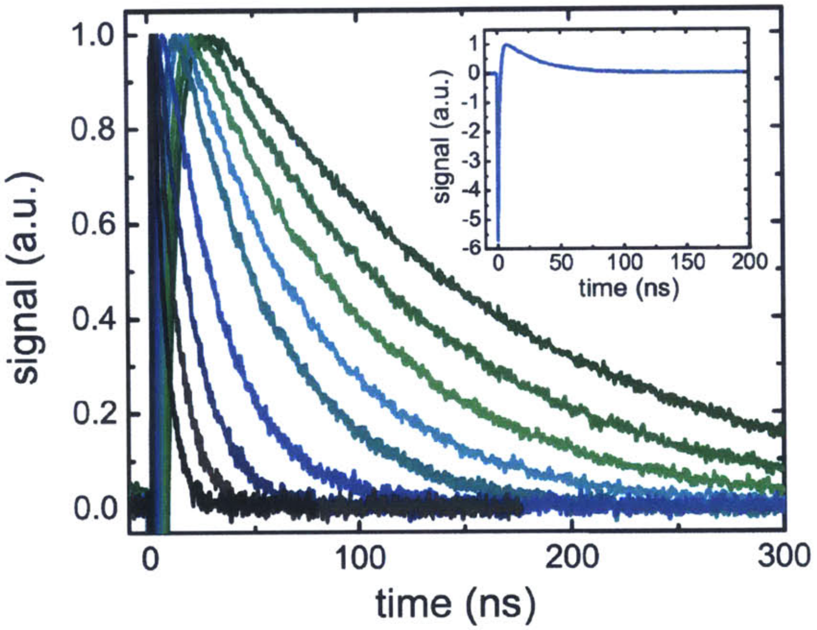

fig 3.3 Taken from [Johnson13]. Time traces of the thermal decay in a 400 nm membrane with grating period ranging from 18 μm (dark green, longest decay) 3.2 μm (black, shortest decay). A full trace for 7.5 μm is shown in the inset.

As the transient grating period gets shorter, the decay time decreases. The figure only depicts the thermal portion of the decay but the full diffracted signal is shown in the inset to fig 3.3. The optical excitation in the membrane promotes carriers from the valence band high into the conduction band. The hot carriers quickly relax to the bottom of the conduction band through electron-electron scattering and electron-phonon scattering. Although this process is on the order of a few picoseconds, the carriers at the bottom of the conduction band can have μs life times [Orthonos]. The periodic electron distribution also modulates the complex transmission function and contributes to the diffracted signal seen as the sharp negative spike in the inset of fig 3.3. The periodic electron density distribution also relaxes through diffusion. Since the ambipolar diffusion constant is an order of magnitude faster than the thermal decay, the electronic component can be separated in time from the thermal decay [Li]. In practice we fit the time traces to bi-exponential function to account for the electron diffusion contribution and extract the decay rate of the thermal profile.

For thermal diffusion we expect that the decay rate is proportional to the TG wavevector squared. The extracted decay rate as a function of grating wavevector is plotted in fig 3.4

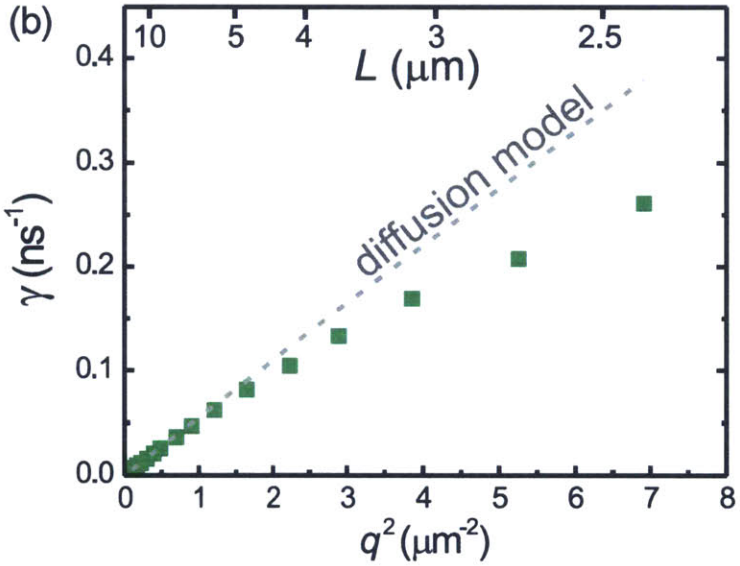

fig 3.4 Decay rate as a function of TG wavevector (TG periods 2.5 -24 μm)

For long grating spacing we can see that the decay rate follows the expected q^2 dependence. As the grating spacing decreases below 15 μm the decay rate deviates from the diffusion model indicating the onset of non-diffusive transport. At the onset of non-diffusive transport a portion of the phonons have mean free path longer than the transient grating period.

3.3.3 Modeling non-diffusive transport in the TG geometry

One great benefit of the TG technique is that the simple sinusoidal spatial profile of the temperature makes analytical theoretical analysis possible. In fact it is even possible to solve the notoriously difficult Boltzmann transport equation for this geometry [Maznev13,Collins14]. To make headway on analyzing non-diffusive transport a link between the experimental length scale and the phonon MFP needs to determined. Maznev *et. al.* derived an analytical expression for this relationship hereafter called the suppression function shown in equation 3.9.

$$A(q\Lambda) = \frac{3}{q^2\Lambda^2}\left[1 - \frac{\arctan(q\Lambda)}{q\Lambda}\right] \tag{3.9}$$

A is termed the heat flux suppression function, q is the TG wavevector, and Λ is the phonon MFP path. The heat flux suppression function describs how much a phonon with a given MFP contributes to the decay of the transient thermal grating.

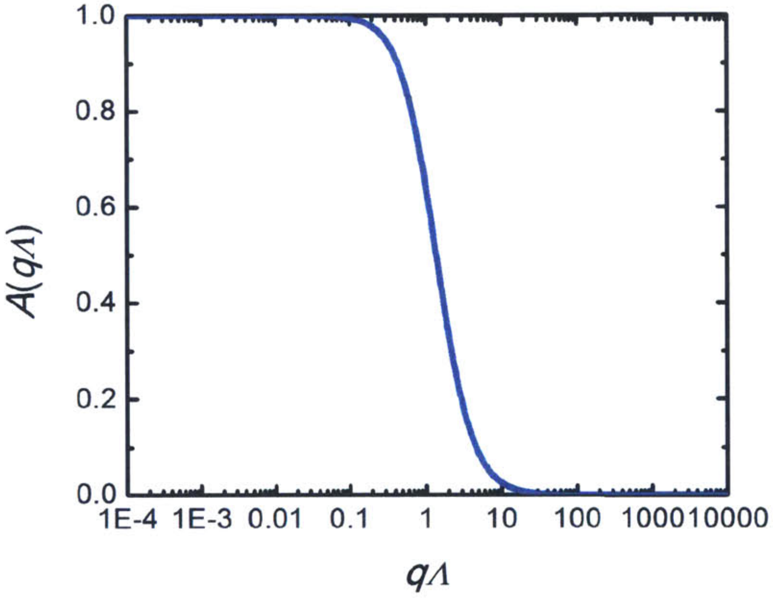

fig 3.5 Plot of the heat flux suppression function for the transient grating geometry (*A* from equation 3.9). The graph shows how much a phonon with a certain MFP contributes to the heat flux at a grating wavevector *q*.

For $q\Lambda \ll 1$ the phonon MFP is much shorter than the TG period giving a value of $A = 1$ meaning the heat flux remains the same as predicted by the diffusion model. For $q\Lambda \gg 1$ the phonon MFP is much longer than the TG period and $A = 0$ meaning the heat flux is reduced compared to the prediction of Fourier's law. Although it appears that phonons with long MFP don't contribute to the grating decay, it really means that in order to recover an accurate heat flux for the non-diffusive regime the contribution of ballistic phonons should be set to zero.

To apply this to our measurements we can calculate the thermal conductivity for a given grating spacing by multiplying the heat flux suppression function and the 0group velocity, density of states and mean free path for all phonon modes. Recent first-principles calculation results have calculated these quantities [Ward, Esfarjani10]. The thermal conductivity calculated for each grating spacing is given by

$$k(q) = \int_0^{\omega_{max}} \frac{1}{3} A(q\Lambda) C_\omega v \Lambda d\omega. \tag{3.10}$$

Using the experimental TG decay rates we determine the experimental thermal conductivity as $k(q) = \gamma/(\rho c_p q^2)$. The experimental data along with the calculated thermal conductivity using MFPs determined from molecular dynamics simulations from [Henry] are plotted together in fig 3.6.

We see good agreement between the theory and experiment showing a reduced effective conductivity at short grating periods. It is important to note that although we see a reduced conductivity, the decay rate of the thermal profile is always increasing with decreasing grating spacing. But unlike diffusion, the decay rate doesn't scale like q^2 resulting in a reduced effective conductivity.

The data presented in fig 3.6 are divided by the bulk value of thermal conductivity for Si, and the ratio doesn't reach unity. The reason it doesn't reach unity is due to phonon scattering at the top and bottom surfaces of the membrane. Such size effects are well documented in the literature [Marconnet13]. Phonon boundary scattering in a membrane will be covered in more detail in the next chapter.

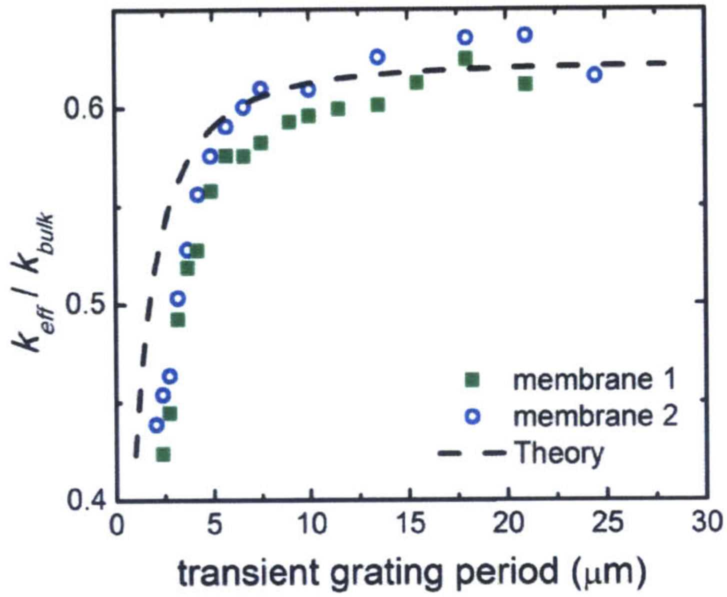

fig 3.6 Experimental thermal conductivity from two ~400 nm Si membranes in green and blue points. Black dotted line is the theoretical prediction using MFP information from [Henry] analytical suppression function from [Maznev] and following equation 3.10.

3.4 Thermal conductivity measurements in bulk materials

In the previous section we described a method for measuring the thermal conductivity of semiconductors by reducing the thickness of the sample to allow the excitation light to pass all the way through. This technique works well for Si which has a relatively long penetration depth of 1.7 μm at 532 nm. But for other semiconductors such as GaAs, which has a penetration depth of 125 μm at 532 nm, preparing a sample with thickness much smaller than the penetration depth is not practical. In addition phonon boundary scattering in thin films will cause significant deviations from the bulk thermal conductivity. In order to study bulk materials we need to create a temperature profile at the surface of the sample. In this case heat flows between the peaks and nulls of the grating and into the depth of the material. Although the 2D thermal transport regime is more complicated we can still use the TG technique to measure thermal conductivity of bulk materials.

3.4.1 TG measurements in reflection

Only a small modification of the setup is necessary for measurements in opaque samples. The modified setup is shown in fig 3.7.

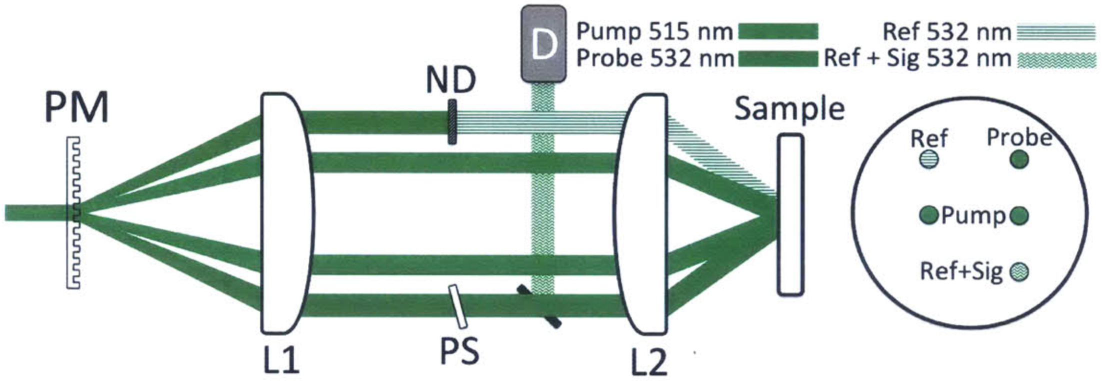

fig 3.7 Schematic illustration of the beam geometry for reflection mode. PM is optical phase mask, PS is phase control for heterodyne detection, ND is a neutral density filter to set the attenuation of the reference beam, D is the APD photodetector. L1 and L2 are the imaging lenses for the TG geometry. The circle on the right depicts a face on view of L2 showing that the probe and ref beam enter the lens above the pumps and with the sample at normal incidence. The ref plus signal returns underneath the pump, hits a pickoff mirror and is sent to the detector.

The reflection geometry is almost identical to the transmission geometry shown in fig 2.1. The major difference is that the diffracted signal combined with the reference beam is reflected back through the second imaging lens L2. A pickoff mirror is placed to direct the ref + sig to the detector.

The major difference comes when analyzing the TG signal, which requires solving the 2D heat equation with a periodic heat source presented in eq 3.11.

$$\frac{\partial \Delta T_{x,z,t}}{\partial t} = \alpha_x \frac{\partial^2 \Delta T_{x,z,t}}{\partial x^2} + \alpha_z \frac{\partial^2 \Delta T_{x,z,t}}{\partial z^2} + \frac{Q}{\rho c_p} \cos(qx) \exp(-\zeta z) \delta(t) \qquad (3.11)$$

Here x is the grating dimension, z is the direction into the depth of the sample, ΔT is the temperature rise induced by the pump, ρ is the density, c_p is the specific heat, Q is the energy absorbed by the sample, q is the grating wavevector magnitude and the finite penetration depth of the laser light is $1/\zeta$. The thermal diffusivity in the grating dimension and into the depth of the material is α_x and α_z respectively. Solving this equation takes a similar approach to what was done in section 3.2.1 and is detailed in [JohnsonPhD, Johnson12]. We start with a Fourier transform in x and t and solve the second order differential equation in z giving the analytical frequency domain solution,

$$\Delta\tilde{T}_{q,z,\omega} = \frac{Q}{\varphi^2 - \zeta^2}\left[\exp(-\zeta z) - \frac{\zeta}{\varphi}\exp(-\varphi z)\right], \tag{3.12}$$

where $\varphi = \frac{1}{(i\omega + \alpha q^2)}$.

A numerical inverse Fourier transform recovers the time domain solution,

$$\Delta T_{q,z,t} = A f_{z,t}[\cos(qx)\exp(-\alpha_x q^2 t)], \tag{3.13}$$

where A is the amplitude and $f_{z,t}$ is the decay into the depth of the material given in [Johnson12]. In the diffusion model the in-plane and cross- plane contributions to the decay are decoupled and in equation 3.13 we see the 1D solution in x multiplied by the cross plane component. If we neglect the finite penetration depth of the probe we can recover the surface temperature solution,

$$\Delta T_{q,z=0,t} = A\exp(\alpha_z \zeta^2 t)\mathrm{erfc}(\zeta\sqrt{\alpha_z t})[\cos(qx)\exp(-\alpha_x q^2 t)] \tag{3.14}$$

where erfc is the complementary error function. In the limit of surface heating, $(1/\zeta \to 0)$ the surface temperature has the following result,

$$\Delta T_{q,z=0,t} = A(\alpha_z t)^{-1/2}[\cos(qx)\exp(-\alpha_x q^2 t)] \tag{3.15}$$

Eq. 3.15 provides a useful form for interpretation of the TG signal. In general it is difficult to exactly determine the amplitude factor A, since it depends on the absorbed laser power, which is not known exactly, and is difficult to measure. As a result, the cross plane factor $(\alpha_z t)^{-1/2}$ can't be fit accurately, and we rely on the in-plane exponential decay to recover the thermal diffusivity in the x direction. The form of the surface heating solution makes it difficult to accurately determine the thermal properties of low diffusivity materials or to use long grating periods, because at long times, the signal is dominated by the slow $t^{-1/2}$ decay.

3.4.2 Phase and amplitude grating in reflection

In Chapter 2 we discussed the various components of the TG signal, namely phase and amplitude grating contributions to diffraction. As a reminder, the diffracted signal has contributions from both phase and amplitude gratings. For reflection, the phase grating is a combination of changes in the imaginary part of the reflectivity and surface displacement, while the amplitude grating is the real part of the complex reflectivity. It is assumed that both the real and imaginary parts of the complex reflectivity have the same time dependence which directly follow the surface temperature, but the surface displacement has a different time dependence. For an isotropic material the surface displacement in the z direction is given by [Käding] as,

$$u = B\mathrm{erfc}\left(q\sqrt{\alpha t}\right) \tag{3.16}$$

where B is the amplitude of the surface displacement, q is TG wavevector, and α is the thermal diffusivity of the material. In principle is it possible to account for both the surface displacement and surface temperature response, but it would be easier to isolate the temperature response. This can be achieved though heterodyne detection as described in Chapter 2. Heterodyne phases of 0, π and π/2, −π/2 will isolate the phase and amplitude grating respectively. Representative phase and amplitude grating signals for a PbTe thin film are shown in fig 3.8 adapted from [Johnson12].

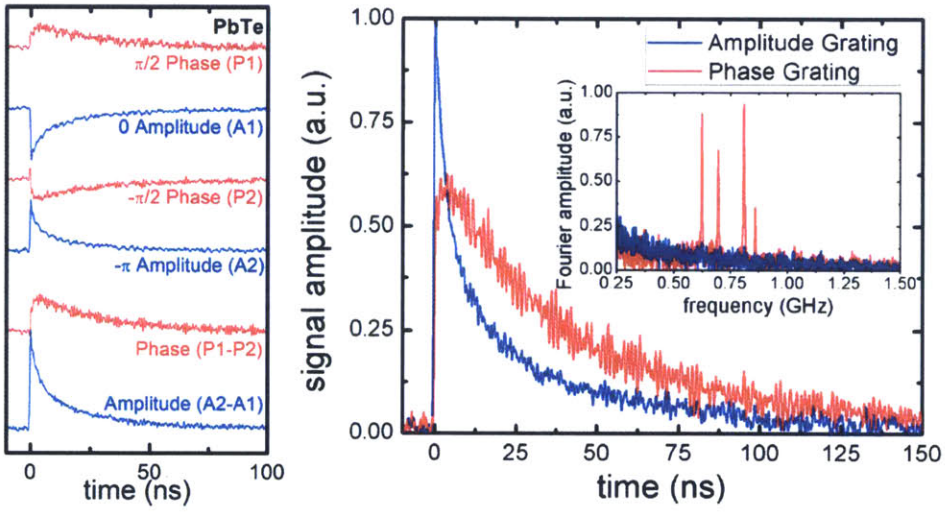

fig 3.8 Adapted from [Johnson12] (left) Reflection mode TG signals for a PbTe thin film showing the phase grating π/2 and −π/2 and from the amplitude grating, 0 and π, as well as the subtracted traces. (right) The subtraced traces are presented with the Fourier transforms shown in the inset. The oscillations in the phase grating are indicative of the surface displacement response from the generated surface acoustic wave.

The thermal diffusivity of the material can be unambiguously determined by isolating the amplitude grating signal with heterodyne detection and fitting using the form of the surface temperature in eq 3.15. The next two sections detail experiments aimed at observing non-diffusive transport in bulk materials.

3.4.3 Non-diffusive thermal transport in bulk GaAs

Transient grating experiments on bulk GaAs were carried out from 2.05 μm to 10 μm grating periods. The time traces are presented in fig 3.9. The amplitude grating data were fit with the surface temperature solution (eq 3.15) which matches the full solution after t = $(4\alpha_z\zeta^2)^{-1}$. Using a bulk literature value for GaAs of α_z = 22 mm^2/s [Adachi] and $1/\zeta$ = 125 nm (the optical penetration depth), t is found to be ~17 ns. We start the fit after 10 ns to account for finite penetration depth of the pump and to reduce the effects of carrier contributions to the signal. Time traces from the TG technique are shown in fig 3.9. The extracted decay rates plotted as a function of TG wavevector are shown in fig 3.10

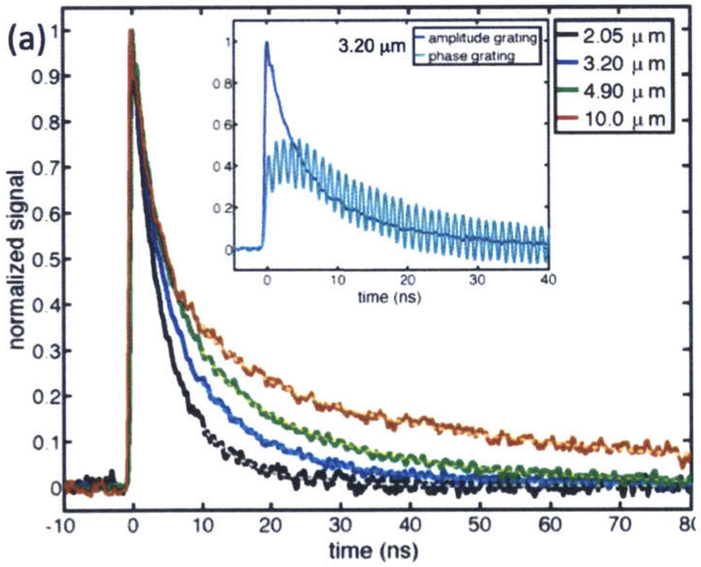

Fig 3.9 TG time traces for bulk GaAs collected in the reflection geometry for a variety of grating periods. The dotted lines indicate the fits to the surface temperature solution (eq 3.15). The inset presents the phase and amplitude grating signals for a TG period of 3.20 μm.

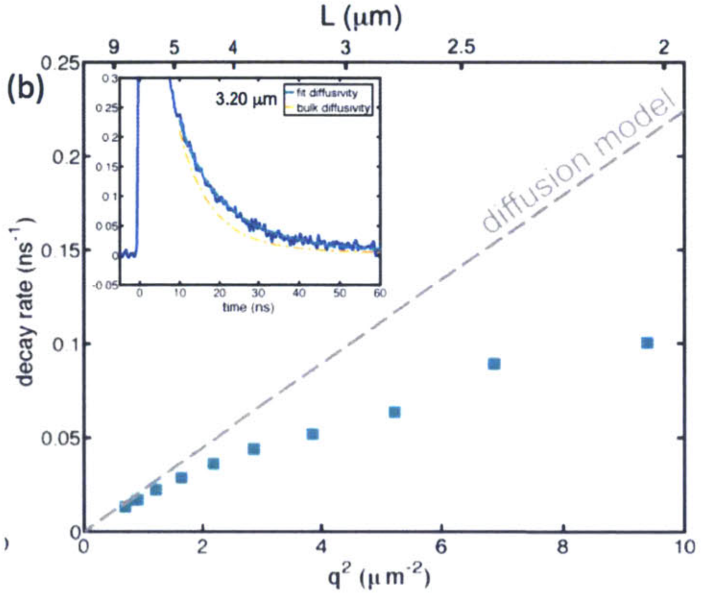

fig 3.10 TG decay rates plotted as a function of TG wavevector squared. The dashed line shows the expected decay rate in the diffusion model for bulk diffusivity from [Adachi]. The inset shows the fit with an adjusted decay rate and one that matches the diffusion model.

As in the 400 nm Si membrane, we observe a strong deviation from the diffusion model as the TG period decreases. The deviation from the diffusion model is attributed to presence of phonons with MFP longer than the TG period. In this case, the contribution of phonons with long MFP is reduced compared to the diffusion model resulting in a smaller decay rate. This indicates the wide distribution of phonon MFPs in GaAs. In fact, we observe the deviation from Fourier law occurring at even longer TG periods than in the Si membrane (up to 10 um at room temperature). Using the expression in eq 3.10 we can calculate the thermal diffusivity as a function of TG period using the first-principles results from [Luo] and compare with our experimental measurements. The experimentally determined diffusivity along with calculated diffusivity for each grating period is shown in fig 3.11.

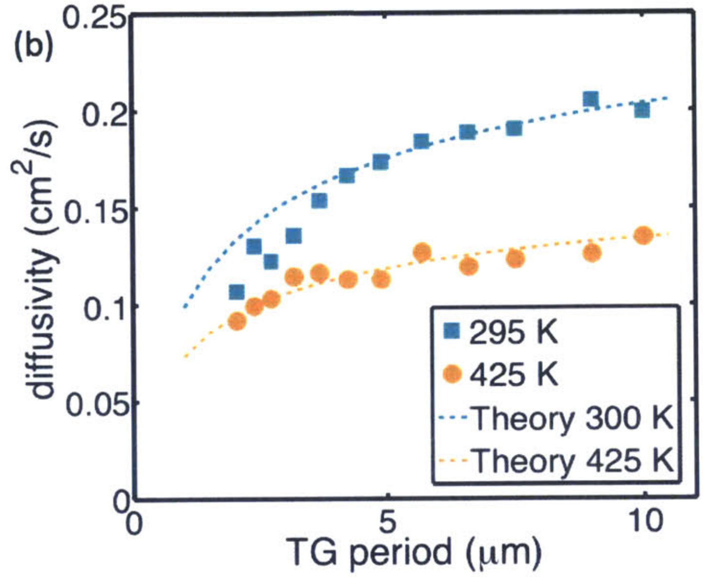

fig 3.11 Thermal diffusivity collected as a function of grating period from 2.5 μm to 10 μm. Data at 295 K and 425K show evidence of non-diffusive thermal transport. Theoretical curves use calculations from [Luo] show good agreement with experimental data.

Data from bulk GaAs at room temperature and elevated temperature show evidence of non-diffusive thermal transport on micron length scales. Comparison with theoretical calculations, confirm the broad nature of the MFP distribution in bulk GaAs. These experiments demonstrate the capability to observe non-diffusive effects in reflection mode TG measurements. The next section will detail the attempts to observe non-diffusive effects in materials relevant for thermoelectric devices.

3.4.4 Results for promising TE materials (PbTe and Bi_2Te_3)

The broad distribution of phonon MFPs in semiconductors has been observed experimentally with the TG technique in Si and GaAs. Indeed, first-principles calculations show that roughly 50% of heat is carried by phonons with MFP > 1 μm at room temperature. These calculations are relatively simple for materials such as Si and GaAs, but it is much more difficult to calculate the phonon MFP distribution in materials with complex crystal structures such as promising thermoelectric (TE) materials. TE materials typically have a very low intrinsic thermal conductivity as thermal conduction in TE devices degrades performance [Tian13]. Strategies to reduce the thermal conductivity involve alloying and nanostructuring by introducing a high concentration of defects and grain boundaries. The highest thermoelectric performance has been achieved in highly nanostructured materials [Chen03]. To aid in the design of more efficient TE materials it would be useful to determine the MFPs of heat carrying phonons in relevant materials. The calculated MFP distribution for a variety of materials is presented fig 3.12 adapted from [Tian13].

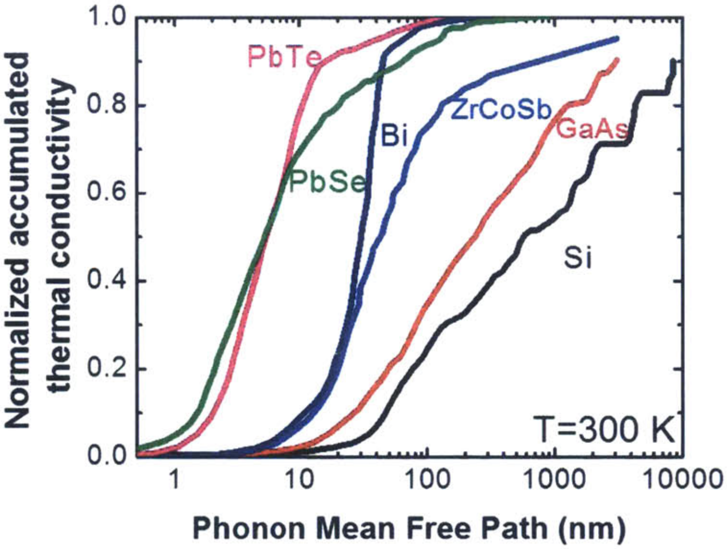

fig 3.12 Taken from [Tian13]. Thermal conductivity accumulation calculated for a variety of semiconductors.

Looking at the curve for PbTe, a promising TE material, the MFP distribution is centered at a much shorter MFP than silicon. This is not surprising since PbTe has a low thermal conductivity at room temperature ~2 W/mK, compared to 148 W/mk for silicon. The low thermal conductivity can be attributed to strong anharmonic potentials in PbTe leading to a large degree of phonon-phonon scattering and shorter phonon MFPs [Delaire11]. As we demonstrated previously, the TG technique is well suited to investigate length dependent thermal conductivity. If the TG period is on the same length scale as the phonon MFP, the TG decay rate deviates from the predictions of Fourier's Law and the result can be observed as a decrease in the effective conductivity.

We made TG measurements on two potential TE materials, PbTe and Bi_2Te_3. The single crystal bulk PbTe was obtained from Oak Ridge National Laboratories and was polished on one side. The Bi_2Te_3 sample was cleaved along the C-axis to provide a surface with good optical quality. Preliminary measurements of the thermal conductivity of PbTe and thermal diffusivity of Bi_2Te_3 are presented in fig 3.13

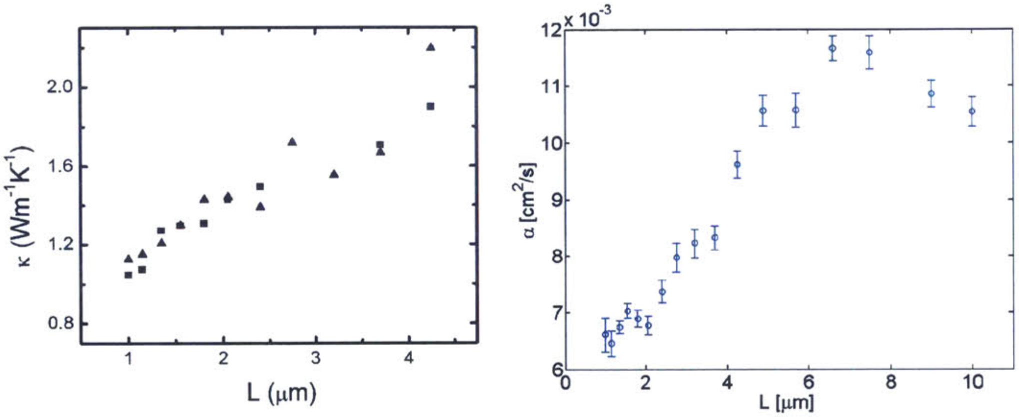

fig 3.13. (Left) Thermal conductivity for single crystal PbTe for grating periods of 1 -4 μm. At large grating period the thermal conductivity is in good agreement with the literature value of ~ 2 W/mK [Tian12] (right) Thermal diffusivity for Bi_2Te_3. The long grating period limit is in good agreement with the literature value for thermal diffusivity of 0.01 cm^2/s

At long TG periods the measured thermal conductivity of PbTe approaches the literature value of 2 W/mK [Tian12]. The same is true for Bi_2Te_3 with the thermal diffusivity approaching the literature value of ~0.01 cm^2/s [Satterthwaite]. For both PbTe and Bi_2Te_3 we observe a decrease in the thermal conductivity as the grating period gets smaller. This is a surprising result as the mean free path distribution for these materials is dominated by short MFP phonons [Tian12, Wang]. The measurements were carried out in open air and since the materials have such a low conductivity, it is possible that the air contributes to the thermal decay signal and modifies the measured decay. Both data sets were fit with the surface temperature solution but the ambipolar diffusion constants are not well known for our materials and thus it is possible electron diffusion could influence the measured signal altering the decay rate. To obtain more useful results on TE materials it would be best to measure the samples in an evacuated cryostat to eliminate the contribution from air. In addition, measurements at low temperature where the MFPs that contribute to thermal transport are longer will provide more conclusive results on observing non-diffusive effects in TG measurements in promising TE materials.

3.5 Summary

In this chapter we introduced thermal transport measurements using the TG technique for both transparent and opaque samples. When the transient grating period is long compared to the MFP of heat carrying phonons, the transport is diffusive and the decay rate of the period thermal profile scales as the TG wavevector squared. When the grating period becomes comparable to the phonon MFP the TG decay rate deviates from the diffusion model due to the onset of non-diffusive transport. Non-diffusive transport has been observed in a 400 nm Si membrane and in bulk GaAs at room temperature for TG Periods of ~5 mm and 10 mm respectively. These results indicate the large role of long MFP phonons in thermal transport at room temperature. Our results are in agreement with first-principles calculations of phonon MFPs, and confirms the broad nature of the MFP distribution for Si and GaAs where calculations indicate that phonons with MFP >1um account for 40% and 25% of the thermal conductivity respectively. TG measurements are useful for observing the onset of non-diffusive behavior but it is challenging to extract useful quantitative information of phonon MFPs due to the limited length scales achievable (1-50 μm). The next section will detail an approach using thin films to extract the full MFP distribution from thermal conductivity measurements.

Chapter 4

Recovering Phonon MFP Contributions to Thermal Transport

4.1 Introduction

In chapter 3 we demonstrated that the MFPs of phonons that contribute to thermal transport in non-metallic crystals at room temperature are much larger than expected based on text book values of the average MFP. Indeed first principles calculations of thermal conductivity demonstrate the broad nature of the distribution of phonon MFPs [Ward, Esfarjani10], but further experimental validation of the calculations is needed. One experimental approach to determining the phonon MFP is to directly measure the frequency dependent phonon lifetime. This can be achieved with a variety of techniques including inelastic scattering of neutrons [Ma], X-rays[Shukla], and visible light[Rozas], or by laser-generated coherent phonons [Maznev13b, Cuffe13]. Direct measurements of phonon lifetimes are limited by the resolution of the instrument in the case of neutrons and X-rays or by the difficulty of generating high-frequency coherent phonons. For example, in silicon phonon lifetimes have been measured up to 100 GHz [Daly], but phonons thought to contribute significantly to thermal transport have frequencies above 1 THz [Esfarjani10].

Other experiments for determining phonon MFPs measure the thermal conductivity over a range of thermal length scale by varying the diameter of the optical spot [Minnich11], the spacing of a periodic interference pattern [Johnson13], the width and spacing of a metal line or dot pattern [Siemens, Hoogeboom-Pot,] or the frequency of a modulated light source [Regner13]. The heat flux of phonons with MFP longer than the imposed thermal length scale is smaller than predicted by the Fourier law, resulting in a reduced effective thermal conductivity, which is determined using the heat diffusion equation. The reduced thermal conductivity as a function of length scale provides information on which phonons contribute to the thermal transport. The difficulty in determining the MFP distribution comes from modeling the relationship between MFP and heat flux reduction, typically called the suppression function. Simplistic approximations are often made that cut off the contribution of phonons with MFP over a certain value, typically the experimental length scale. Other approaches involve solving the Boltzmann transport equation for the specific experimental geometry. This is challenging since some geometries involve multiple thermal length scales and the presence of metal transducer layers which complicate the interpretation non-diffusive measurements. Even experiments with analytical solutions to the BTE, such as the TG technique [Johnson13, Maznev13], are limited to relatively long thermal length scales by the optical interference pattern, typically on the micrometer length scale.

In this chapter we present an alternative method for determining the phonon MFP from measurements of thermal conductivity. Rather than using observations of non-diffusive thermal transport, we make measurements of diffusive thermal transport in nanoscale membranes. The scattering of phonons at the boundaries of the membranes reduces the phonon MFPs in the membrane resulting in a reduction of the thermal conductivity based on the thickness of the film. Nanoscale membranes also offer access to length scales on the order of 10 nm [Shchepetov].

This chapter will begin by discussing measurements of in-plane thermal conductivity of silicon membranes with thicknesses ranging from 15 nm to 1500 nm. Then we discuss phonon boundary scattering in the membrane and the Fuchs-Sondheimer suppression function. Then, the experimental measurements are compared to similar experiments from the literature as well as first principle calculations. Next, we present the reconstruction of the room temperature MFP distribution, and conclude with measurements on nanoscale membranes at low temperatures. The majority of this chapter aside from the low temperature measurements is contained in [Cuffe15].

4.2 In-plane thermal conductivity of Si membranes

The in-plane thermal conductivity of a series of silicon membranes was measured using the TG technique described in chapter 2. The thickness of the silicon membranes ranged from 15 nm to 1518 nm . The membranes were fabricated from 150 mm silicon-on-insulator(SOI) wafers using techniques common for processing wafers for MEMS [Shchepetov]. The top silicon layer is thinned by repeated oxidation and removal of oxide until the layer reaches the desired thickness. Then, using a combination of wet and dry etching the substrate and buried oxide are etched away leaving free standing layers with an area of ~500 μm x 500 μm. The thickness of each membrane was measured using a reflectometer achieving an accuracy of better than 1 nm [Cuffe14].

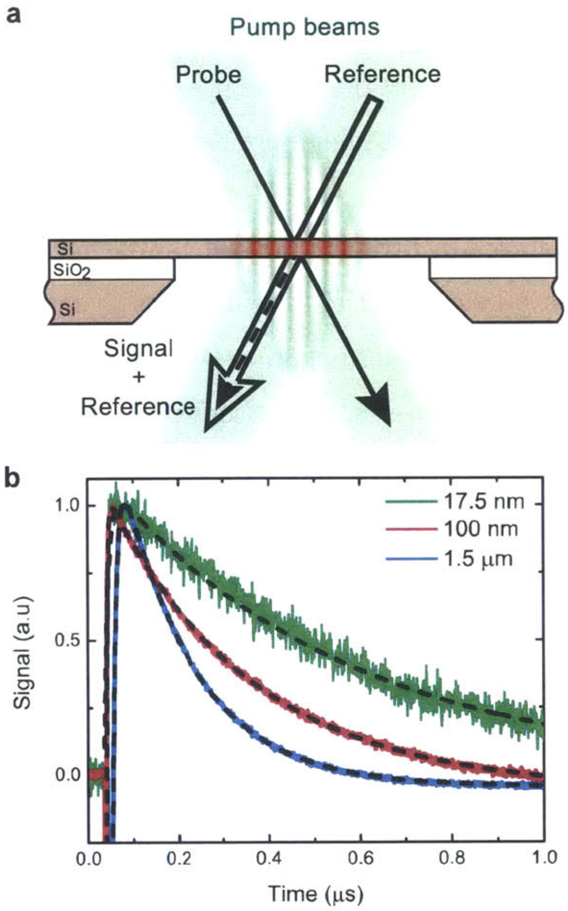

fig 3.1 Taken from [Cuffe] a) illustration of the TG geometry. Experimental details are presented in chapter 2. b) Representative time traces for silicon membranes of thickness 1515 nm (blue) 100 nm (red) and 17.5 nm (green). The slower decay for thinner membranes indicates a reduction in the thermal conductivity. The dashed line indicates a fit to the 1D heat diffusion equation

The optical penetration depth of silicon at wavelengths of 515 nm and 532 nm is just over 1 μm with the absorbance of each membrane determined by Fabry-Pérot effects, i.e. multiple reflection of the light inside the membrane [Chávez14]. Although the multiple reflections can significantly increase the absorption the maximum absorption was determined to be no greater than 0.65. As a result the membranes can be measured in the transmission TG geometry. In this geometry the light uniformly deposits heat throughout the depth of the membrane and the resulting thermal transport is one-dimensional in the plane of the film. A schematic illustration of the measurement and representative time traces for membranes with thickness 17.5 nm, 100 nm and 1518 nm are presented in fig 3.1. A visual comparison of the time traces in fib 3.1b shows an increase in the decay time for thinner membranes. This indicates a reduction in the thermal conductivity of the sample due to phonon scattering at the boundaries of the membrane. Phonon boundary scattering will be discussed in more detail in the next section.

The time traces are analyzed by fitting to an exponential decay (the solution to the 1D heat diffusion equation with a periodic heat source as described in chapter 3). The decay rate γ is related to the thermal diffusivity α by, $\gamma = \alpha q^2$, where q is the TG wavevector. As we noted in chapter 3, if the product of the TG wavevector and phonon MFP becomes larger than 1, or the MFP is long compared to the thermal length scale, the thermal transport becomes non-diffusive. In the non-diffusive regime the decay rate no longer scales as q^2 and the calculated diffusivity is reduced. To obtain an accurate thermal diffusivity, we perform measurements with long TG periods to assure purely diffusive transport. TG measurements were performed with periods ranging from 11 to 21 μm for all membranes. The extracted thermal diffusivities as a function of TG period are presented in fig 3.2a. Over the range of grating periods measured, there was no discernable change in the value of the diffusivity, indicating diffusive thermal transport. The conductivity for each membrane was calculated as $k = \alpha C$ where $C = 1.64 \times 10^6$ J m^{-3} K^{-1} is the volumetric heat capacity of silicon [Shanks]. The heat capacity was taken as constant for all membrane thicknesses because at room temperature the density of states shows no significant deviation from the bulk [Huang, Chávez12]. The thermal conductivity as a function of thickness is presented in fig 3.2b. The error bars indicate the uncertainties from the experiment and analysis. The largest source of error came from laser induced heating of the membrane. The magnitude of the error was estimated by repeating the measurements with twice the pump and probe powers. The pump was found to have no significant effect while double the probe power reduced the determined diffusivity by roughly 5%. The full error analysis can be found in [Cuffe14]

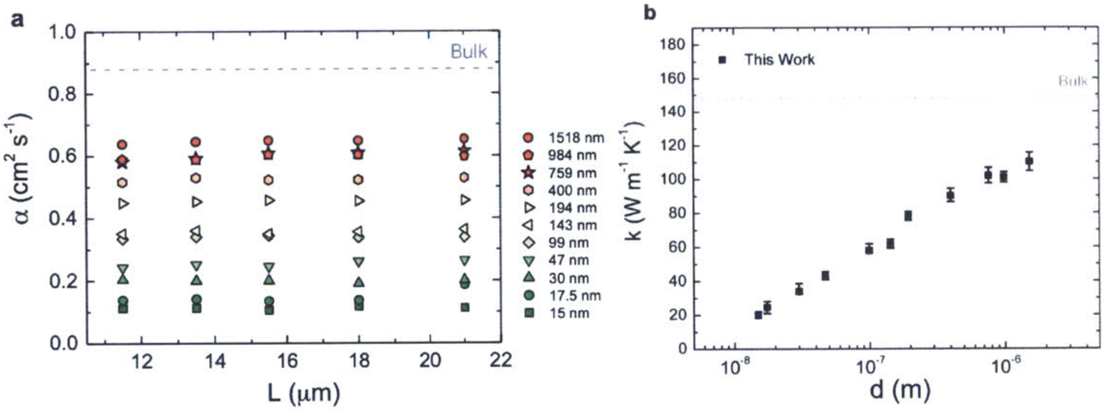

fig 4.2 a)Thermal diffusivities as a function of TG period extracted from exponential fits of time traces measured on silicon membranes with a range of thicknesses from 15 nm to 1518 nm. b) Thermal conductivity as a function of membrane thickness, determined by averaging over the values at each grating period.

For all membranes we notice a significant deviation of the thermal conductivity from the bulk. The 15 nm membrane showed a reduction to 15% of the bulk value and the 1518 nm membrane showed a reduction to 75% of the bulk value. The reduction of the thermal conductivity for large membranes is another clear indication of the large contribution of long MFP phonons to thermal transport in Si. The relationship between the phonon MFP and the membrane thickness is determined by the scattering of phonons at the surfaces of the membrane.

4.3 Phonon boundary scattering

The reduction of the in-plane conductivity in thin films was originally solved for electrical conductivity in metal films in the mid 1900's by [Fuchs] and [Sondheimer]. The derivation uses the Boltzmann transport equation and splits the phonon distribution into two components, which interact with the top and bottom surfaces of the film. When phonons interact with the surface they will be either specularly reflected or diffusely scattered. Specular reflection conserves the in plane component of the phonon wavevector and reverses the out of plane component, while diffuse scattering randomizes both components of the wavevector. A specularity parameter p is used to describe the fraction of phonons that have specular reflection from the surface, where $p = 0$ corresponds to completely diffuse scattering. In reality, the specularity parameter requires detailed knowledge of the surface roughness and the wavelength dependence of wave scattering off rough surfaces, both of which are complicated [Ogilvy]. Recently there has been progress on this front, with calculations of the specularity parameter under two approximations [Maznev14b]. When the roughness has a correlation length smaller than the wavelength of the phonon, $p \propto k^4$ where k is the phonon wavevector, the familiar dependence found in Rayleigh scattering. When the correlation length is long, known as the Kirchhoff approximation, $p \propto k^2$ which matches the form found in solid state physics textbooks [Ziman]. For silicon at room temperature most of the heat is carried by phonons with wavelength <6 nm [Esfarjani10]. In addition, recent photo-acoustic experiments at sub-THz frequency in silicon membranes indicate that diffuse boundary scattering for thermal phonons is a good approximation [Maznev15]. However, at low temperatures where relevant phonon wavelengths are much longer, a wavelength dependent specularity parameter is required [Ziman, Ogilvy].

For diffuse scattering at the interfaces the in-plane thermal conductivity of the membrane is [Chen05],

$$k_{mem} = \frac{1}{3}\int_{0}^{\omega_{max}} C_\omega v S\left(\frac{\Lambda_{bulk}}{d}\right)\Lambda_{bulk} d\omega \tag{4.1}$$

where ω is the phonon frequency, C_ω is the volumetric heat capacity, v is the group velocity, Λ_{bulk} is the phonon MFP in the bulk material, d is the membrane thickness and $S(\Lambda_{bulk}/d)$ is the heat flux suppression function [Fuchs, Sondheimer]. The suppression function describes how much the contribution of a given phonon mode with MFP Λ_{bulk} is reduced by diffuse boundary scattering in a membrane with thickness d and has the following form,

$$S\left(\frac{\Lambda_{bulk}}{d}\right) = 1 - \frac{3}{8}\frac{\Lambda_{bulk}}{d} + \frac{3}{2}\frac{\Lambda_{bulk}}{d}\int_{1}^{\infty}\left(\frac{1}{t^3} - \frac{1}{t^5}\right)\exp\left(-\frac{d}{\Lambda_{bulk}}t\right) \tag{4.2}$$

where t is a parameter describing the propagation direction of the phonons. The full derivation of the in plane conductivity for phonons is presented elsewhere [Cuffe14]. The suppression function with diffuse boundary scattering is presented in fig 4.3.

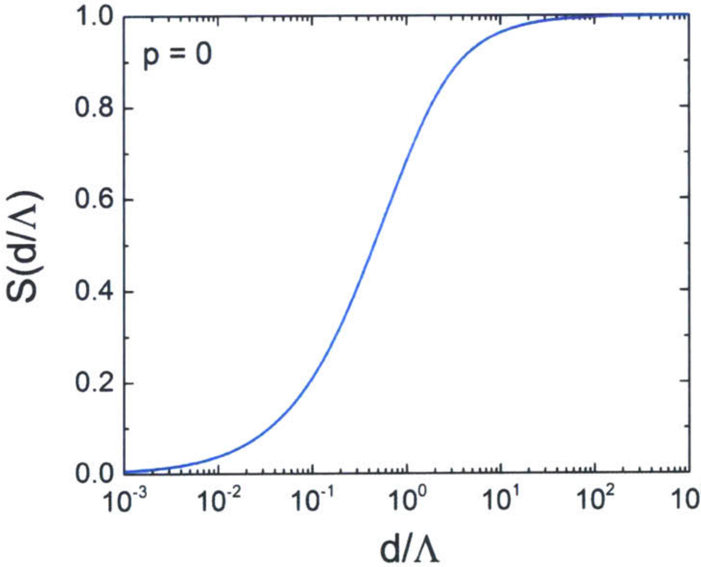

fig 4.3 Fuchs-Sondheimer suppression function plotted as a function of membrane thickness *d* over the phonon MFP Λ for diffuse scattering at the surfaces.

From figure 4.3 we see the broad range of phonon MFPs that contribute to the in-plane transport. This is in contrast to the reduction of the MFP in a thin rod where

Casimir predicted that the MFP is limited by the diameter of the rod [Casimir]. In a membrane, the extra dimensionality results in a significant contribution of phonons with MFP much longer than the membrane thickness even with diffuse boundary scattering.

4.4 Comparing experiment to theory

To aid in performing the calculation in eq 4.1 we can perform a change of variables to express the thermal conductivity in the membrane as a function of MFP.

$$k_{mem} = \int_0^\infty K_{\Lambda_{bulk}} S\left(\frac{\Lambda_{bulk}}{d}\right) d\Lambda_{bulk} \tag{4.3}$$

where, $K_{\Lambda_{bulk}} = -\sum_S \frac{1}{3} Cv\, \Lambda_{bulk} \frac{d\omega}{d\Lambda_{bulk}}$ is the differential MFP distribution as shown in fig 3.2. Using the calculations from [Esfarjani10] we calculate the thermal conductivity of the silicon membrane as a function of the membrane thickness. The experimental data and theoretical curve are presented in fig 4.4.

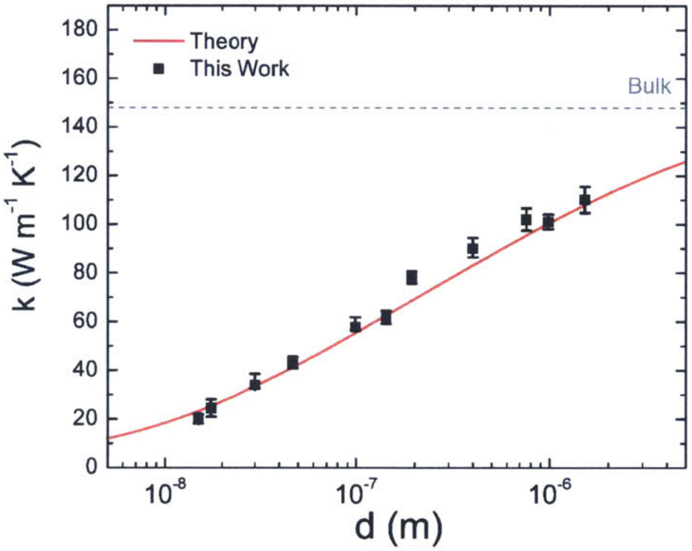

Fig 4.4 Thermal conductivity of Si membranes as a function of thickness d. The theoretical curve was calculated from eq. 4.3 using MFP distributions obtained from [Esfarjani10].

We see good agreement between the theoretical predictions and our experimental data, demonstrating the ability of first principles calculations to accurately calculate thermal conductivity without any fitting parameters.

In fig 4.5 we present our experimental results along with measurements of thermal conductivity in thin silicon films from the literature [Chávez14, Hao, Aubain10, Aubain11, Asheghi, Ju, Liu]. The previous measurements come from both supported and unsupported films but the large error bars have made it difficult to compare these results to the theory. TG measurements on Si membranes demonstrate the ability to accurately measure the thermal conductivity over a wide range of thicknesses with one technique.

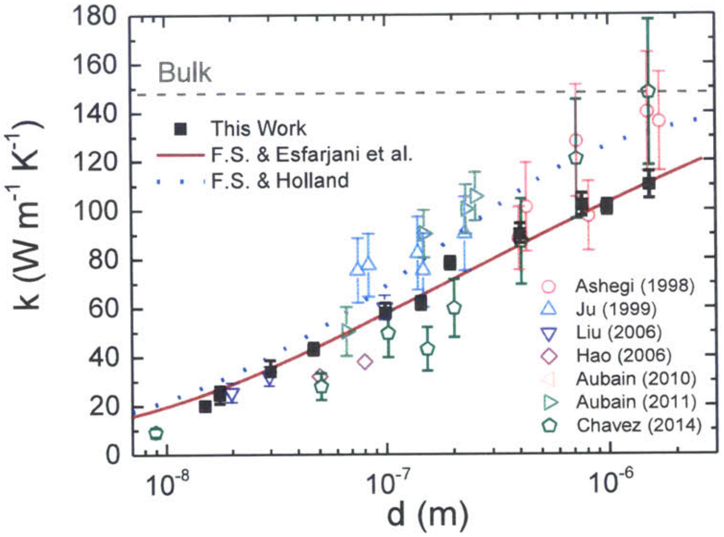

fig 4.5 Thermal conductivity of Silicon membranes as function of thickness comparing the TG measurements with a number of other measurements from the literature. Theoretical curve calculated using eq 4.3 based on the first principles MFP distribution from [Esfarjani] (red) and the MFP distribution from [Holland].

4.5 Reconstructing the MFP distribution

In the previous section we demonstrated that the thermal conductivity of thin films can be determined using first principles calculations of the phonon MFP distribution and the Fuchs-Sondheimer suppression function. We could also look at the inverse problem, determining the MFP distribution from the measured thermal conductivity and the suppression function. We can write eq 4.3 in terms of the accumulative thermal conductivity(presented in red in fig 3.2) and normalizing to the bulk value for thermal conductivity we obtain the expression in eq 4.4.

$$\frac{k_{mem}}{k_{bulk}} = \int_{0}^{\infty} k_{acc}(\Lambda_{bulk}) \frac{dS\left(\frac{\Lambda_{bulk}}{d}\right)}{d\Lambda_{bulk}} d\Lambda_{bulk}, \qquad (4.4)$$

Here $k_{acc}(\Lambda_c) = \int_0^{\Lambda_c} K_{\Lambda_{bulk}} d\Lambda_{bulk}$, is the cumulative thermal conductivity which describes how much phonons with MFP up to Λ_c contribute to the thermal conductivity. Inverting this expression to obtain k_{acc} is an ill-posed problem, but Minnich *et. al.* developed a way to extract k_{acc} by imposing constraints [Minnich14]. They used an algorithm following a mathematical procedure called convex optimization to find the smoothest function that monotonically increases from 0 to 1 and still satisfies eq 4.4. The reconstruction result is shown in fig 4.6 showing very good agreement with first principles calculations from [Esfarjani10] and MD simulations from [Henry]. Our extracted cumulative thermal conductivity is also compared with the Holland model [Holland].

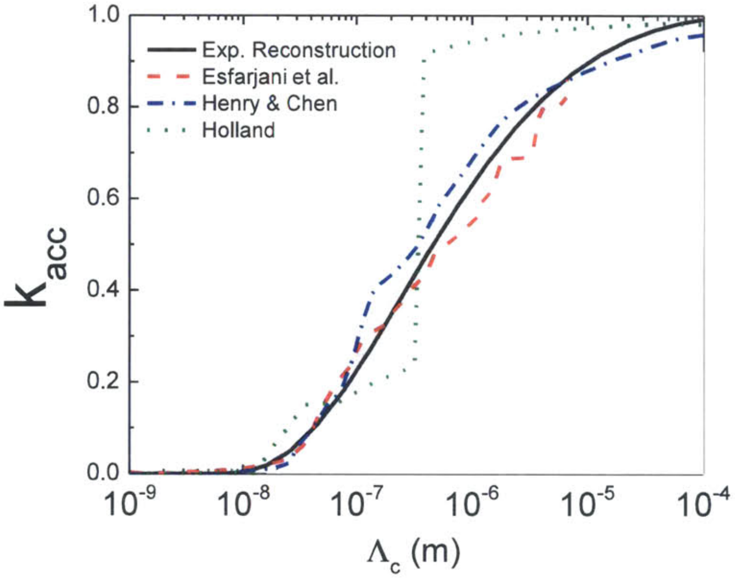

fig 4.6 Reconstructed cumulative thermal conductivity or the phonon MFP distribution for silicon presented with recent calculations and the Holland model. The shaded grey area indicates the uncertainty in the reconstruction using the error bars in the experimental measurements.

The reconstruction result presented here is the first experimental determination of the bulk MFP distribution of any material. This is enabled by knowledge of the suppression function for the well-defined experimental geometry of in plane transport in thin slabs. This method has the potential to be extended to many other materials as the suppression function applies only to the sample geometry. This provides the ability to determine the MFP distribution in materials where accurate calculations are not possible.

4.6 Low temperature measurements in a 200 nm Si membrane

The reconstruction technique offers the possibility to experimentally determine the phonon MFP distribution. A natural extension is to use this technique to explore the temperature dependence of the MFP distribution. This is especially useful because calculating the MFP distribution at low temperatures is difficult because it requires a large calculation cell to accurately account for the large contribution from low frequency, long MFP phonons. As a result, low temperature calculations are unreliable [Esfarjani10].

Here we present temperature dependent measurements of thermal diffusivity in a 200 nm Si membrane using the TG technique. The experimental technique is presented in chapter 2 and the temperature was controlled using a Janis ST-100 cryostat. Liquid nitrogen was used to cool the samples and a Lakeshore 301 temperature controller was used to stabilize the temperature. The thermal diffusivity as a function of TG period at a number of different temperatures is presented in fig 4.7.

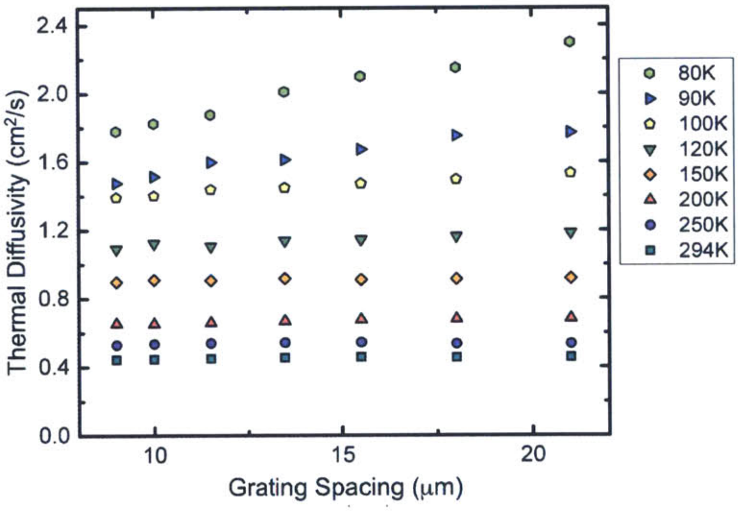

fig 4.7 Thermal diffusivity of a 200 nm membrane as a function of TG period for temperatures ranging from 80K to 294K.

At temperatures close to room temperature, the thermal diffusivity is independent of the grating period indicative of diffusive thermal transport. This is consistent with the reduction of the phonon MFP in the membrane due to diffuse scattering at the boundaries. At low temperatures the thermal diffusivity is reduced for short grating spacings. This indicates that at low temperatures long MFP phonons are contributing to thermal transport in the membrane. The contribution of long MFP phonons (>10 μm) is surprising since a significant reduction in the MFP is expected due to diffuse scattering at the membrane boundaries. We have previously mentioned that the specularity of the membrane boundaries will be wavelength dependent. It is likely that at low temperatures, where long wavelength phonons contribute significantly to thermal transport, a completely diffuse scattering picture is inaccurate.

We can calculate the thermal conductivity with first principles MFP distributions using similar approaches to those presented previously. But for our low temperature measurements we need to account for boundary scattering and the heat flux suppression due to the grating periodicity. The thermal conductivity in a membrane with thickness d as a function of grating wavevector q is presented in eq 4.5.

$$k_{mem}(q) = \int_0^\infty K_{\Lambda_{bulk}} S\left(\frac{\Lambda_{bulk}}{d}\right) A\left(qS\left(\frac{\Lambda_{bulk}}{d}\right)\Lambda_{bulk}\right) d\Lambda_{bulk} \tag{4.5}$$

Here S is the Fuchs-Sondheimer suppression function shown in eq 4.2, and A is the suppression function for the grating period shown in eq 3.9. We make a crude approximation in which the phonon MFPs that contribute to the grating decay are first modified by the membrane which is why the factor $S\left(\frac{\Lambda_{bulk}}{d}\right)\Lambda_{bulk}$ appears inside the expression for A. We use temperature dependent MFP distributions calculated from first principles to calculate the thermal conductivity in the membrane, courtesy of Keivan Esfarjani and Austin Minnich. The thermal conductivity is converted to thermal diffusivity by $\alpha = k/\rho c_p$ so that we can easily compare with our experimental measurement. The temperature dependent volumetric heat capacities were obtained from the literature [Flubacher]. The theoretical results for a specularity parameter of p=0, along with the experimental data, are presented in figure 4.8. Our results indicate that the diffuse boundary scattering approximation does not work at low temperatures where long MFP phonons no longer scatter diffusely at the membrane boundaries. In addition, at 80K the measured diffusivity does not level out. In order to accurately determine the thermal conductivity at low temperature using the TG technique, a much longer grating spacing is required. This is a surprising result considering the largest grating period is a hundred times larger than the thickness of the membrane.

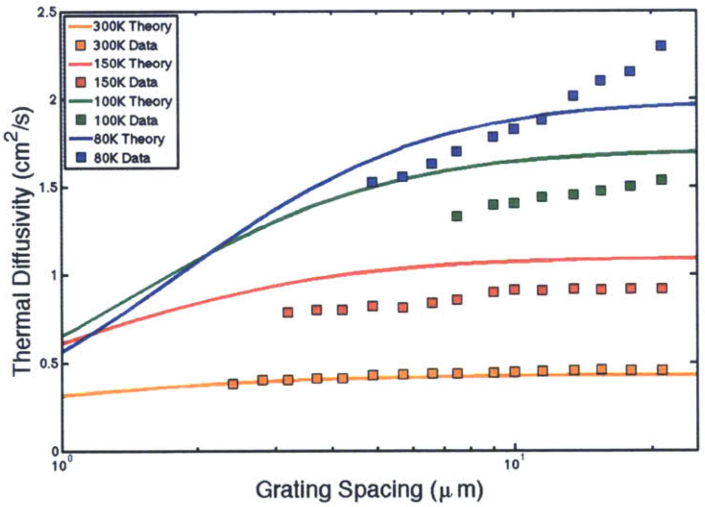

fig 4.8 Thermal diffusivity of a 200 nm Si membrane as a function of grating period. Experimental points are measured with the TG technique and the theory curves are results from first principles calculations of the MFP distribution at low temperatures by Keivan Esfarjani and Austin Minnich.

4.7 Summary

In this chapter we presented thermal conductivity measurements of silicon membranes for a wide range of thicknesses. The high accuracy of the measurements and wide range provide a significant improvement over previous measurements from the literature. Our results show good agreement with first principles calculations, providing more evidence of the broad nature of the MFP distribution in silicon. Using the known suppression function and the experimental measurement results, we applied convex optimization to reconstruct the MFP distribution. The experimentally determined MFP distribution shows good agreement with theoretical models. Our approach opens up possibilities to determine the MFP distribution in materials where it cannot be easily calculated. Finally, we present preliminary measurements of the thermal diffusivity in a 200 nm membrane at low temperatures. The results indicate that the diffuse scattering approximation doesn't work well at low temperatures and a wavelength dependent specularity parameter is needed.

Chapter 5

Surface Acoustic Waves in Granular Media

5.1 Introduction

Granular media are assemblies of discrete solid particles. Sand, perhaps the most ubiquitous granular material, is composed of small particles of rocks. Granular media are host to a number of interesting linear and non-linear phenomena [Hinrichsen, Nesterenko, Theocharis]. Wave behavior in granular media is of particular interest because the interaction between the discrete particles is highly non-linear[Hertz]. Granular media can exhibit the properties of gasses, liquids and solids, but can also enter jammed states, where particles get trapped out of equilibrium [Hinrichsen]. Ordered granular media, sometimes called granular crystals, are analogous to a solid crystal but instead of atoms locked in a lattice structure through microscopic interactions, the granular particles form an ordered lattice where contact between particles is described by the Hertzian contact model. Typical studies on granular crystals have been performed with relatively large particles, 1 mm – 10 mm [Hinrichsen, Nesterenko, Theocharis], but there have been limited studies of granular crystals with ~1 um particles. Particles with dimensions on the single micron scale are particularly interesting due to the increased role of adhesion, or Van der Waals forces, between the particles. This chapter will begin with an introduction to contact mechanics and discuss the role of adhesion in particle interactions. Then, we will cover surface acoustic waves and how we experimentally generate and detect them. Finally, we will use interaction between SAWs and a 2D array of particles to study the behavior of microscale contacts.

5.2 Contact mechanics and adhesion

In the late 1800's Heinrich Hertz studied the interaction between two elastic bodies [Hertz]. Hertz discovered that the stiffness of the contact depends on the applied force between them. Consider for example a sphere in contact with an elastic half space. If a force is applied to the sphere, both the sphere and the substrate will deform. The applied force F can be related to the displacement as,

$$F = KR^{1/2}\alpha^{3/2} \tag{5.1}$$

where $K = \left[3/4\left(((1-\nu_s^2)/E_s) + ((1-\nu_1^2)/E_1)\right)\right]^{-1}$ is the effective modulus with E_s and ν_s the elastic modulus and Poisson's ratio for the spheres and E_1 and ν_1 the elastic modulus and Poisson's ratio for the substrate, R the radius of the sphere, and α the displacement from the equilibrium position. The area of the contact depends on the radius of the sphere and the applied force as $a = \sqrt{Rd}$. A schematic illustration of the contact and the force vs. displacement curve are shown in fig 5.1

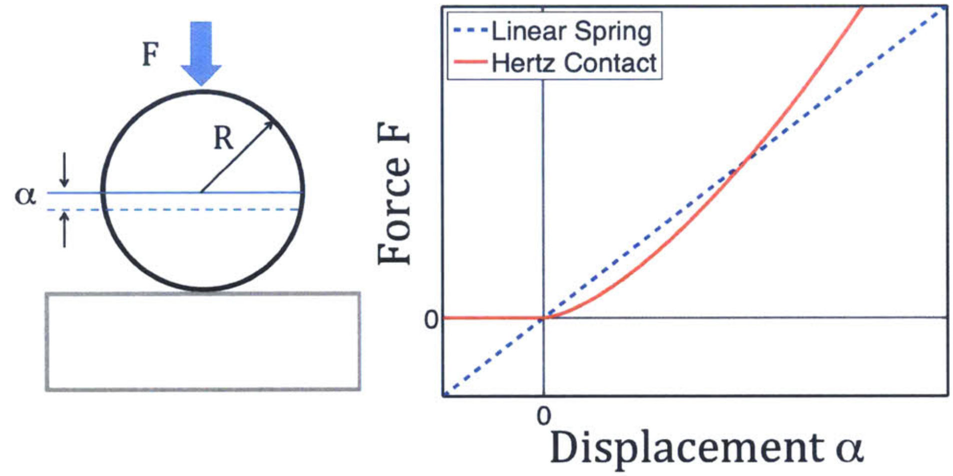

Fig 5.1 (left) Schematic illustration of Hertzian contact between an elastic sphere and an elastic half space. (right) Force-displacement curve for a Hertzian contact compared to a linear spring.

The Hertz model works well for large particles (>1mm), but as the particle dimension decreases, adhesive forces become significant and can't be neglected. Adhesion forces scale with the radius of the particle, whereas gravitational forces scale as the radius cubed [Israelachvili]. For example, the adhesion force between a 1 μm particle and a substrate is over a million times larger than the force of gravity. There are a number of models that have been used to describe the added adhesive interaction [Bhushan]. We will discuss the DMT model, detailed by Muller, Derjaguin and Toporov in their 1983 paper [DMT, Pashley]. The DMT model assumes that the nature of the contact between the sphere and substrate remains the same as in the Hertz model but additional attraction between the sphere and the substrate (adhesion) occurs outside the contact area. In the DMT model the force can be related to the displacement as,

$$F_{DMT} = KR^{1/2}\alpha^{3/2} - 2\pi wR \tag{5.2}$$

where the additional term on the right accounts for the adhesive interaction, and w is the work of adhesion. A schematic illustration of the DMT model along with the force vs. displacement curve are presented in fig x. At zero applied force there is a finite slope in the force vs. displacement curve rather than no slope, as in the Hertz model. The finite slope at zero force gives a stiffness to the contact, which now behaves as a spring. It is also interesting to see the curve drops below zero force stemming from the attractive nature of the adhesion force. The force at which the sphere detaches from the surface is called the pull-off force. The pull-off force is the central interaction in many scanning probe measurements such as AFM and has been widely studied [Israelachvili].

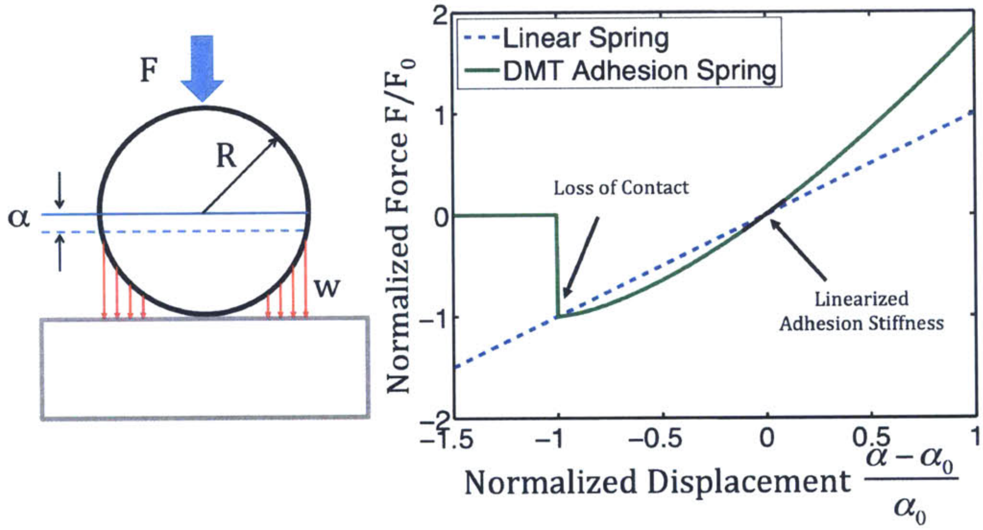

fig. 5.2 (left) Schematic illustration of a sphere in contact with a substrate with added adhesion outside of the contact area (right) Force vs. Displacement curve for a sphere adhered to a substrate under the DMT model compared to a linear spring.

Within the picture of the contact behaving as a mass on a spring we can define the resonance frequency of the oscillation as

$$\omega_{0,DMT} = 2\pi f_{0,DMT} = \sqrt{\frac{K_{2,DMT}}{m}} \tag{5.3}$$

where $K_{2,\mathrm{DMT}}$ is the linearized stiffness at equilibrium displacement given by $K_{2,DMT} = (3/2)(2\pi wR^2K^2)^{1/3}$, and m is the mass of the sphere. This assumption is only valid when the frequency of the sphere's motion is lower than the vibrational modes of the sphere and the sphere behaves as a rigid body. Given an impulse force normal to the sphere, the sphere will oscillate at this frequency, and the motion will remain normal to the surface. There are likely other resonances from rocking motion or even shear motion, but we will focus on the normal motion. The vertical vibrational motion, called the axial contact resonance, is the target of the experiments that we present in this thesis. To probe the axial contact resonance of micron sized spheres we will use surface acoustic waves (SAWs) generated by the TG technique.

5.3 SAW generation and detection

Surface acoustic waves are waves that propagate along the surface of a material. A common type of acoustic wave, the Rayleigh wave, has a combination of longitudinal and shear motion, resulting in displacement parallel to and perpendicular to the surface respectively. The vertical motion generated by the Rayleigh wave provides the driving force to excite the axial motion of a sphere on the surface of the material. The TG technique is well suited for generation and detection of surface acoustic waves and has the ability to generate SAWs with a wide range of frequencies. When the two short excitation pulses are crossed at the surface of a highly absorbing material, the stress caused by fast thermal expansion generates counter-propagating surface acoustic waves with wavelength determined by the period of the interference profile L given in eq 2.1. The surface ripple caused by the SAW diffracts an incident probe beam, which is combined with a reference beam for heterodyne detection as is described in Chapter 2. All the experiments we performed on microspheres used a glass substrate coated with an aluminum film of thickness 100-200nm. We typically generate SAWs by crossing the beams on the aluminum film from the backside, through the transparent glass substrate. A typical time trace taken at 32.5 μm and its Fourier transform can be seen in fig 5.3. The oscillations in the time trace correspond to the SAW and the offset from the baseline and decay come from the spatially periodic heating of the aluminum film and subsequent thermal diffusion. The Fourier transform of the time trace returns the frequency components of the oscillatory signal. The low frequency peak in the Fourier transform corresponds to the Rayleigh wave, with frequency equal to the Rayleigh velocity divided by the TG period. The peak at higher frequency comes from a surface-skimming longitudinal wave, which is particularly strong because we probe through the depth of the substrate. The frequency of the longitudinal wave matches the expected frequency calculated using the longitudinal speed of sound in the substrate and the TG period.

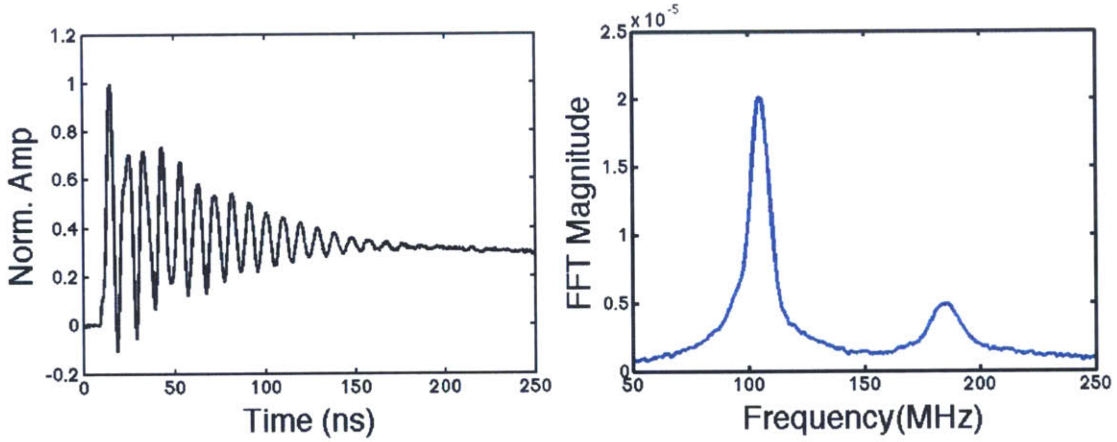

fig 5.3 (left) Heterodyne signal obtained from SAWs generated on a Al film on a glass substrate with a TG period of 32.5 μm (right) Fourier transform of the SAW signal showing the Rayleigh peak at 105 MHz and surface-skimming longitudinal wave at 185 MHz.

5.4 Wave behavior in a monolayer of microspheres

5.4.1 Experiment

To study the axial contact resonance of micron sized spheres we will investigate SAW propagation in a 2D array of spheres. The full experimental details, as well as theory, are presented in [Boechler], but we will introduce the essential components here. The hexagonally packed monolayer of 1.08 μm spheres is formed using a "wedge-shaped cell" in a convective self-assembly technique [Sun, Canalejas]. The monolayer was deposited on a 1.5 mm thick fused silica substrate coated with a 0.2 μm aluminum film. Surface acoustic waves were generated with the TG technique by focusing on the aluminum film through the substrate. Images of the monolayer as well as a schematic diagram of the TG geometry are presented in Fig 5.4. To measure the dispersion of the system, TG time traces were taken as a function of SAW wavevector from 0.12 – 0.83 μm^{-1} (50 μm – 7.5 μm wavelength). A representative data set is shown in fig 5.5 at a wavevector of 0.46 μm^{-1}. The time dependence of the diffracted TG signal is shown in (a) and (b) for SAW generation on the bare substrate and on the monolayer of spheres respectively. It is immediately obvious that there is a significant change to the signal when the SAW is generated on the monolayer region due to the coupling between the axial contact vibration and the surface motion. A Fourier transform of the time data returns the frequency components in the on-spheres and off-spheres data, and is presented in fig 5.5 (c) and (d) with logarithmic and linear representation respectively. Looking at fig 5.5 (c) we can see the spectra of the SAW on the substrate in black, with two peaks corresponding to the Rayleigh wave (low frequency) and longitudinal wave (high frequency). The SAW in the monolayer is plotted in red, showing the appearance of an additional peak. The longitudinal peak is unchanged while the Rayleigh wave peak has been split into two peaks. The full dispersion of the system is plotted in Fig 5.6. The black markers correspond to data taken on the bare substrate with the three black lines corresponding to the wave speeds in fused silica, c_L = 5968 m/s for longitudinal, c_T = 3764 m/s for transverse, and c_R = 3409 m/s for the Rayleigh velocity, calculated using the numerical solution to the Rayleigh equation [Ewing]. We also accounted for the change in Rayleigh velocity due to the aluminum layer but found that the deviation was small, around 1% lower, and so was neglected for this analysis [Boechler]. The red markers correspond to data taken on the monolayer region, which display "avoided crossing" behavior between the Rayleigh wave and the axial contact resonance of the microspheres. The lower branch starts out resembling the SAW but approaches a horizontal asymptote at the resonance frequency. The upper branch resembles the SAW at high wavevectors and approaches a horizontal asymptote at low wavevectors, but it disappears after crossing the line corresponding to the transverse velocity of the substrate because such modes are classified as leaky waves that radiate as shear waves into the substrate [Every, Mason]. The solid red lines correspond to our theoretical model detailed in the next section.

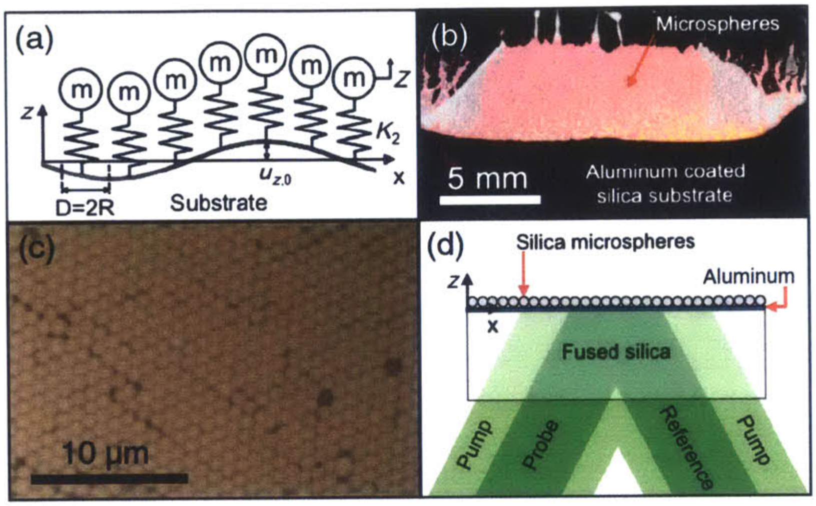
(a)
m
z
z
K₂
u_{z,0}
x
D=2R
Substrate
(b)
Microspheres
5 mm
Aluminum coated
silica substrate
(c)
10 µm
(d)
Silica microspheres
Aluminum
z
x
Fused silica
Pump
Probe
Reference
Pump

fig 5.4 Taken from [Boechler] (a) SAW interacting with the axial contact vibration of spheres. Notations consistent with theory in the text. (b) Photo of sample. (c)Microscope image of monolayer showing hexagonal close packing. (d) Schematic diagram of TG geometry.

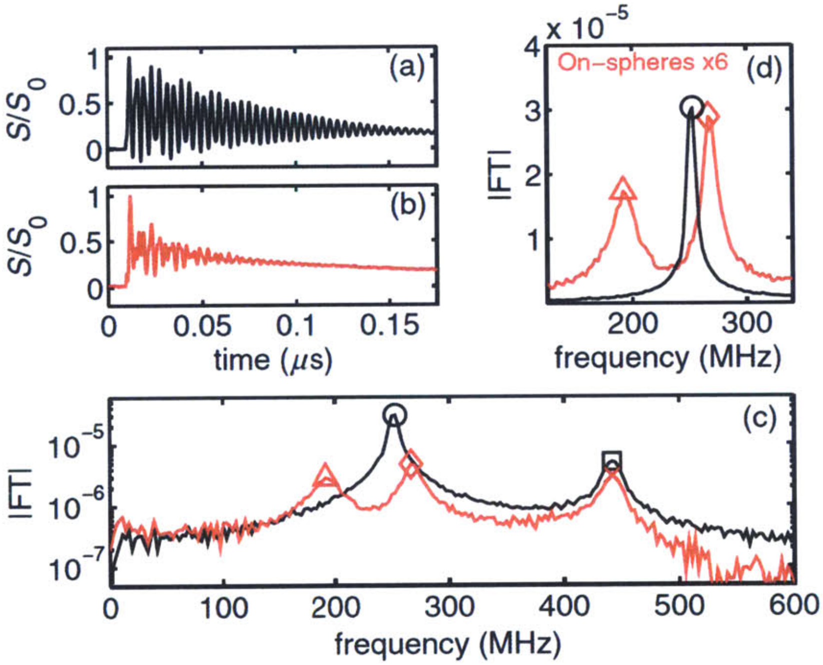

Fig 5.5 Taken from [Boechler] Normalized time traces taken on the bare substrate (a) and on a monolayer of 1.08 μm spheres (b) with a wavevector of 0.46 μm^{-1}. Fourier transform spectra comparing on (red) and off sphere (black) plotted with a log scale (c) and linear scale (d). The marks indicate the chosen peak positions presented for the full wavevector range in Fig 5.6.

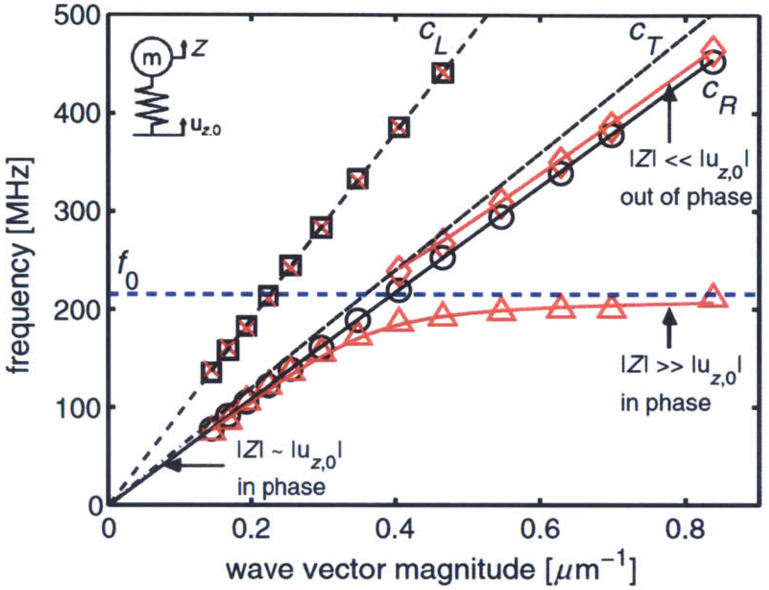

fig 5.6 Taken from [Boechler] Dispersion relations for substrate (black) and monolayer of spheres (red). The points indicate peak positions taken from the Fourier transforms at each wavevector.

5.4.2 Theory

The model for SAW propagation in a monolayer of microspheres is adapted from [Kosevich, Baghai-Wadji, Garova] and will follow the derivation in [Boechler] but here we present a Green's function approach to arrive at an identical result. A schematic illustration of the model is shown in fig 5.4(a), where we treat the substrate as an elastic half-space, and the surface of the substrate is covered by an array of oscillators. The oscillators represent the contacts between the microspheres and the substrate in the DMT model. The contact is treated as a linear spring, with stiffness K_2, connecting a microsphere with mass m to the substrate. The motion of the oscillators is described by the equation for a harmonic oscillator as,

$$m\ddot{Z} + K_2(Z - u_{z,0}) = 0 \tag{5.4}$$

where Z is the displacement of the oscillator relative to the surface, and $u_{z,0}$ is the displacement of the substrate surface induced by the SAW. The spheres apply a force normal to the surface of the substrate, yielding the following boundary conditions at $z = 0$:

$$\sigma_{zz} = \frac{K_2(Z - u_{z,0})}{A} \qquad \sigma_{xz} = 0 \tag{5.5}$$

where σ_{zz} and σ_{xz} are components of the elastic stress tensor and $A = \left(\sqrt{3}D^2/2\right)$ is the area of the unit cell for the hexagonally packed monolayer. Since the acoustic wavelength used in the experiment is much larger than the sphere diameter, we use an effective medium approximation to obtain the boundary conditions. This approximation allows us to treat the normal stress of the microsphere contact spring as the applied force divided by the contact area. Assuming a traveling wave solution for the surface oscillators, $Z = Z_0 \exp(i\omega t - ikx)$, and substituting into equation 5.4 gives the following result.

$$Z = \left(\frac{\omega_0^2 u_{z,0}}{\omega_0^2 - \omega^2}\right) \tag{5.6}$$

where ω_0 is the resonance frequency of the axial contact vibration obtained from the DMT model and shown in eq 5.3. Substituting the resulting Z into the boundary conditions (eq 5.5) results in new stress boundary conditions at z =0,

$$\sigma_{zz} = \frac{K_2}{A}\left(\frac{\omega^2 u_{z,0}}{\omega_0^2 - \omega^2}\right) \qquad \sigma_{xz} = 0 \tag{5.7}$$

To determine the dispersion relation of the system we can use a Green's function approach. In the Fourier domain, the Green's function, relates the surface displacement and the stress as,

$$\tilde{u}_{z,0} = \tilde{G}(\omega, k)\tilde{\sigma}_{zz} \tag{5.8}$$

where $\tilde{G}(\omega, k)$ is the surface Green's function for an elastic half space. The surface Green's function for an isotropic half space is given by [Maradudin, Eguiluz],

$$\tilde{G}(\omega, k) = \frac{1}{\rho c_T^4} \frac{\omega^2 k \left(1 - \frac{\omega^2}{k^2 c_L^2}\right)^{1/2}}{R(k)} \tag{5.9}$$

where $\rho = 2.2$ g/cm^3, is the density of the fused silica substrate and *R(k)* is the Rayleigh determinant,

$$R(k) = 4k^4\left(1 - \frac{\omega^2}{k^2 c_T^2}\right)^{1/2}\left(1 - \frac{\omega^2}{k^2 c_L^2}\right)^{1/2} - k^4\left(2 - \frac{\omega^2}{k^2 c_T^2}\right)^2 \tag{5.10}$$

By substituting eq 5.8 into eq 5.7 and using the Green's function and Rayleigh determinant, we can recover the dispersion relation as,

$$\left(\frac{\omega^2}{\omega_0^2}-1\right)\left[\left(2-\frac{\omega^2}{k^2c_T^2}\right)^2-4\left(1-\frac{\omega^2}{k^2c_T^2}\right)^{1/2}\left(1-\frac{\omega^2}{k^2c_L^2}\right)^{1/2}\right] = \frac{m}{A\rho}\frac{\omega^4}{c_T^4k^3}\left(1-\frac{\omega^2}{k^2c_L^2}\right)^{1/2} \tag{5.11}$$

The numerical solution of the dispersion equation is plotted in red in fig 5.6. On the left hand side of eq 5.11, the expression in brackets describes the Rayleigh wave and the expression in parentheses is the resonance of the surface oscillators. The right hand side of the equation describes the coupling between the Rayleigh wave and the surface oscillators. The magnitude of the coupling will depend on m, ρ and A, while the resonance frequency, i.e. the position of the avoided crossing, will depend on m and K_2. Using a least squares minimization algorithm, we fit the numerical dispersion relation to the experimental data, with the resonance frequency as the only free parameter. From the fit to the experimental data in fig 5.6 we recover a resonance frequency of $f_0 = \omega_0/2\pi = 215$ MHz. The mass of the microsphere was calculated using a density $\rho_s = 2.0$ g/cm^3, which results in a contact stiffness $K_2 = 2.4$ kN/m.

The real solutions of the dispersion relation have a phase velocity ω/k, less than the velocity of the shear wave c_T. All other solutions result in imaginary roots, leading to the upper branch disappearing at $\omega = c_T k$, matching the experimental results. Modes with imaginary solutions are called leaky modes, which radiate into the substrate as shear waves and don't appear in the signal.

Using eq 5.6 we can estimate the relative displacement of the spheres Z and the substrate $u_{z,0}$. The displacement of the substrate for this experiment is 8.3 pm, which is calculated based on the pulse energy and the thermoelastic properties of the aluminum film and the substrate [Boechler]. For the lower branch, we see that the surface displacement is roughly equal to the displacement of the oscillators. As the lower branch flattens out and approaches the resonance frequency, the displacement of the spheres becomes much larger than the surface displacement.

This is confirmed by comparing measurements on the backside to those performed on the front, or with the lasers directly on the spheres. The front side measurement is more sensitive to the displacement of the spheres as the light interacts with the spheres directly. A comparison of the front side and backside measurements is shown in Fig 5.7, clearly demonstrating the larger amplitude of the peak corresponding to the lower branch in the front side measurement. Above the resonance frequency, on the upper branch, the displacement of the spheres is much smaller than the displacement of the surface. Although the displacement of the spheres is larger than the displacement of the surface on the flat part of the lower branch, the displacement is still much smaller than the equilibrium displacement $\alpha_0 = \left(2\pi R^{1/2}/K\right)^{2/3} = 0.44$ nm calculated from the DMT model [Boechler].

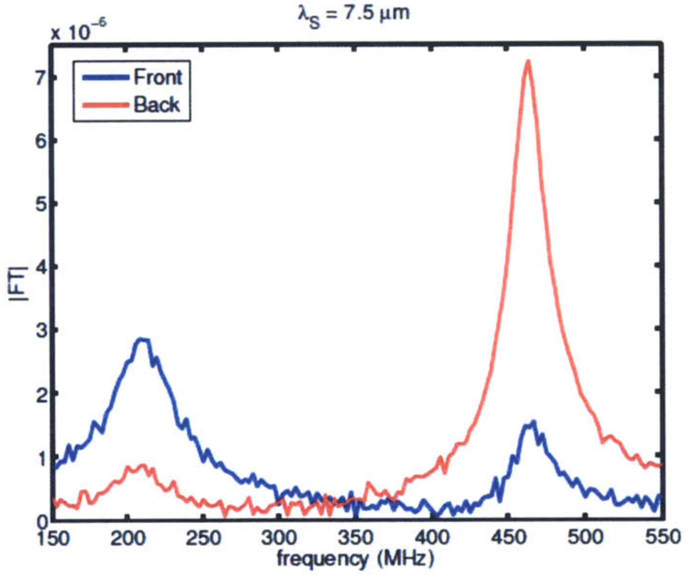

fig 5.7 Taken from the supplementary information of [Boechler]. Fourier spectra of TG measurements with a period of 7.5 μm taken of the front (blue) and back (red) of the microsphere monolayer.

The resonance frequency of the axial vibration of the spheres can be estimated using the DMT model by determining the stiffness of the contact given by $K_{2,DMT} = (3/2)(2\pi w R^2 K^2)^{1/3}$. The work of adhesion, between the oxidized aluminum surface and the silica spheres is w = 0.094 J^2/m [Lide], giving K_2 = 1.1 kN/m and a resonance frequency of f_0 = 140 MHz. There are other motions of the spheres, such as a lateral motion with calculated frequency f_l = 129 MHz, and a rocking motion with calculated frequency f_r = 9.1 MHz, but no signatures of these motions were seen in our signals, which might be a result of the close packing of the spheres [Boechler, Vittorias, Murthy Peri]. The relatively large discrepancy between our data and the DMT model could be explained by a larger work of adhesion than is presented in the literature, or uncertainties in the contact model. Indeed there has been a great deal of trouble in using the DMT model to predict the behavior of nanoscale contacts measured with atomic force microscopy (AFM) [Israelachvili]. AFM measures the pull-off force, which doesn't provide all the necessary information to accurately test adhesion models. In our measurement we obtain the contact stiffness directly from the resonance frequency, thus providing a more straightforward comparison to adhesion models in the limit of small displacements. A natural extension of this work is to use SAWs with larger amplitude to probe the anharmonic response of the axial contact providing additional information about adhesion. It is worth noting that the calculated resonance frequency from another common contact model, the JKR model shows only a 5% difference from that of the DMT model, suggesting that there may be other factors that affect the resonance frequency of the microsphere contact [JKR, Boechler].

5.5 Summary

In this chapter we introduced the Hertz model for contact between a sphere and an elastic half-space. When the sphere becomes small, attractive forces (adhesion) between the sphere and substrate become significant and cause a deformation of the sphere and substrate around the contact area. To account for adhesion we discussed the DMT model, where the contact area remains the same as in the Hertz model but the attractive forces act outside the contact area. To test adhesion models, we investigated the interaction between SAWs and a monolayer of micron sized spheres. We observed a classic avoided crossing in the dispersion relation of the system at the resonance frequency of the axial contact. This system provides a natural platform to study the linear and non-linear behavior of microscale contacts.

Chapter 6

Mechanical Properties of Microsphere Structures

6.1 Introduction

A monolayer of microspheres provides an interesting platform to investigate the wide range of linear and non-linear dynamics present in microscale contacts. Even though adhesive forces are the dominant interaction between small particles, there is no definitive model to describe the interaction [Bhushan]. In the previous chapter we determined the dispersion properties and contact resonance frequency and compared the results to the DMT model showing good agreement (within a factor of two). Our results suggest a wide range of further experiments including characterization of environmental (e.g. humidity) and structural (e.g. particle size and surface roughness) effects, development of SAW control possibilities such as waveguiding and filtering, and exploration of nonlinear and linear responses. By exploring the wide range of environmental and structural factors that influence the axial contact resonance frequency we can gain insight into the fundamental nature of the adhesive interaction. In addition, demonstrating SAW control in the linear and nonlinear regimes will indicate the usefulness of a monolayer of microspheres for applications in SAW devices. This final chapter presents preliminary results showing progress in these directions and indicates the steps needed for more controlled experiments and a more detailed analysis.

6.2 Variability of adhesion conditions

6.2.1 Sample-to-sample variations

In our experiments the characterization of adhesion in the microsphere monolayer is based on the measurement of the resonance frequency of the axial contact. There are many factors that could affect the resonance frequency, including variations in the mass of the spheres, local adhesion conditions and roughness of the surface. It is also possible that interparticle interactions, not accounted for in our model, could play a role [Boechler, Tournat]. To begin testing for some of these factors, we measured the SAW dispersion on different samples and compared SAW traces at many spots on the same sample. All the monolayer samples were fabricated with nominally identical particles, 1.08 mm silica spheres, on nearly identical substrates, float glass slides coated with 100 nm of aluminum, obtained from the EMF Corporation. The fabrication procedure is described in the previous chapter and is discussed in [Boechler]. The Fourier transforms of TG data with a period of 9.0 μm are presented in fig 6.1 for four different samples.

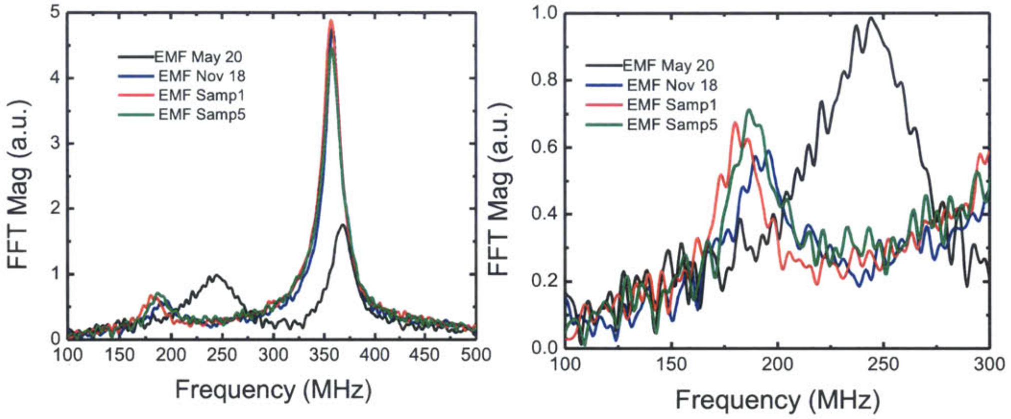

Fig 6.1 FFTs of time domain data collected at a TG period of 9.0 μm for four different microsphere monolayer samples. (Left) Spectra of the split Rayleigh peaks. (Right) Close-up of the lower branch peaks.

Three of the samples show almost the same spectra with only small shifts in peak position. The EMF May20 sample has a large change in the peak frequency as well as a much wider peak width. The only difference between the samples is the preparation procedure of the substrate. For EMF May20 the treatment was as follows: rinse with deionized (DI) water, place in 30% H_2O_2 solution for 1 hour, then rinse with acetone followed by isopropanol and finishing with DI water. The other three samples had a slightly different procedure: place in an acetone bath for 30 min, transfer to an isopropanol bath for 30 min, rinse with DI water, submerge in H_2O_2 for varying times at a temperature of 150 – 200 °C, place in DI water bath and rinse. For EMF Nov18 and EMF Samp5 the H_2O_2 treatment times were 5 min and for EMF Samp1 the treatment time was 1 hour. Based on the similarity of the treatment procedures, we would not expect such a large difference in the spectra. Although we have no definitive explanation for the disparity, the slight differences in the treatment procedures might offer possible explanations. The EMF May20 sample was only rinsed with acetone and isopropanol while the other three samples were soaked. Submerging the substrate in solvent for a long period of time would ensure that any organic residue was removed. Therefore, it is possible that the large change in the resonance frequency in the EMF may20 sample could be a result of surface contamination. Another difference in the preparation is the temperature of the H_2O_2 treatment. High temperature H_2O_2 accelerates the oxidation of the aluminum surface and can result in a different roughness of the surface. A higher surface roughness has been linked with a lower value of the contact stiffness for spheres on a substrate [Cheng, Fuller]. On the other hand, a larger surface roughness likely causes each sphere to experience a different contact interaction, resulting heterogeneous broadening of the peak.

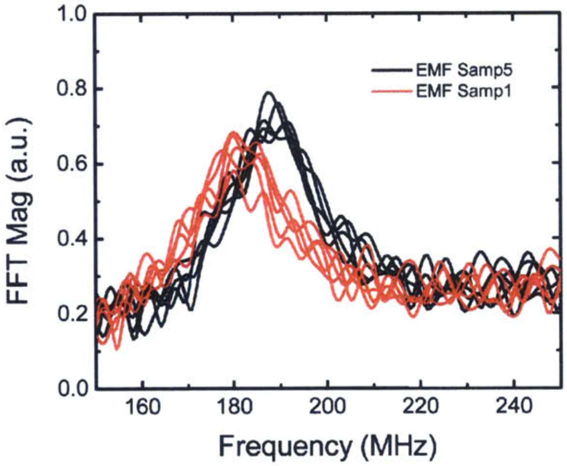

Fig 6.2 FFTs of time data collected at a TG period of 9.0 μm showing the lower branch peak of the SAW dispersion in two different monolayer samples. Five traces at different locations were collected for each sample.

For three of the samples presented above, we observed small variations in the resonance frequency. To determine whether this variation is significant, we tested the variability of the resonance frequency within one monolayer. Measurements from 5 different locations on the monolayer of EMF Samp1 and EMF Samp5 are presented in fig 6.2.

Although there is significant noise, the data show a clear separation of the peaks between the two samples. By finding the frequency of the maximum of the peak, we can develop some simple statistics to illustrate the variability of the samples. For sample 1 the average peak frequency is 180 MHz with a standard deviation of 2.5 MHz and for sample 5 the average peak frequency is 189 MHz with a standard deviation of 2 MHz. These results indicate that inhomogeneities within one monolayer sample likely contribute to the width of the peak and not to the observed differences between samples.

6.2.2 Changing humidity

Another possible contribution to the frequency of the axial contact resonance of the microspheres is the humidity at the time of the measurement. In humid environments a thin layer of water adheres to the surfaces of objects [Duran]. Due to the small size of the sphere-substrate contacts, adhered water fills the contacts and creates "water bridges", which act to increase the contact stiffness. To test the impact of water bridges in our experiments we compared the SAW dispersion on a monolayer of spheres in three distinct environments: in vacuum, under ambient lab conditions and in a 100% humid environment. All the measurements were carried out inside a Janis ST-100 cryostat. For measurements in vacuum, the chamber was pumped down using an Edwards rotary pump, typically obtaining pressures around 10 mtorr. The chamber was then opened up to allow the ambient air to fill the chamber and equilibrate for 48 hours. Finally, a small cup of water was placed in the bottom of the cryostat and was allowed to equilibrate for 48 hours, assuming this was sufficient time to obtain 100% humidity. Spectra for each of the environmental conditions are presented in fig 6.3 for a grating period of 11.5 μm.

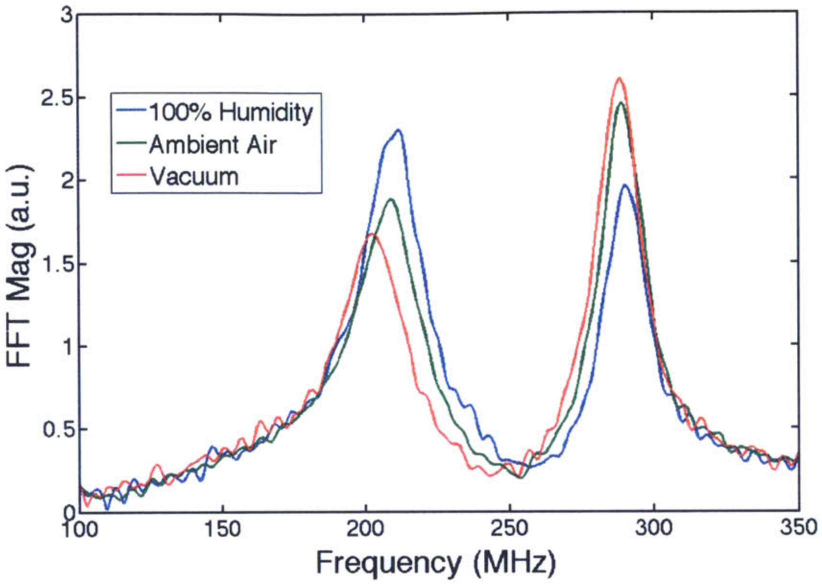

Fig 6.3 FFT magnitude of TG data collected at period of 11.5 μm for three different humidity conditions no humidity (red), low humidity (green), high humidity (blue). The frequency of the upper and lower branch peaks increase as a function of the humidity of the environment

A clear blue shift in the upper and lower branch peak positions is observed indicating a stiffening of the axial contact. The full dispersion relations were fit with the numerical results from eq 5.11. The resonance frequencies were determined to be 217 MHz, 224 MHz, and 227 MHz for the vacuum, ambient air, and the humid environment respectively. This is consistent with the presence of water bridges at higher humidity conditions as the added attractive force increases the stiffness of the axial contact resulting in an increase of the resonance frequency. Although we see a clear trend, measurements of the percent humidity are necessary to compare with models describing the added attractive forces due to water bridges [Duran]. We see a 5% difference in the measured resonance frequency between spheres in the evacuated environment and the humid environment. The small shift in the resonance frequency indicates that humidity is not a dominant factor in determining the stiffness of the contact, but the noticeable peak shift indicates this platform could be used as a humidity sensor.

In summary we observed differences in the resonance frequency of the axial contact of 1.08 μm silica spheres, due to sample fabrication and the humidity of the environment. To fully understand what properties affect the axial contact resonance, systematic studies varying conditions of the sample should be performed. For example, it would be informative to measure samples with different values of the RMS surface roughness. A characterization of what physical parameters of the sample, such as surface roughness, sphere roughness, sphere porosity and thickness of the alumina layer, influence the resonance frequency is essential before we can accurately model the work of adhesion. With this information we can make more direct comparisons to adhesion models and investigate the linear and nonlinear properties of adhesion up to the point at which the spheres detach from the substrate.

Once we have mastered sample fabrication, there are a number of interesting ways to investigate samples with different adhesive forces. For example, silica spheres coated with a small molecular functional group, such as an amine group (NH_2), are commercially available. The added functional group will alter the forces between the sphere and substrate, changing the measured frequency without significantly altering the other properties of the spheres, such as mass and radius. A demonstration of this effect would open the door to a wide range of possible applications for molecular sensing. For example, small spheres coated with proteins and other biologically active groups are available. Then, by exposing the array to a molecule that interacts with the functional group, the adhesion conditions would change and a shift in the resonance frequency would be observed. The small shifts observed so far indicate the sensitivity of the technique to varying adhesion conditions.

6.3 500 nm Spheres

Another way to test adhesion based contact models is by looking at the scaling behavior as a function of the particle diameter. For example, both the DMT model and the JKR model predict that the resonance frequency should scale as $R^{-7/6}$ [DMT ,JKR]. Guillet *et. al.* used optical interferometry to measure the vibrational modes of isolated gold spheres on a substrate, with R ranging from 90 nm to 900 nm [Guillet].

They compared the fundamental breathing mode of the spheres to the axial mode and found that the data were consistent with the theoretical prediction of $f_0 \propto f_b^{7/6}$ where f_b, is the frequency of the fundamental breathing mode and f_0 is the frequency of the axial contact vibration.

As we mentioned in the previous chapter, there are many potential differences between a single isolated sphere and an array of spheres. To test these predictions we fabricated an array of 500 nm spheres using the same convective self-assembly technique presented in [Boechler]. The SAW dispersion was measured with the TG technique for grating wavevectors ranging from 0.1 – 3.5 μm^{-1}. The dispersion relation and numerical fit are presented in fig 6.4.

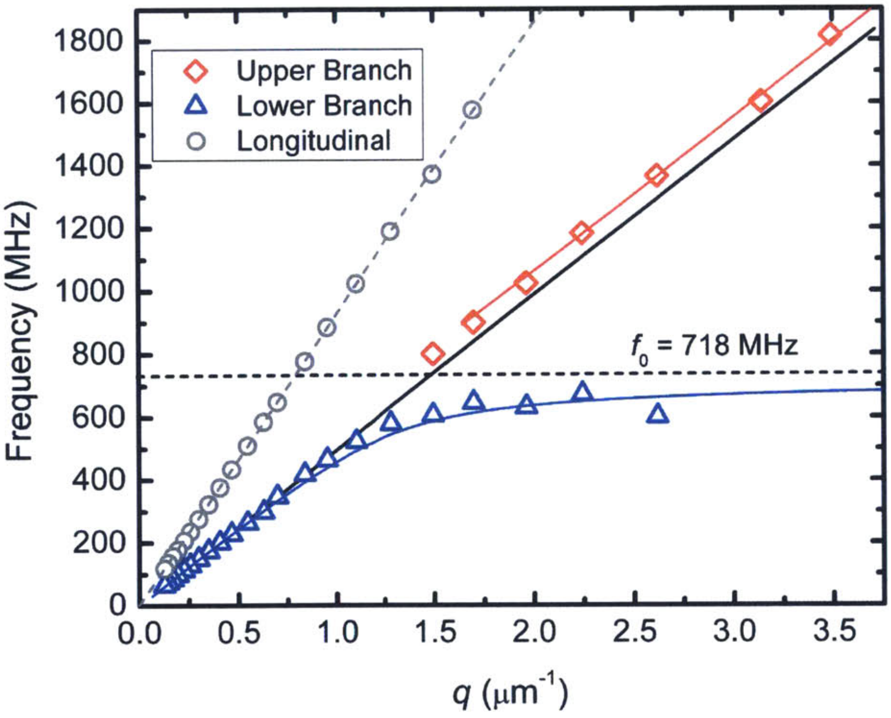

Fig 6.4 SAW dispersion in a monolayer of 518 nm spheres resulting in a resonance frequency of the axial contact of 718 MHz. The experimental data (open points) are plotted along with the numerical fits solid lines for upper branch (red) and lower branch (blue) and longitudinal wave (grey). The black line indicates the Rayleigh velocity of the float glass substrate of 3141 m/s and the grey dotted line corresponds to longitudinal velocity of 5711 m/s. The black dotted line is a guide to eye indicating the approximate position of the resonance frequency.

Using the procedure presented in chapter 5 we can estimate the resonance frequency of 518 nm spheres using the DMT model, which results in a frequency of 331 MHz. The numerical fit returns a resonance frequency of 718 MHz, which is more than two times the frequency predicted by the DMT model. Since we noted previously that our experimental results deviate from the DMT model, we can still test the scaling behavior by predicting the new frequency based on our measured frequency of 215 MHz for 1.08 mm spheres. In this case, for 518 nm spheres the scaling behavior predicted by the DMT model results in a frequency of 506 MHz, significantly lower than the observed value. The reason for large discrepancy is yet unexplained. We observed significant sample-to-sample variations in the 1.08 μm sphere samples and it is plausible that the same variability exists here. Although sample-to-sample variability is a possible explanation, the variation we observed previously is not large enough to explain the high frequency observed in the 518 nm spheres. In addition, as the sphere gets smaller the contact area also decreases which could increase the influence of surface roughness effects. The measured dispersion from 518 nm spheres highlights the need for additional experiments to explain the puzzling observations and test adhesion based contact models.

6.4 Microsphere waveguides

The observed avoided crossing in the monolayer of microspheres occurs for SAW wavelengths much larger than the particle size. As a result, this platform has similarity with a class of materials called "locally resonant metamaterials." The properties of these metamaterials have been presented in the literature for macroscopic systems [Liu00, Lemoult]. For example, Lemoult *et. al.* demonstrated sub-wavelength focusing of broadband sound waves using an array of soda cans, which behave as local acoustic resonators. Other examples demonstrate band gaps for surface waves formed from the vibrational resonance of micron sized pillars [Achaoui]. The local contact resonance in the monolayer of microspheres should also exhibit interesting wave control effects such as a thin strip of spheres acting as a waveguide for SAWs.

Here we present a study of TG measurements on a 6 μm wide strip of microspheres aimed at demonstrating waveguiding effects. The process for fabrication of the waveguides is detailed in [GanThesis]. Briefly, aluminum coated glass slides are covered with a photoresist polymer. Using photolithography, a 1 cm long trench is created with the desired width. The convective self-assembly technique is employed to deposit the microspheres in the trench and the remaining photoresist is removed. Structures as small as one particle wide can be fabricated with this technique [GanThesis].

Measuring a thin structure required a modification of the laser spot sizes. By using perpendicular cylindrical lenses with focal length 70 cm and 8 cm, the probe spot was reduced to 90 μm by 30 μm $1/e^2$ intensity radius. A pump spot size of 325 mm by 45 mm $1/e^2$ intensity radius was achieved using a 10 cm cylindrical lens. The average power of the quasi-cw probe beam was 7.25 mW and the pump pulse energy was 0.25 μJ. A CCD image of the waveguide and the laser spots are shown in fig 6.5. The waveguide appears bright due to scattering of incident light from a lamp used to enhance the optical image.

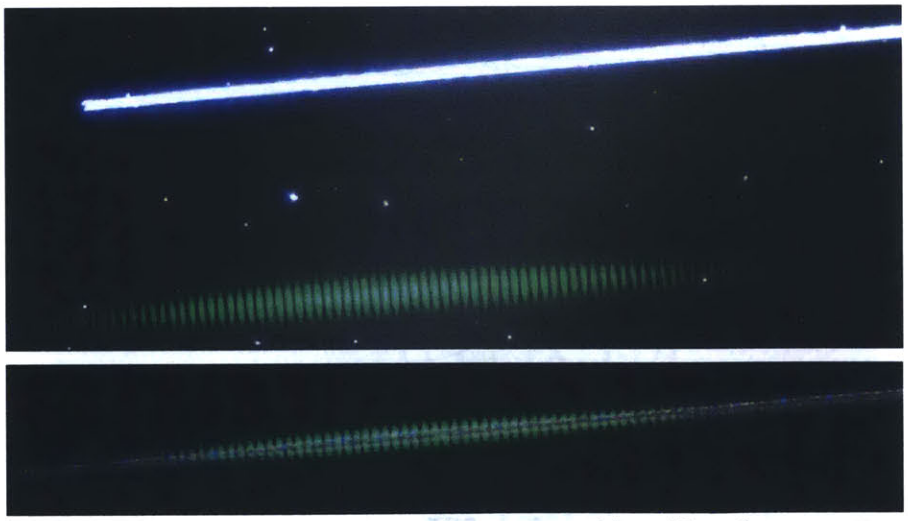

figure 6.5 (Top) CCD image showing 6 μm microsphere wave guide and interference pattern of TG excitation pulses. (bottom) CCD image of the overlap of the excitation spot and the waveguide structure.

In the experiments, the laser spot was translated toward and over the 6 μm waveguide structure and TG traces were collected in increments of 2 μm translation. The TG period was 11.5 μm (q = 0.55 μm^{-1}). The spectra are shown in fig 6.6 where each trace is offset to indicate the incremental movement of the spot. When the spot is far away from the structure, we observe a peak corresponding to the Rayleigh wave in the substrate. As the spot approaches the structure, a new peak appears at a lower frequency than the Rayleigh wave, just above 250 MHz. The new peak due to the microsphere waveguide extends for tens of microns above and below the structure. The additional peak is present for 25 of the traces corresponding to a translation length of around 50 μm, consistent with a probe spot width of ~60 μm. Small signatures of the Rayleigh wave in the substrate remain while directly on the structure as the spot is larger than the waveguide structure. Interestingly, the additional peak, which should correspond to the resonance mode doesn't split as would be expected from measurements on an extended monolayer structure. To investigate this observation, we measured the dispersion of the structure.

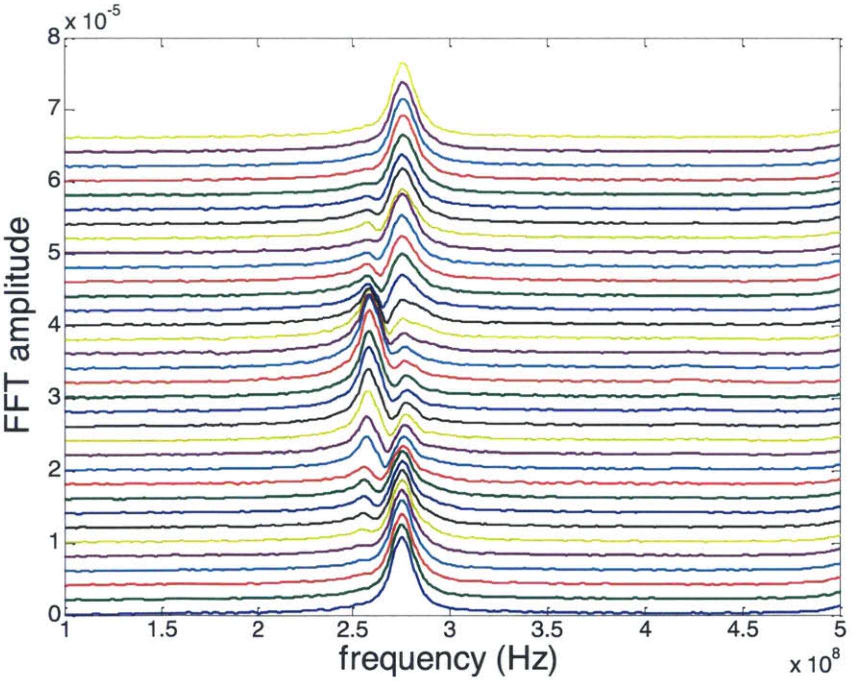

fig 6.6 Fourier transforms of TG time data. The spot was initially located below the waveguide structure and each trace moving up was taken at 2 μm increments until the spot had fully cleared the structure.

The dispersion was measured by aligning the TG spot directly on top of the waveguide using a CCD camera, as shown in fig 6.5. TG data were collected as a function of wavevector from 0.3 to 0.85 μm^{-1}. The spectra for a selection of the wavevectors are presented in fig 6.7 along with spectra on the substrate as a comparison.

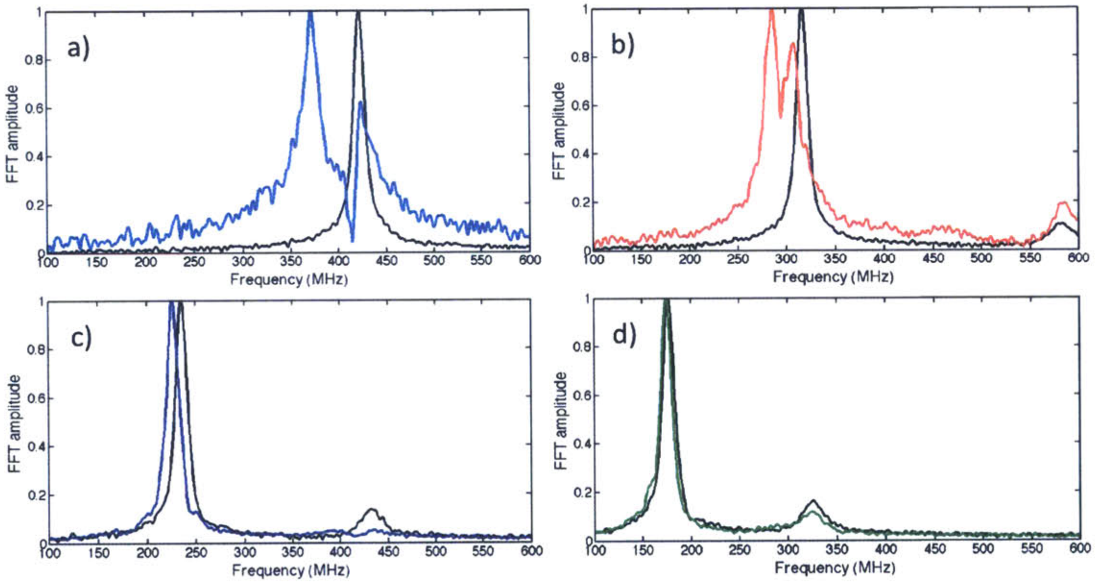

fig 6.6 Representative spectra for TG measurements on a 6 μm wide waveguide of 1.08 μm silica spheres for on waveguide (color) and off waveguide (black). The wavevectors shown are 0.84 μm^{-1} (a), 0.63 μm^{-1} (b), 0.47 μm^{-1} (c) and 0.35 μm^{-1} (d).

At higher wavevectors the spectra show additional peaks below the Rayleigh frequency. Based on calculations of the waveguide dispersion [Kumar] in a 15 μm waveguide, the lowest order waveguide mode has a similar dispersion to that of the perfect crystal while the upper branch disappears. The lower branch of the waveguide dispersion matches the Rayleigh wave at low wavevector and approaches the resonance frequency at high wavevector, the only difference being that the peak frequencies are slightly blue shifted. According to the calculations, the additional peaks corresponding to the lower branch should not appear above the resonance frequency. At a TG wavevector of 0.84 μm^{-1}, the peak resembling the lower branch has a frequency significantly higher than the resonance frequency of the axial contact (around 220 MHz). Thus, it is unclear whether the additional peaks arise from the axial contact resonance. One possible explanation is that residual photoresist from the fabrication process is interfering with the contact and causing a strong bond between the substrate and the sphere. In this case, the waveguide would behave as a solid structure and cause a downshift in the Rayleigh wave frequency due to mass loading. A mass loading type response would not be limited by the resonance frequency as expected for the axial contact. Although we see a clear change in the spectra due to the waveguide structure, it is unclear if the changes are caused by the axial contact resonance or by other factors, namely unremoved polymer from the fabrication process. Experiments on cleaner waveguide structures would clarify these results.

6.5 SAW filtering

An alternative approach to demonstrating wave control using microspheres is to create a SAW filter. SAW filters have a wide range of applications in microelectronics and signal processing [Campbell]. A microsphere based SAW filter resembles a waveguide structure, but the SAWs propagate perpendicular to the structure and are attenuated before passing through. A tapered strip, roughly 60 - 120 μm wide, was fabricated using a monolayer of 1.02 μm polystyrene (PS) spheres and a microcontact printing technique. The fabrication of the PS monolayer was adapted from [Vogel]. Briefly, PS microspheres were dispersed in a 50-50 water-ethanol solution. After adding sodium dodecyl sulfate a monolayer of spheres selfassembled at the water-air interface and were then lifted out using a glass substrate coated with aluminum [Khanolkar]. To create the strip, a polydimethylsiloxane (PDMS) stamp was created by placing two blocks of PDMS on a glass slide with a separation of ~100 μm using a mechanical stage. The stamp was pressed onto the monolayer area and the spheres attached to the PDMS. Once the stamp was removed only spheres in the area between the two PDMS blocks remained on the substrate. The strip was slightly tapered due to the difficulty of achieving a high degree of parallelism between the two PDMS blocks. An image of the strip courtesy of Morgan Hiriawa is shown in fig 6.7

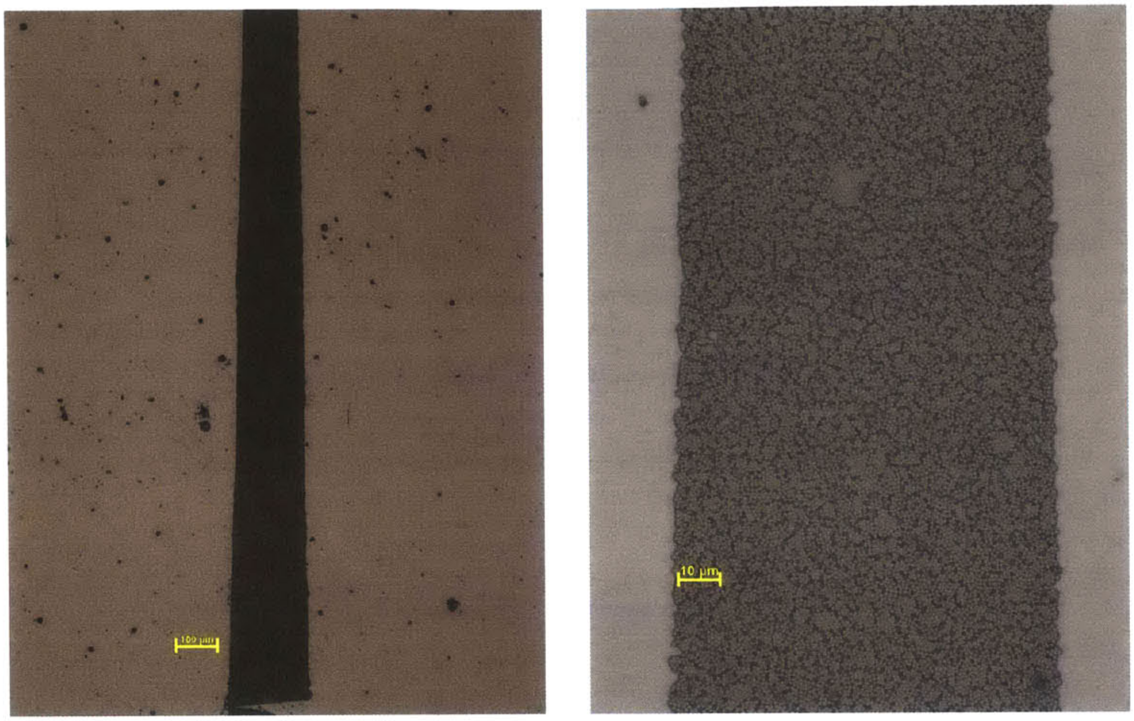

fig 6.7 Optical microscope image of the tapered strip under 5x (left) and 50 x (right) magnification.

By generating a SAW on one side of the structure and detecting it on the other, we can measure the attenuation caused by the strip of microspheres. This can be achieved by offsetting the pump and probe spots of the TG technique. TG measurements with offset spots have been demonstrated previously in the literature [Maznev98]. Since we image the optical phase mask onto the sample, offsetting the pump and probe spots that are incident on the phase mask results in offset spots on the sample. We offset the spots simply by translating the pump beam on the phase mask so that there was roughly 500 μm between the edges of the spots. TG measurements for a wide range of wavevectors were carried out with the strip between the spots and with no spheres between the spots called on-strip and off-strip respectively. (Note that neither the excitation nor the probe beams irradiated the microsphere strip, but the SAW generated by the excitation beams traverses the strip in the "on-strip" measurements and only traverses the bare substrate in the "off-strip" measurements.) TG time traces for three different wavevectors are presented in fig 6.8

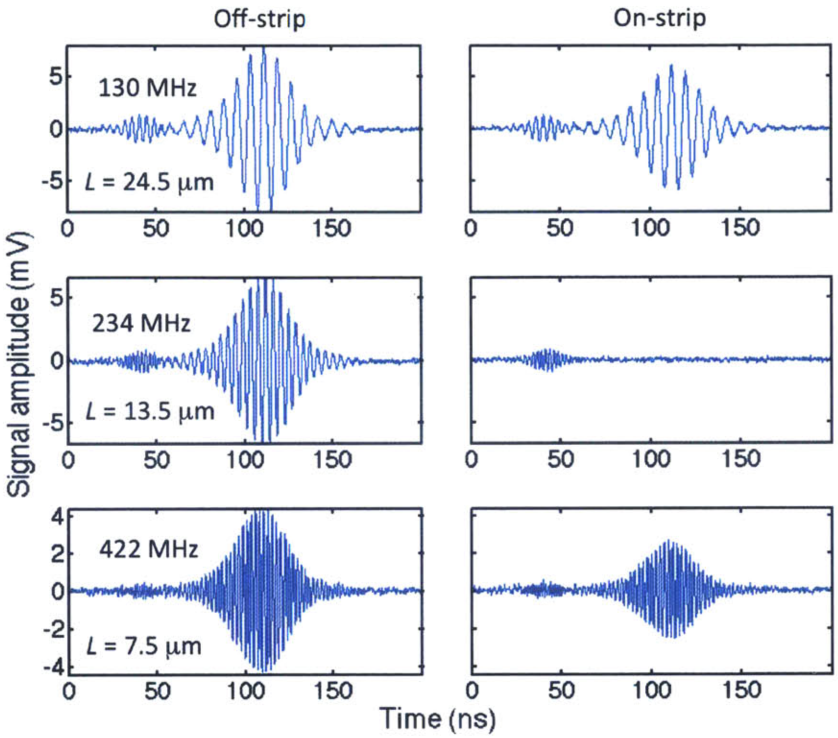

fig 6.8 Time traces comparing SAW propagation on substrate (off-strip) and SAW transmission through the strip (on-strip) for three TG periods.

In each trace we see two wavepackets, the first corresponding to the longitudinal wave and the second corresponding to the Rayleigh wave. The longitudinal wavepacket arrives at the probing region earlier due to its higher group velocity. The wavepackets have a Gaussian temporal profile matching the Gaussian spatial profile of the optical excitation spot. Comparing the on-strip and off-strip measurements we observe a reduction in the amplitude of the Rayleigh wavepacket and no change in the longitudinal wavepacket. When the frequency of the Rayleigh wave matches the frequency of the axial contact resonance (13.5 μm grating period) the Rayleigh wavepacket disappears completely. We performed a full set of TG measurements off and on strip, for TG periods ranging from 24.5 μm to 7.5 μm. To get a finer spacing between TG periods we implemented the angled phase mask approach detailed in section 2.6. In addition to the normal incidence measurements we collected data at phase mask angles of 15°, 20° and 25° for grating periods 9 μm, 10 μm, 11.5 μm, 13.5 μm and 15.5 μm. Fourier transforms of the on-strip data presenting only the Rayleigh wave peak for each trace are shown in fig 6.9.

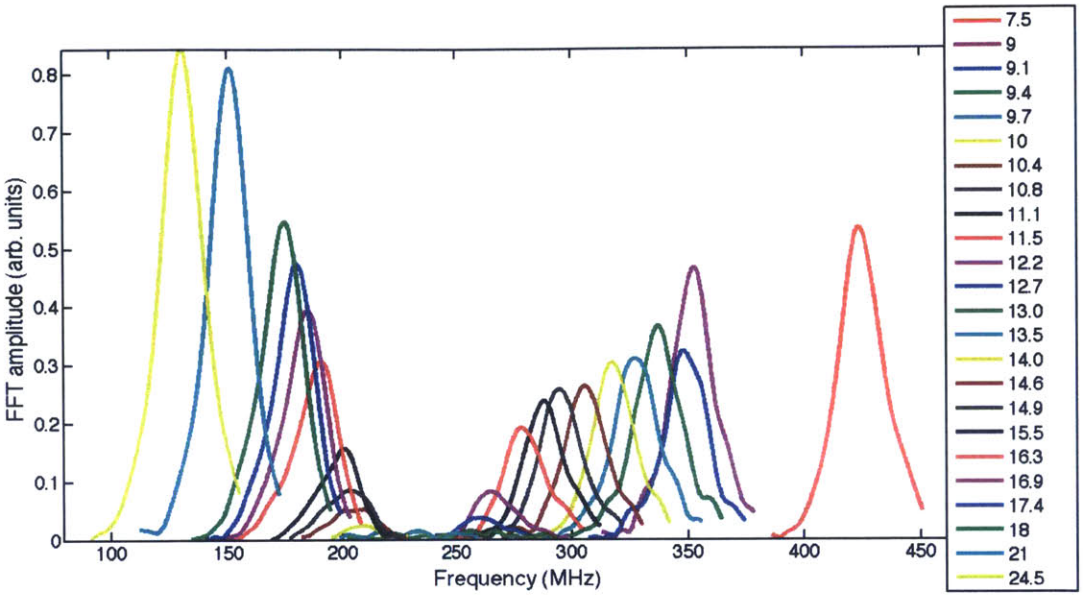

Fig 6.9 Rayleigh wave peaks from on-strip TG measurements demonstrating the frequency dependent attenuation due to a strip of microspheres. The legend on the right indicates the TG period in micrometers.

The dip between 200 MHz and 275 MHz is caused by attenuation of the SAW due to the axial contact resonance of the microspheres. A resonance frequency of 235 MHz was determined by measuring the dispersion with overlapped spots inside the strip. The large attenuation could be a result of many effects. The avoided crossing creates an acoustic band gap between the upper and lower branch. If the SAW frequency is sufficiently narrow to fit within the band gap, there should be 100% reflection of the wave. There is also a large impedance mismatch between due to the difference in phase velocity between the SAW in and out of the structure. The impedance mismatch contributes to the reflection even outside the band gap. In modes that generate a large displacement in the spheres (the modes near the resonance frequency) there may also be higher attenuation due to the heterogeneities in the contact. The attenuation from inhomogeneities is further increased by the low group velocity near the resonance, visualized as the flat lower branch in the dispersion relation (fig 5.6 and 6.4). In similar experiments performed on microsphere strips fabricated with the photoresist technique (not presented here) we did observe a reflection in the TG signal, although this reflection could be a result of residual photoresist rather than the contact resonance. The absence of a reflection in the current experiment could be explained by the apparent disorder of the edge of the strip seen in fig 6.7. The disordered structure will scatter the SAW so no reflection reaches the probing region.

The attenuation coefficient as a function of frequency was calculated by comparing the magnitude of the off strip and on strip Fourier peaks with the following expression,

$$\text{Attenuation coefficient} = \frac{R_{off}}{R_{on}} \times \frac{L_{on}}{L_{off}},$$

where R is the magnitude of the Fourier peak for the Rayleigh wave, L is the magnitude of the Fourier peak for the longitudinal wave, and on and off refer on-strip and off-strip measurements respectively. The magnitude of the longitudinal wave was included in this way to account for any changes in the magnitude of the signal due to changes in alignment between on-strip and off-strip measurements. The ratio of the longitudinal magnitudes was between 0.85 and 1.1 for all traces indicating only small variations in alignment. The attenuation coefficient as a function of frequency is presented in fig 6.10

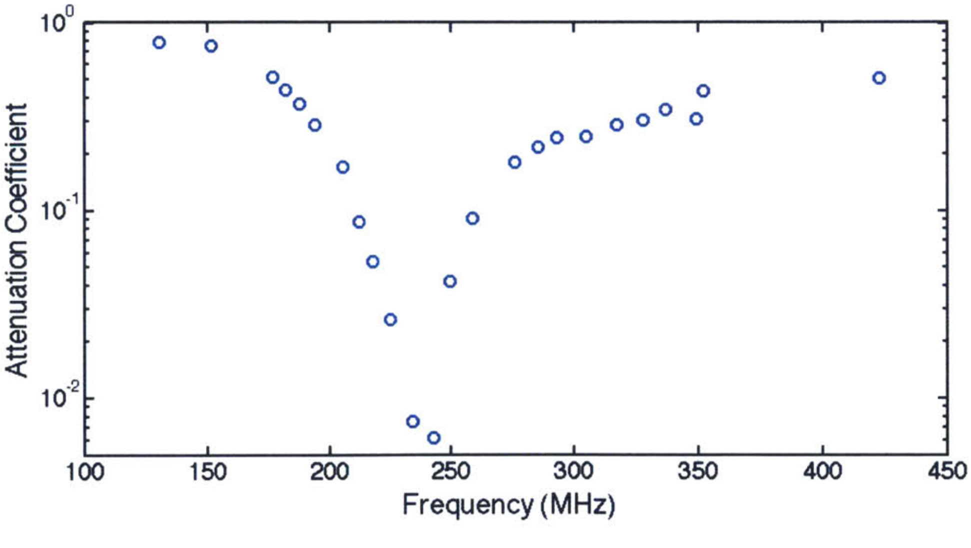

fig 6.10 Attenuation coefficient as a function of frequency of SAW propagation through a ~100 μm strip of PS spheres.

The maximum attenuation occurs at a frequency slightly above the resonance frequency of 235 MHz. The two lowest points are not true measurements of the attenuation since there was no discernable Rayleigh wave signature in the data, as seen in in the middle row of fig 6.8. Rather they show an upper limit of the attenuation since we used the magnitude of the noise at the expected frequency for the calculation.

The frequency dependent attenuation induced by a strip of microspheres opens the door for applications in SAW filtering. Since the frequency of maximum attenuation is dependent on the axial contact resonance and thus on adhesion, we can create filters with tunable frequencies through in situ variations of adhesion. It would also be possible to create switches by sending a high amplitude SAW to knock off the spheres, eliminating attenuation while they are in the air. Then, once the spheres settled back on the surface, the attenuation would return to normal. The relatively simple fabrication and small scale of microsphere monolayer makes this platform appealing for microelectrical mechanical devices.

6.6 Nonlinear dynamics

The Hertz contact, the primary interaction in granular crystals, is inherently non-linear, but so far our measurements have all remained in the linear regime. The non-linearity of granular crystals has been observed for much larger particles but has yet to be explored for micron sized particles [Theocharis, Gantzounis, Bonanomi]. Here we present our observations of a nonlinear response in a monolayer of 1.08 mm silica spheres. Measurements were performed on a monolayer of microspheres with a TG period of 15.50 μm by increasing the laser fluence each time up to the damage threshold. The resulting time traces were all normalized to account for the increase in signal with laser fluence. The Fourier transforms of the time data are presented in fig 6.11 showing the upper and lower branch of the dispersion.

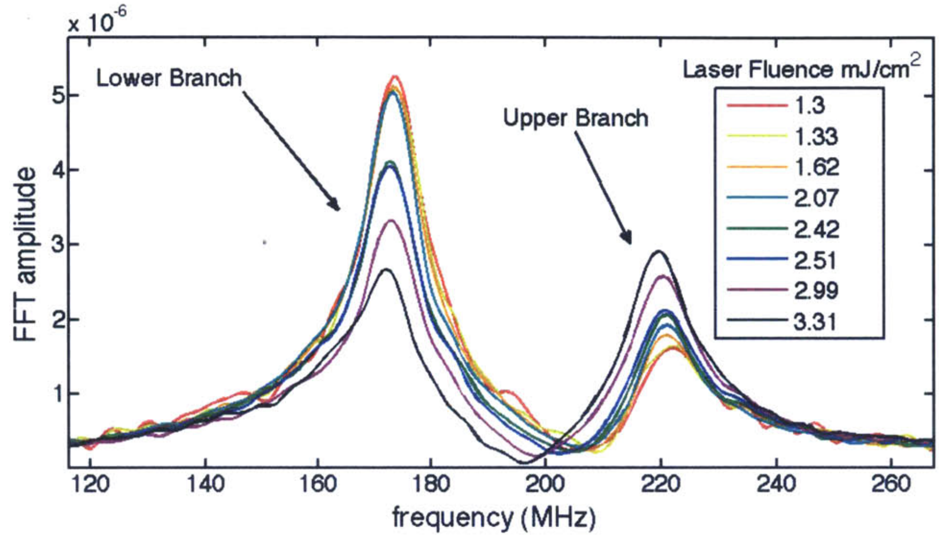

Fig 6.11 FFTs of the fluence dependent measurements of SAW propagation in a monolayer of 1.08 mm silica spheres.

If the axial contact resonance were completely linear than we would expect no change in the shape or position of the peaks. The observed changes to the spectra as a function of laser fluence confirm the nonlinearity of the axial contact. The most noticeable effect is the change in the relative amplitudes of the lower branch and upper branch peaks. At low fluence the amplitude of the lower branch peak is higher than the amplitude of the upper branch. As the fluence increases, the relative amplitude of the lower branch decreases while that of the upper branch increases. In addition, there is a slight shift of the peak positions of both the upper and lower branches to lower frequencies. These observations are consistent with a down shift in the resonance frequency upon large amplitude excitation [Bonanomi, Theocharis09]. The change in relative amplitude is also indicative of the softening of the contact. As the resonance frequency decreases it moves farther from the excitation frequency and the excitation is less efficient at exciting the sphere motion. As a result, the signal from the sphere motion, namely the low frequency peak in the spectra, decreases in amplitude. The experiment presented here demonstrates the nonlinear nature of the microscale contact and provides the groundwork to quantify a nonlinear model for a monolayer of microspheres.

6.7 Summary

In this chapter we presented experiments that highlight the sensitivity of the axial contact resonance of an array of microspheres to varying environmental conditions. We saw a significant change in the resonance frequency between samples with slightly different fabrication steps, and a dependence of the frequency on the humidity of the atmosphere. Future experiments with controlled parameters will help to model quantitatively the factors that determine the resonance frequency. In addition, dispersion measurements on 500 nm spheres showed a much higher resonance frequency than predicted by adhesion models. We demonstrated that a ~100 μm strip of microspheres fully attenuates SAWs near the resonance frequency, showing the potential for using microspheres as SAW filters in microelectronic devices. Finally we demonstrated the nonlinearity of the microscale contact opening up possibilities for many future nonlinear studies.

References

[Achaoui] Achaoui, Y., Khelif, A., Benchabane, S., Robert, L. & Laude, V. Experimental observation of locally-resonant and Bragg band gaps for surface guided waves in a phononic crystal of pillars. *Physical Review B* **83**, 104201 (2011).

[Adachi] S. Adachi. *GaAs and Related Materials, Bulk Semiconducting and Superlattice Properties* (World Scientific Publishing Co, Singapore, 1994)

[Asheghi] Asheghi, M., Touzelbaev, M., Goodson, K., Leung, Y.K. & Wong, S.S. Temperature-dependent thermal conductivity of single-crystal silicon layers in SOI substrates. *Journal of heat* **120**, (1998).

[Ashcroft] N. W. Ashcroft, N.D. Mermin. *Solid State Physics.* (Saunders College Publishing, Orlando, 1976)

[Aubain10] Aubain, M.S. & Bandaru, P.R. Determination of diminished thermal conductivity in silicon thin films using scanning thermoreflectance thermometry. *Applied Physics Letters* **97**, 253102 (2010).

[Aubain11] Aubain, M.S. & Bandaru, P.R. In-plane thermal conductivity determination through thermoreflectance analysis and measurements. *Journal of Applied Physics* **110**, 084313 (2011).

[Baghai-Wadji] A. R. Baghai-Wadji, V.P. Plessky, and A.V. Simonian, Sov. Phys. Acoust. 38, 442 (1992).

[Berne] B.J. Berne, R. Pecora. *Dynamic Light Scattering with Applications to Chemistry, Biology, and Physics.* (Dover Publications, Mineola, NY, 2000).

[Bhushan] B. Bhushan, *Handbook of Micro/Nano Tribology* (CRC Press, Boca Raton, FL, 1999), 2nd. ed.

[Blakemore] J.S. Blakemore, *Solid State Physics* (Cambride University Press, Cambridge, 1985).

[Boechler] Boechler, N., Eliason, J.K., Kumar, a., Maznev, a. a., Nelson, K. a. & Fang, N. Interaction of a Contact Resonance of Microspheres with Surface Acoustic Waves. *Physical Review Letters* **111**, 036103 (2013).

[Bonanomi] Bonanomi, L., Theocharis, G. & Daraio, C. Wave propagation in granular chains with local resonances. *Physical Review E* **91**, 033208 (2015).

[Brekhovskikh] L.M. Brekhovskikh. *Waves in Layered Media* (Academic Press, New York 1960).

[Broido] Broido, D. a., Malorny, M., Birner, G., Mingo, N. & Stewart, D. a. Intrinsic lattice thermal conductivity of semiconductors from first principles. *Applied Physics Letters* **91**, 231922 (2007).

[Burns] G. Burns, *Solid State Physics* (Academic Press, Orlando, 1985).

[Cahill03] Cahill, D.G. *et al.* Nanoscale thermal transport. *Journal of Applied Physics* **93**, 793 (2003).

[Cahill14] Cahill, D.G. et al. Nanoscale thermal transport. II. 2003–2012. Applied Physics Reviews 1, 011305 (2014).

[Callaway] Callaway, J. Model for lattice thermal conductivity at low temperatures. *Physical Review* **113**, 1046–51 (1959).

[Campbell] S. Campbell, *The Science and Engineering of Microelectronic Fabrication,* (Oxford University Press, New York, 2001)

[Canalejas] Canalejas-tejero, V., Ibisate, M., Golmayo, D., Blanco, A. & Cefe, L. Qualitative and Quantitative Analysis of Crystallographic Defects Present in 2D Colloidal Sphere Arrays. *Langmuir* **28**, 161–167 (2012).

[Carslaw] H. S. Carslaw, J. C. Jaeger. Conduction of Heat in Solids. (Oxford University Press, Osford, 1986)

[Capinsky] Capinski, W.S. & Maris, H.J. Improved apparatus for picosecond pump-and-probe optical measurements. *Review of Scientific Instruments* **67**, 2720 (1996).

[Casimir] Casimir, H. Note on the conduction of heat in crystals. *Physica* 495–500 (1938)

[Chávez12] Chávez, E., Cuffe, J., Alzina, F. & Torres, C.M.S. Calculation of the specific heat in ultra-thin free-standing silicon membranes. *Journal of Physics: Conference Series* **395**, 012105 (2012).

[Chávez14] Chávez-Ángel, E. *et al.* Reduction of the thermal conductivity in free-standing silicon nano-membranes investigated by non-invasive Raman thermometry. *APL Materials* **2**, 012113 (2014).

[Chen96] Chen, G. Nonlocal and Nonequilibrium Heat Conduction in the Vicinity of Nanoparticles. *Journal of Heat Transfer* **118**, 539 (1996).

[Chen05] G. Chen, *Nanoscale Energy Transport and Conversion* (Oxford University Press, New York, 2005).

[Chen03] Chen, G., Dresselhaus, M.S., Dresselhaus, G., Fleurial, J.-P. & Caillat, T. Recent developments in thermoelectric materials. *International Materials Reviews* **48**, 45–66 (2003).

[Cheng] Cheng, W., Dunn, P.F. & Brach, R.M. Surface Roughness Effects on Microparticle Adhesion. *The Journal of Adhesion* 929–965 (2002)

[Choi] Choi, G.-M., Wilson, R.B. & Cahill, D.G. Indirect heating of Pt by short-pulse laser irradiation of Au in a nanoscale Pt/Au bilayer. *Physical Review B* **89**, 064307 (2014).

[Collier] R. J. Collier, C.B. Burckhardt, L.H. Lin, *Optical Holography*. (Academic Press, 1971).

[Collins14] Collins, K.C., Maznev, A. a., Tian, Z., Esfarjani, K., Nelson, K. a. & Chen, G. Non-diffusive relaxation of a transient thermal grating analyzed with the Boltzmann transport equation. *Journal of Applied Physics* **114**, 104302 (2013).

[Cuffe13] Cuffe, J. *et al.* Lifetimes of Confined Acoustic Phonons in Ultrathin Silicon Membranes. *Physical Review Letters* **110**, 095503 (2013).

[Cuffe14] Cuffe, J. et al. Reconstructing phonon mean free path contributions to thermal conductivity using nanoscale membranes. arXiv:1408.6747

[Dadusc] Dadusc, G. et. al. Advances in Grating-Based Photoacoustic Spectroscopy for the Study of Protein Dynamics. *Israel Journal of Chemistry* **38**, 191–206 (1998).

[Daly] Daly, B.C. Picosecond ultrasonic measurements of attenuation of longitudinal acoustic phonons in silicon. *Physical Review B* **80**, 1–5 (2009).

[Debye] P. Debye, "Zustandsgleichung und Quantenhypothese mit einem Anhang über Wärmeleitung," in Vorträge über die kinetische Theorie der Materie und der Elektrizität, edited by M. Planck, P. Debye, W. Nernst, M. Smoluchowski, Arnold Sommerfeld, and H. A. Lorentz (B. G. Teubner, Leipzig, 1914), pp. 17–60.

[Deinzer10] Deinzer, G., Birner, G. & Strauch, D. Ab initio calculation of the linewidth of various phonon modes in germanium and silicon. *Physical Review B* **67**, 144304 (2003).

[Delaire11] Delaire, O. *et al.* Giant anharmonic phonon scattering in PbTe. *Nature materials* **10**, 614–9 (2011).

[DMT] Muller, V.M., Derjaguin, B.V., Toporov, Y.P. On Two Methods of Calculation of the Force of Sticking of an Elastic Sphere to a Rigid Plane. *Colloids and Surfaces* **7**, 251–259 (1983).

[Dresselhaus] Dresselhaus, M.S. *et al.* New Directions for Low-Dimensional Thermoelectric Materials. *Advanced Materials* **19**, 1043–1053 (2007).

[Duran] J. Duran, *Sands, Powders and Grains: An Introduction to the Physics of Granular Materials.* (Springer-Verlag, New York, 2000)

[Eguiluz] Eguiluz, A.G., and Maradudin, A.A. Effective Boundary Conditions for a Semi-Infinite Elastic Medium Bounded by a Rough Planar Stress-Free Surface. *Physical Review B* **28**, 711 (1983).

[Eichler] H.J. Eichler, P. Guther, abd D.W. Phol, *Laser Induced Dynamic Gratings*, (Springer, Berlin, Heidelberg, 1986)

[Esfarjani10] Esfarjani, K., Chen, G. & Stokes, H. Heat transport in silicon from first-principles calculations. Physical Review B 84, 1–11 (2011).

[Every] Every, A.G. Measurement of the near-surface elastic properties of solids and thin supported films. *Measurement Science and Technology* **13**, R21 (2002).

[Flubacher] Flubacher, P., A. J. Leadbetter, and J. A. Morrison, *Phil. Mag.* 4, 39 (1959) 273-294.

[Fourier] Fourier, J. *Analytical Theory of Heat.* (Paris, Gauthier-Villars, 1882).

[Fuchs] Fuchs, K. The conductivity of thin metallic films according to the electron theory of metals. *Proc. Cambridge Philos. Soc* **157**, 100–108 (1938).

[Fuller] Fuller, K.N.G. and Tabor, D. The Effect of Surface Roughness on the Adhesion of Elastic Solids. *Proc. R. Soc. Lond.* **345**, 327 (1975).

[GanThesis] T. Gan Masters Thesis. (Massachusetts Institute of Technology, Cambridge, MA, 2014)

[Gantzounis] Gantzounis, G., Serra-Garcia, M., Homma, K., Mendoza, J.M. & Daraio, C. Granular metamaterials for vibration mitigation. *Journal of Applied Physics* **114**, 093514 (2013).

[Garova] Garova, E., Maradudin, a. & Mayer, a. Interaction of Rayleigh waves with randomly distributed oscillators on the surface. *Physical Review B* **59**, 13291–13296 (1999).

[Goodno] Goodno, G.D., Dadusc, G. & Miller, R.J.D. Ultrafast heterodyne-detected transient-grating spectroscopy using diffractive optics. *Optical Society of America* **15**, 1791–1794 (1998).

[Guillet] Guillet, Y., Audoin, B., Ferrié, M. & Ravaine, S. All-optical ultrafast spectroscopy of a single nanoparticle-substrate contact. *Physical Review B* **86**, 035456 (2012).

[Hao] Hao, Z., Zhichao, L., Lilin, T., Zhimin, T., Litian, L. & Zhijian, L. Thermal conductivity measurements of ultra-thin single crystal silicon films using improved structure. (2006).

[Henry] Henry, A.S. & Chen, G. Spectral phonon transport properties of silicon based on molecular dynamics simulations and lattice dynamics. *Journal of Computational and Theoretical Nanoscience* **5**, 141–152 (2008).

[Hertz] H. Hertz, *J. Reine Angrew. Math.* **92.** 156 (1882).

[Highland] Highland, M. *et al.* Ballistic-phonon heat conduction at the nanoscale as revealed by time-resolved x-ray diffraction and time-domain thermoreflectance. *Physical Review B* **76**, 1–7 (2007).

[Hinrichsen] H. Hinrichsen and D.E. Wolf, *The Physics of Granular Media*, (Wiley-VCH Verlag GmbH & Co. KGaA, Weinheim, 2004)

[Hiriawa] PDMS stamping and optical microscope images courtesy of Morgan Hiriawa from the Department of Mechanical Engineering at the Universtiy of Washington.

[Holland63] Holland, M. Analysis of lattice thermal conductivity. *Physical Review* **132**, 2461 (1963).

[Holland64] Holland, M. Phonon scattering in semiconductors from thermal conductivity studies. *Phys. Rev* **134**, A471–A480 (1964).

[Hoogeboom-Pot] Hoogeboom-Pot, K.M. *et al.* A new regime of nanoscale thermal transport: Collective diffusion increases dissipation efficiency. *Proceedings of the National Academy of Sciences* **112**, 201503449 (2015).

[Huang] Huang, M.-J., Chang, T.-M., Liu, C.-K. & Yu, C.-K. A theoretical study of the specific heat and Debye temperature of low-dimensional materials. *International Journal of Heat and Mass Transfer* **51**, 4470–4479 (2008).

[Israelachvili] J. Israelachvili, *Intermolecular and Surface Forces* (Elsevier Inc., Burlington, MA, 2011)

[JKR] K.L. Johnson, K. Kendall, A.D. Roberts, *Surface energy and contact of elastic solids*, Proc. R. Soc. Lond. A 324 (1971) 301–313.

[JohnsonPhD] J. Johnson. PhD Thesis. (Massachusetts Institute of Technology, Cambridge, MA 2011).

[Johnson12] Johnson, J.A. *et al.* Phase-controlled, heterodyne laser-induced transient grating measurements of thermal transport properties in opaque material. *Journal of Applied Physics* **111**, 023503 (2012).

[Johnson13] Johnson, J. a. *et al.* Direct Measurement of Room-Temperature Nondiffusive Thermal Transport Over Micron Distances in a Silicon Membrane. *Physical Review Letters* **110**, 025901 (2013).

[Ju] Ju, Y. & Goodson, K. Phonon scattering in silicon films with thickness of order 100 nm. *Applied Physics Letters* **74**, 3005 (1999).

[Kapitza] P.L. Kaptiza. J. Phys (Moscow) **4**, 181 (1941).

[Khanolkar] The polystyrene monolayer was fabricated by Amey Khanolkar in the Department of Mechanical Engineering at the University of Washington.

[Koh] Koh, Y. & Cahill, D. Frequency dependence of the thermal conductivity of semiconductor alloys. *Physical Review B* **76**, 1–5 (2007).

[Kosevich] Kosevich, Yu.A. and Syrkin, E.S. Long Wavelength Surface Oscillations of a Crystal with an Adsorbed Monolayer. *Physics Letters A* **135**, 8–12 (1989).

[Kumar] Calculations performed by Anshuman Kumar from the Department of Mechanical Engineering at the Massachusetts Institute of Technology.

[Käding] Käding, O.W., Skurk, H., Maznev, A.A. & Matthias, E. Transient thermal gratings at surfaces for thermal characterization of bulk materials and thin films. Applied Physics A Materials Science Processing 61, 253–261 (1995).

[Landau] L. D. Landau, E. M. Lifshitz. *Theory of Elasticity.* (Pergamon Press, New York, 1970).

[Lemoult] Lemoult, F., Fink, M. & Lerosey, G. Acoustic Resonators for Far-Field Control of Sound on a Subwavelength Scale. *Physical Review Letters* **107**, 064301 (2011).

[Li] Li, C., Sjodin, T. & Dai, H. Photoexcited carrier diffusion near a Si(111) surface: Non-Negligible consequence of carrier-carrier scattering. *Physical Review B* **56**, 252–255 (1997).

[Lide] D.R. Lide, *Handbook of Chemistry and Physics* (CRC Press, Boca Raton, FL, 2003).

[Liu] Liu, W. & Asheghi, M. Thermal Conductivity Measurements of Ultra-Thin Single Crystal Silicon Layers. *Journal of Heat Transfer* **128**, 75 (2006).

[Liu00] Liu, Z. Locally Resonant Sonic Materials. *Science* **289**, 1734–1736 (2000).

[Luo] Luo, T., Garg, J., Shiomi, J., Esfarjani, K. & Chen, G. Gallium arsenide thermal conductivity and optical phonon relaxation times from first-principles calculations. *EPL (Europhysics Letters)* **101**, 16001 (2013).

[Ma] Ma, J. *et al.* Glass-like phonon scattering from a spontaneous nanostructure in AgSbTe2. *Nature nanotechnology* **8**, 445–51 (2013).

[Majumdar93] Majumdar, A. Microscale heat conduction in dielectric thin films. *ASME Transactions Journal of Heat Transfer* **1**, 7–16 (1993).

[Maradudin] A. A. Maradudin and D. L. Mills, Ann. Phys. 100, 262 (1976).

[Marconnet13] Marconnet, A.M. From the Casimir Limit to Phononic Crystals: 20 Years of Phonon Transport Studies Using Silicon-on-Insulator Technology. *Journal of Heat Transfer* **135**, 061601 (2013).

[Mason] W.P. Mason and R.N. Thurston, *Physical Acoustics* (Academic Press, New York, 1970)

[Maznev98] Maznev, A., Nelson, K. & Rogers, J.A. Optical heterodyne detection of laser-induced gratings. Optics letters 23, 1319–1321 (1998).

[Maznev13] Maznev, A., Johnson, J. & Nelson, K. Onset of nondiffusive phonon transport in transient thermal grating decay. *Physical Review B* **84**, 1–8 (2011).

[Maznev13b] Maznev, A.A. *et al.* Lifetime of sub-THz coherent acoustic phonons in a GaAs-AlAs superlattice Lifetime of sub-THz coherent acoustic phonons in a GaAs-AlAs superlattice. **041901**, (2013).

[Maznev14] Maznev, A. A. & Wright, O.B. Demystifying umklapp vs normal scattering in lattice thermal conductivity. *American Journal of Physics* **82**, 1062–1066 (2014).

[Maznev14b] Maznev A.A., Boundary scattering of phonons: specularity of a randomly rough surface in the small perturbation limit
arXiv:1411.1721

[Maznev15] Maznev, A.A., Hofmann, F., Cuffe, J., Eliason, J.K. & Nelson, K. a Lifetime of high-order thickness resonances of thin silicon membranes. *Ultrasonics* **56**, 116–21 (2015).

[Minnich11] Minnich, A. *et al.* Thermal Conductivity Spectroscopy Technique to Measure Phonon Mean Free Paths. *Physical Review Letters* **107**, 1–4 (2011).

[Murthy Peri] Murthy Peri, M.D. & Cetinkaya, C. Non-contact microsphere--surface adhesion measurement via acoustic base excitations. *Journal of colloid and interface science* **288**, 432–43 (2005).

[Nelson82] Nelson, Keith A. Casalegno, Roger, Miller, R. J. Dwayne, Fayer, M.. Laser-induced excited state and ultrasonic wave gratings: Amplitude and phase grating contributions to diffraction. *The Journal of Chemical Physics* **77**, 1144 (1982).

[Nesternerko] Nesternerko, V.F., *Dynamics of Heterogeneous Materials* (Springer-Verlag, New York, 2001)

[Nilsson] Nilsson, G. and Nelin, G. Study of the Homology between Silicon and Germanium by Thermal-Neutron Spectrometry. *Physical Review B* **6**, 3777 (1972).

[Note1] When measuring the thermal conductivity of silicon mebranes we measured the power dependence of the determined thermal conductivity. We noticed that by doubling the average power of the probe at a 5:95 (on:off) duty cycle the extracted thermal conductivity went down by roughly 5%. By increasing the duty cycle to 50:50 the measured thermal conductivity was unchanged. The conclusion is that higher peak powers lead to large heating in the sample and is not significantly impacted by the probe duration.

[Nye] F. Nye. *Physical Properties of Crystals.* (Oxford University Press, London, 1964).

[Ogilvy] Ogilvy, J.A. Wave scattering from rough surfaces. *Reports on progress in physics* **50**, (1987).

[Orthonos] Othonos, A. Probing ultrafast carrier and phonon dynamics in semiconductors. *Journal of Applied Physics* **83**, 1789 (1998).

[Pashley] Pashley, M.D. Further Consideration of the DMT Model for Elastic Contact. *Colloids and Surfaces* **12**, 69 (1984).

[Peierls] R. Peierls, "Zur kinetischen Theorie der Wärmeleitung in Kristallen," Ann. Phys. 395, 1055–1101 (1929).

[Pop] Pop, E. Energy dissipation and transport in nanoscale devices. *Nano Research* **3**, 147–169 (2010).

[Poudel] Poudel, B. *et al.* High-thermoelectric performance of nanostructured bismuth antimony telluride bulk alloys. *Science (New York, N.Y.)* **320**, 634–8 (2008).

[Regner13] Regner, K.T., Sellan, D.P., Su, Z., Amon, C.H., McGaughey, A.J.H. & Malen, J. a. Broadband phonon mean free path contributions to thermal conductivity measured using frequency domain thermoreflectance. *Nature Communications* **4**, 1640 (2013).

[Rogers94] Rogers, J., Yang, Y. & Nelson, K.A. Elastic modulus and in-plane thermal diffusivity measurements in thin polyimide films using symmetry-selective real-time impulsive stimulated thermal scattering. *Applied Physics A: Materials Science & Processing* **58**, 523–534 (1994).

[Rogers00] Rogers, J.A., Maznev, A.A., Banet, M.J. & Nelson, K.A. Optical generation and characterization of acoustic waves in thin films: Fundamentals and applications. Annual review of materials science 30, 117–157 (2000).

[Rozas] Rozas, G. *et al.* Lifetime of THz Acoustic Nanocavity Modes. *Physical Review Letters* **102**, 015502 (2009).

[Schmidt08] Schmidt, A.J., Chiesa, M., Torchinsky, D.H., Johnson, J. a., Nelson, K. a. & Chen, G. Thermal conductivity of nanoparticle suspensions in insulating media measured with a transient optical grating and a hotwire. *Journal of Applied Physics* **103**, 083529 (2008).

[Shanks] Shanks, H.R., Maycock, P.D., Sidles, P.H., Danielson, G.C. Thermal Conductivity of Silicon from 300 to 1400K. *Physical Review* **130**, 1743 (1963).
[Shchepetov] Shchepetov, A. *et al.* Ultra-thin free-standing single crystalline silicon membranes with strain control. *Applied Physics Letters* **102**, 192108 (2013).

[Shukla] Shukla, A. *et al.* Phonon Dispersion and Lifetimes in MgB2. *Physical Review Letters* **90**, 095506 (2003).

[Siemens] Siemens, M.E. *et al.* Quasi-ballistic thermal transport from nanoscale interfaces observed using ultrafast coherent soft X-ray beams. *Nature materials* **9**, 26–30 (2010).

[Slatterthwaite] Slatterwaite, C.B., Ure, R.W. Electrical and Thermal Properties of Bi2Te3. *Physical Review* **108**, 1164 (1957).

[Snyder] Snyder, G.J. & Toberer, E.S. Complex thermoelectric materials. *Nature materials* **7**, 105–14 (2008).

[Sondheimer] Sondheimer, E.H. The mean free path of electrons in metals. (1952)

[Sun] Sun, J., Tang, C., Zhan, P., Han, Z., Cao, Z.-S. & Wang, Z.-L. Fabrication of centimeter-sized single-domain two-dimensional colloidal crystals in a wedge-shaped cell under capillary forces. *Langmuir : the ACS journal of surfaces and colloids* **26**, 7859–64 (2010).

[Terazima] Terazima, M. Optical heterodyne detected transient grating for studies of photochemical reactions and solution dynamics. *Chemical Physics Letters* **304**, 343-349 (1999).

[Theocharis] G. Theocharis, N. Boechler, and C. Daraio, in *Acoustic Metamaterials and Phononic Crystals,* edited by P.A. Deymier (Springer, Berlin, 2013) Vol. 173, Chap 7.

[Theocharis09] Theocharis, G., Kavousanakis, M., Kevrekidis, P.G., Daraio, C., Porter, M. a. & Kevrekidis, I.G. Localized breathing modes in granular crystals with defects. *Physical Review E* **80**, 066601 (2009).

[Tian12] Tian, Z., Garg, J., Esfarjani, K., Shiga, T., Shiomi, J. & Chen, G. Phonon conduction in PbSe, PbTe, and PbTe_{1-x}Se_{x} from first-principles calculations. *Physical Review B* **85**, 184303 (2012).

[Tian13] Tian, Z., Lee, S. & Chen, G. Heat Transfer in Thermoelectric Materials and Devices. *Journal of Heat Transfer* **135**, 061605 (2013).

[TorchinskyPhD] D.H. Torchinsky. PhD Thesis, (Massachusetts Institute of Technology, Cambridge, MA 2008)

[Tournat] Tournat, V., Pèrez-Arjona, I., Merkel, A., Sanchez-Morcillo, V. & Gusev, V. Elastic waves in phononic monolayer granular membranes. *New Journal of Physics* **13**, 073042 (2011).

[Vermeersch] Vermeersch, B., Mohammed, A.M.S., Pernot, G., Koh, Y.R. & Shakouri, A. Thermal interfacial transport in the presence of ballistic heat modes. *Physical Review B* **90**, 014306 (2014).

[Vogel] Vogel, N., Goerres, S., Landfester, K. & Weiss, C.K. A Convenient Method to Produce Close- and Non-close-Packed Monolayers using Direct Assembly at the Air-Water Interface and Subsequent Plasma-Induced Size Reduction. *Macromolecular Chemistry and Physics* **212**, 1719-1734 (2011).

[Vittorias] Vittorias, E., Kappl, M., Butt, H.-J. & Johannsmann, D. Studying mechanical microcontacts of fine particles with the quartz crystal microbalance. *Powder Technology* **203**, 489-502 (2010).

[Wang] Wang, Y., Qiu, B., J. H. McGaughey, A., Ruan, X. & Xu, X. Mode-Wise Thermal Conductivity of Bismuth Telluride. *Journal of Heat Transfer* **135**, 091102 (2013).

[Ward] Ward, A. & Broido, D. a. Intrinsic phonon relaxation times from first-principles studies of the thermal conductivities of Si and Ge. *Physical Review B* **81**, 1-5 (2010).

[Wolfe] J.P. Wolfe, *Imaging Phonons* (Cambridge University Press, Cambridge, England, 1998)

[Yan88] Yan, Y.-X., Cheng, L.-T. & Nelson, K. a. The temperature-dependent distribution of relaxation times in glycerol: Time-domain light scattering study of acoustic and Mountain-mode behavior in the 20 MHz–3 GHz frequency range. *The Journal of Chemical Physics* **88**, 6477 (1988).

[Yang95a] Yang, Y. & Nelson, K. a. Impulsive stimulated light scattering from glass-forming liquids. I. Generalized hydrodynamics approach. *The Journal of Chemical Physics* **103**, 7722 (1995).

[Yang95b] Yang, Y. & Nelson, K. a. Impulsive stimulated light scattered from glass-forming liquids. II. Salol relaxation dynamics, nonergodicity parameter, and testing of mode coupling theory. The Journal of Chemical Physics 103, 7732 (1995).

[Yang96] Yang, Y. & Nelson, K. a. Impulsive stimulated thermal scattering study of α relaxation dynamics and the Debye–Waller factor anomaly in Ca0.4K0.6(NO3)1.4. The Journal of Chemical Physics 104, 5429 (1996).

[Ziman] J.M. Ziman, *Electrons and Phonons* (Clarendon Press, Oxford, 1960).